# Single Exciton Optical Gain from Dense Colloidal Quantum Dot Films and Their Optically Pumped Laser Applications

by

Kwangdong Roh

B.S., Seoul National University; Seoul, Republic of Korea, 2008

A dissertation submitted in partial fulfillment of the
requirements for the degree of Doctor of Philosophy
in the Department of Physics at Brown University

Providence, Rhode Island

May 2016

This dissertation by Kwangdong Roh is accepted in its present form
by the Department of Physics as satisfying the
dissertation requirement for the degree of Doctor of Philosophy.

Date_____ _____

Arto V. Nurmikko, Ph.D., Advisor

Recommended to the Graduate Council

Date_____ _____

Humphrey J. Maris, Ph.D., Reader

Date_____ _____

Rashid Zia, Ph.D., Reader

Approved by the Graduate Council

Date_____ _____

Peter M. Weber, Dean of the Graduate School

# Vita

Kwangdong Roh was born on January $16^{th}$, 1984 in Seoul, South Korea. He received his B.S. degree in Physics Education from Seoul National University in February 2009. He enrolled in the Department of Physics at Brown University in Sep, 2009. He began his graduate researches as a research assistant in June, 2010. His scientific accomplishments include;

## Publications

- S. Chen, **K. Roh**, J. Lee, W. K. Chong, E. Sari, Y. Lu, T. C. Sum, and A. V. Nurmikko, "Room-temperature ultralow threshold two dimensional photonic crystal band-edge laser from solution-based organo-lead iodide perovskite thin film," *Submitted*, 2015

- **K. Roh**, C. Dang, J. Lee, C. Breen, J. S. Steckel, S. Coe-Sullivan, and A. V. Nurmikko, "Spectroscopy of optical gain in low threshold colloidal quantum dot laser media: dominance of single exciton states," *submitted to Physical Review Letters*, 2016

- **K.Roh**, C. Dang, J. Lee, S. Chen, J. S. Steckel, S. Coe-Sullivan, and A. V. Nurmikko, "Surface-emitting red, green, and blue colloidal quantum dot distributed feedback lasers," *Optics Express*, 22(15), 18800-18806, 2014.

- C. Dang, J. Lee, **K. Roh**, H. Kim, S. Ahn, H. Jeon, C. Breen, J. S. Steckel,

S. Coe-Sullivan, and A. V. Nurmikko, "Highly efficient, spatially coherent distributed feedback lasers from dense colloidal quantum dot films," *Applied Physics Letters*, 103(17), 171104, 2013.

- M. Kim, S. Hong, **K. Roh**, K. Soh, S. Shin, J. Son, and J. Kim, "Study on elimination of twin image in a combined dual-type digital hologram microscope system," *Proceeding of SPIE*, 7329, 73290F, 2009.

**Conferences**

- S. Chen, W. K. Chong, J. Lee, **K. Roh**, E. Sari, N. Mathews, T. C. Sum, and A. V. Nurmikko, "Optically pumped distributed feedback laser from organo-lead iodide perovskite thin films," *Conference on Laser and Electro-Optics (CLEO)*, San Jose, California, 2015

- **K. Roh**, J. Lee, C. Dang, C. Breen, J. S. Steckel, S. Coe-Sullivan, and A. V. Nurmikko, "Red, green, and blue colloidal quantum dot-based optically pumped distributed feedback lasers," *IEEE International Photonics Conference*, Bellevue, Washington, 2013

- C. Dang, **K. Roh**, J. Lee, C. Breen, J. S. Steckel, S. Coe-Sullivan, and A. V. Nurmikko, "Transient gain spectroscopy in the potent single-exciton regime of dense II-VI colloidal quantum dot films," *Conference on Laser and Electro-Optics (CLEO)*, San Jose, California, 2013

- **K. Roh**, C. Dang, J. Lee, S. Ahn, H. Jeon, C. Breen, J. S. Steckel, S. Coe-Sullivan, and A. V. Nurmikko, "High performance, spatially coherent, multi-color distributed feedback lasers in optiacally pumped colloidal quantum dot," *Conference on Laser and Electro-Optics (CLEO)*, San Jose, California, 2013

- C. Dang, **K. Roh**, J. Lee, C. Breen, J. S. Steckel, S. Coe-Sullivan, and A. V. Nurmikko, "Red, green, and blue laser action in solid colloidal quantum dot films," *IEEE International Conference on Nanotechnology*, Birmingham, United Kingdom, 2012

- C. Dang, **K. Roh**, J. Lee, and A. V. Nurmikko, "Low threshold lasers from wavelength-engineered colloidal quantum dot enabled by single-exciton optical gain," *IEEE Lester Eastman Conference*, Providence, Rhode Island, 2012

- C. Dang, **K. Roh**, J. Lee, C. Breen, J. S. Steckel, S. Coe-Sullivan and A. V. Nurmikko, "Stimulated emission in red, green, and blue from colloidal quantum dot films by single exciton optical gain," *IEEE International Photonics Conference*, Burlingame, California, 2012

- **K. Roh**, M. Kim, C. Wei, J. Jung, and J. Kim, "Optical design for illumination system in a G-line stepper," *Korean Physics Society*, Kwangju, Republic of Korea, 2009

- H. Yoo, K. Kim, **K. Roh**, S. Ha, I. Han, J. Seo, and J. Kim, "Media related characteristics of the solid immersion lens system," *Optical Data Storage Topical Meeting*, Lake Buena Vista, Florida, 2009

# Acknowledgements

First I would like to thank my advisor, Professor Arto Nurmikko for his guidance, encouragement and patience during my entire graduate studies at Brown University. His continuous unwavering enthusiasm and motivation in research inspired me all the time. Without his support, I couldn't completed the Ph.D and thesis. Also, his insight and advice have enabled me to continue my academic career. I would like to express my sincerest gratitude to him. It was my great honor to be his student.

I would also like to thank my thesis committe, Professor Humphrey Maris and Professor Rashid Zia who were also on my preliminary exam committee for generously spending their precious time for reading this thesis. They have been very professional collaborators and provided valuable comments and discussion.

I wish to thank my colleagues at Brown University. I want to thank Dr. Cuong Dang for teaching and training me for the first three years of my graduate studies. I have learned a lot from his knowledge and experience in many photonics experiments. Dr. Joonhee Lee was also a great teacher and a mentor. His extensive experience and knowledge in microelectronic fabrication processes were very helpful for me to save huge amount of time. I also want to thank Songtao Chen for working together in many photonics experiments. I am sure that he will lead the photonics research in the Nurmikko's lab successfully.

I am thankful to the former and current members of Nurmikko's group; Dr. Ilker

Ozden, Dr. Ming Yin, Dr. Juan Aceros, Dr. Yoon-Kyu Song, Dr. Jing Wang, Dr. Dave Borton, Dr. Sunmee Park, Dr. Fabien Wagner, Dr. Andy Bleaser, Dr. Farah Laiwalla, Dr. Emre Sari, Dr. Jussi Rahomaki, Rizwan Huq, Travis May, Jacob Komar, Chris Heelan, Yao Lu, Ben Brush, Naubahar Agha, Zeyang Yu, Margaret Baxter, Radu Darie, Marc Powell, Nicole Dusang, Dmitrijs Celinskis, and Stefan Sigurdsson. It has been great and treasured experience to share the PN-junction space and work with them.

I would also like to acknowledge the technical helps from Mr. Michael Jibitsky and Mr. Anthony McCormick for the microelectronic facility and the electron microscopy systems. Ms. Barbara Dailey and Ms. Sandra Van Wagoner also gave me administrative support while I have been here at Brown University. I also have to remember the fruitful discussion and helps from my colleagues at Brown University; Dr. Mingming Jiang, Dr. Pei Liu, Dr. Dongfang Li, Jim Liu, Declan Oller, Dr. Jinhoo Kim, Dr. Hyokyung Sung, and Dr. Hyunmin Kim.

Finally and most importantly, I would like to thank my parents, grandparents, and sister. Without their endless love, faith, support, and encouragement from Korea, I would have never accomplished my work. I want to dedicate this dissertation to my beloved family with all my gratitude.

Abstract of " Single Exciton Optical Gain from Dense Colloidal Quantum Dot Films and Their Optically Pumped Laser Applications" by Kwangdong Roh, Ph.D., Brown University, May 2016

Colloidal quantum dots (CQDs) have emerged as an efficient fluorescent material with tunable bandgap across the visible spectrum due to quantum confinement effect. Also, studies of optical gain and stimulated emission from the CQDs have been extensively reported. However, fast-decaying non-radiative Auger recombination has been impeding further development of CQDs in the laser applications. Here, in this thesis, optical gain dynamics of our core-shell engineered type-I CQDs have been studied via transient absorption spectroscopy, and optically pumped lasers have been demonstrated as optoelectronic device applications.

The role of single exciton states as a dominant optical gain mechanism in densely packed II-VI CQD films by pump-probe laser spectroscopy has been discussed. Optimizing the Stokes shift and having narrow inhomogeneous broadening of the CQDs play the key role for empowering the single exciton states. Consequently, the single exciton gain regime is accessible without the involvement of the non-radiative Auger process.

Bragg grating structures have been incorporated with the CQD gain media to create red, green and blue surface-emitting distributed feedback lasers. A compact solid-state laser whose pulse duration exceeds the Auger decay time has been used as an excitation source. Monochromatic single mode lasing actions at low threshold levels were observed with excellent spatial coherence and conversion efficiency.

Finally, another type of CQD laser device, vertical-cavity surface-emitting laser has been fabricated using nano-porous(NP)-GaN distributed Bragg reflectors. Close-packed CQD films were sandwiched between the two NP-GaN/GaN DBRs to achieve ultra-low threshold lasing outputs under the same optical excitation condition. This enabled the realization of the pixelated laser display devices driven by a scanning mirror system.

# Contents

# List of Tables

# List of Figures

# Chapter 1

# Introduction

## 1.1 Fundamentals of Quantum Dots

Semiconductor quantum dots are nanometer-sized zero-dimensional crystalline particles. They have very different electrical and optical properties as the semiconductor dimensions get reduced. One consequence of the reduction appears in the density of states. Different density of states for different types of semiconductor structures are shown in Fig. 1.1. For quantum dots, the density of states finally shows a delta function-like shape which is similar to the density of states of atoms or molecules. Experimental results by Arakawa and Asada have shown that a restriction of lateral dimensions in semiconductors results in more confined density of states and leads to enhanced gain with less temperature sensitivity of the lasing thresholds [**?** **?** ].

In a semiconductor quantum dot, when the size is almost comparable with or even smaller than the exciton size in the bulk semiconductor, the quantum size effect begins to occur where the excitons are squeezed and electron and hole wave functions are spatially confined within the boundary of the quantum dot. In this case, continuous energy bands in bulk semiconductors become discrete levels depending on the size as seen in Fig 1.2. Thus, using this effect, the bandgap energy of a

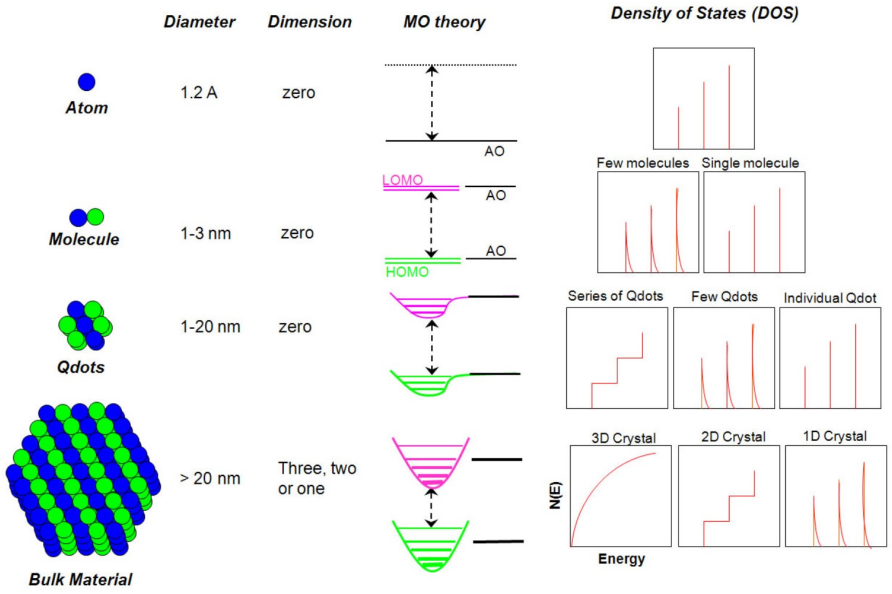


**Figure 1.1:** Schematic illustration of the changes of the density of quantum states from atom to bulk material. (MO: molecular orbital; HOMO: highest occupied MO; LUMO: lowest unoccupied MO; AO: atomic orbital) (reprinted from [**?** ])

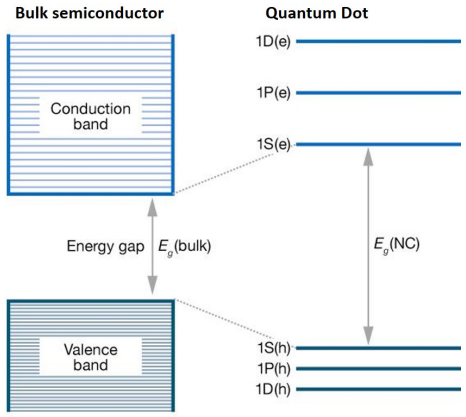


**Figure 1.2:** Comparison of energy band structures for bulk and quantum dot semiconductors. A bulk semiconductor has continuous energy bands separated by a fixed bandgap energy, $E_g$. However, quantum dots have discrete energy levels and size-dependent bandgap energy. (reprinted from [**?** ])

semiconductor quantum dot can be tunable more than 1 eV. For example, bandgap energy of CdSe-based quantum dots can span the whole visible range of spectrum.

There are several methods to produce quantum-confined semiconductor structures. Among them, colloidal quantum dots (CQDs) which are prepared by wet-chemistry based synthesis are of particular interest as their fabrication process is easier and lower cost compared to other epitaxial growth methods. This colloidal synthesis can provide better size controls with atomic precision, high monodispersity (less than 5%) and good crystallinity. It is also possible to create various types of heterostructures and shapes with great flexibility, leading to core/shell, multi-shell, nearly spherical shape, nanorod, and nanoplatelets structures [**?** **?** **?** **?** **?** ]. These advantages have resulted in CQDs being suggested as strong candidates for various application such as optically or electrically driven light-emitting diodes (LEDs) [**?** **?** **?** **?** ], photovoltaics [**?** **?** ], biosensors [**?** **?** ], and lasers [**?** **?** **?** ].

## 1.2 Thesis overview

This thesis mainly describes the research on colloidal quantum dots (CQDs) as an efficient optical gain and lasing media. **Chapter 2** serves to provide theoretical background. One of the most important properties for zero-dimensional quantum dots, the quantum confinement effect is explained with theoretical models describing the electronic structures of semiconductor quantum dots. Traditional optical gain mechanisms are introduced and our proposed model for single exciton optical gain regime for type-I CQDs is suggested. Non-radiative fast-decaying Auger processes are highlighted as they are strongly related to the light amplification process in strong confined semiconductor structures.

**Chapter 3** highlights the single exciton optical gain regime of our CQD materials via ultrafast laser pump-probe spectroscopy. First, fundamental optical and struc-

tural properties of two different CQDs are fully characterized. Then, experimental results on transient absorption and exciton dynamics are discussed, in which the optical gain emerges and is dominated by single exciton states without the inhibition of the multi-excitonic Auger process. This work will be submitted for publication soon. [**?** ]

**Chapter 4** is based on the reference [**?** ] and summarizes the work done in developing surface-emitting red, green and blue (RGB) CQD distributed feedback (DFB) lasers. Detailed microelectronic processes for fabricating nano-grating structures as a laser resonator are fully explored. High performance of the lasing actions such as spectral monochromaticity, threshold behavior, and spatial coherence is analyzed, confirming the benefit of single exciton gain regime of the CQDs used in this study.

**Chapter 5** considers another type of laser device using the same CQDs as gain media. CQD-based vertical-cavity surface-emitting lasers (VCSELs) devices using nano-porous (NP)-GaN based distributed Bragg reflectors (DBRs) are introduced, in which the lasing thresholds are extremely low due to the high quality of the DBR structures. Proof-of-concept scanning pixelated arrays of CQD-VCSEL devices are also demonstrated in this chapter.

# Bibliography

[1] Y. Arakawa and H. Sakaki. Multidimensional quantum well laser and temperature dependence of its threshold current. *Applied Physics Letters*, 40(11):939–941, 1982.

[2] M. Asada, Y. Miyamoto, and Y. Suematsu. Gain and the threshold of three-dimensional quantum-box lasers. *Quantum Electronics, IEEE Journal of*, 22(9):1915–1921, 1986.

[3] D. Bera, L. Qian, T.K. Tseng, and P.H. Holloway. Quantum dots and their multimodal applications: a review. *Materials*, 3(4):2260–2345, 2010.

[4] Victor I Klimov. Spectral and dynamical properties of multiexcitons in semiconductor nanocrystals. *Annu. Rev. Phys. Chem.*, 58:635–673, 2007.

[5] C.B. Murray, D.J. Norris, and M.G. Bawendi. Synthesis and characterization of nearly monodisperse CdE (e= sulfur, selenium, tellurium) semiconductor nanocrystallites. *Journal of the American Chemical Society*, 115(19):8706–8715, 1993.

[6] X. Peng, L. Manna, W. Yang, J. Wickham, E. Scher, A. Kadavanich, and A.P. Alivisatos. Shape control of CdSe nanocrystals. *Nature*, 404(6773):59–61, 2000.

[7] B. Guzelturk, Y. Kelestemur, M. Olutas, S. Delikanli, and H.V. Demir. Amplified spontaneous emission and lasing in colloidal nanoplatelets. *ACS Nano*, 8(7):6599–6605, 2014.

[8] Y. Chen, J. Vela, H. Htoon, J.L. Casson, D.J. Werder, D.A. Bussian, V.I. Klimov, and J.A. Hollingsworth. giant multishell CdSe nanocrystal quantum dots with suppressed blinking. *Journal of the American Chemical Society*, 130(15):5026–5027, 2008.

[9] C. Dang, J. Lee, C. Breen, J.S. Steckel, S. Coe-Sullivan, and A.V. Nurmikko. Red, green and blue lasing enabled by single-exciton gain in colloidal quantum dot films. *Nature Nanotechnology*, 7(5):335–339, 2012.

[10] K.S. Cho, E.K. Lee, W.J. Joo, E.J. Jang, T.H. Kim, S.J. Lee, S.J. Kwon, J.Y. Han, B.K. Kim, B.L. Choi, and J.M. Kim. High-performance crosslinked colloidal quantum-dot light-emitting diodes. *Nature Photonics*, 3(6):341–345, 2009.

[11] J. Kwak, W.K. Bae, D. Lee, I. Park, J. Lim, M. Park, H. Cho, H. Woo, D.Y. Yoon, and K. Char. Bright and efficient full-color colloidal quantum dot light-emitting diodes using an inverted device structure. *Nano Letters*, 12(5):2362–2366, 2012.

[12] J.M. Caruge, J.E. Halpert, V. Wood, V. Bulović, and M.G. Bawendi. Colloidal quantum-dot light-emitting diodes with metal-oxide charge transport layers. *Nature Photonics*, 2(4):247–250, 2008.

[13] C. Dang, J. Lee, Y. Zhang, J. Han, C. Breen, J.S. Steckel, S. Coe-Sullivan, and A.V. Nurmikko. A wafer-level integrated white-light-emitting diode incorporating colloidal quantum dots as a nanocomposite luminescent material. *Advanced Materials*, 24(44):5915–5918, 2012.

[14] J. Tang, K.W. Kemp, S. Hoogland, K.S. Jeong, H. Liu, L. Levina, M. Furukawa, X. Wang, R. Debnath, D. Cha, K.W. Chou, A. Fischer, A. Amassian, J.B. Asbury, and E.H. Sargent. Colloidal-quantum-dot photovoltaics using atomic-ligand passivation. *Nature Materials*, 10(10):765–771, 2011.

[15] P.V. Kamat. Quantum dot solar cells. semiconductor nanocrystals as light harvesters. *The Journal of Physical Chemistry C*, 112(48):18737–18753, 2008.

[16] I.L. Medintz, H. T. Uyeda, E.R. Goldman, and H. Mattoussi. Quantum dot bioconjugates for imaging, labelling and sensing. *Nature Materials*, 4(6):435–446, 2005.

[17] K.E. Sapsford, T. Pons, I.L. Medintz, and H. Mattoussi. Biosensing with luminescent semiconductor quantum dots. *Sensors*, 6(8):925–953, 2006.

[18] C. Dang, J. Lee, K. Roh, H. Kim, S. Ahn, H. Jeon, C. Breen, J.S. Steckel, S. Coe-Sullivan, and A.V. Nurmikko. Highly efficient, spatially coherent distributed feedback

lasers from dense colloidal quantum dot films. *Applied Physics Letters*, 103(17):171104, 2013.

[19] K. Roh, C. Dang, J. Lee, S. Chen, J.S. Steckel, S. Coe-Sullivan, and A.V. Nurmikko. Surface-emitting red, green, and blue colloidal quantum dot distributed feedback lasers. *Optics Express*, 22(15):18800–18806, 2014.

[20] K. Roh, J. Lee, C. Dang, and A.V. Nurmikko. Spectroscopy of optical gain in low threshold colloidal quantum dot laser media: Dominance of single exciton states. Manuscript submitted to Physical Review Letters for publication, 2016.

# Chapter 2

# Electronic Structure and Optical Gain Dynamics of Semiconductor Quantum Dots

## 2.1 Quantum confinement effects in semiconductor quantum dots

Chemical synthesis for fabricating semiconductor nanocrystal quantum dots makes it possible to tune the size and shape precisely and control the optical and electronic properties. For example, CQDs can now be prepared with atomic precision and high monodispersity in a variety of compositions as spherical, pyramidal, elongated, and even platelet shapes [5, 6, 9**? ?** ]. When the size of the quantum dots gets small enough, the quantum confinement effect begins to occur. Here the threshold natural length scale is given by the exciton Bohr radius, $a_x$, which is the measure of the strength of the electron-hole Coulomb interaction. In general, the Bohr radius is defined as:

$$a_x = \epsilon \frac{m}{m^*} a_0 \quad , \tag{2.1}$$

where $\epsilon$ is the dielectric constant of the material, $m^*$ is the mass of the particle, $m$ is the rest mass of the electron, and $a_0$ is the Bohr radius of the hydrogen atom. If the size of the nanocrystal quantum dots is smaller than its exciton Bohr radius, then the motion of the electrons and holes are spatially confined within the boundary of the quantum dots. This is referred as the strong confinement regime.

One of the consequences of the strong confinement regime is the enhancement of Coulomb interaction since it scales approximately with $r^{-1}$ ($r$ is the radius of the quantum dots). Therefore, the Coulomb interaction becomes size dependent, leading to an increase of the interaction energies as the size of the quantum dots decreases. The Coulomb interaction is related to the exciton and biexciton binding energies in quantum dots. The former is a measure of the electron-hole interaction strength, and the latter is a measure of the strength of the exciton-exciton interaction. For a bulk CdSe semiconductor, the exciton and biexciton binding energies are 16 and 4.5 meV, respectively [**?** **?** ]. However, for CdSe quantum dots, the exciton binding energy can be more than 100 meV [**?** ]and the biexciton binding energy can be tens of meV [**?** **?** **?** ].

In order to quantify the size dependent electronic properties, several theoretical approaches have been investigated. One of the simplest model is the "particle-in-a-sphere" model. In this model, a nanocrystal quantum dot with radius $a$ is in a spherical potential well:

$$V(r) = \begin{cases} 0, & \text{if } r \leq a \\ \infty, & \text{if } r > a \quad . \end{cases} \tag{2.2}$$

In spherical coordinates, the solutions of the Schrödinger equation can be separable

into products:

$$\Psi_{n,l,m}(r,\theta,\phi) = R_{nl}(r)Y_{lm}(\theta,\phi) \quad , \tag{2.3}$$

where $R_{nl}(r)$ are solutions of radial equation and $Y_{lm}(\theta,\phi)$ are spherical harmonics that satisfy the following angular equation:

$$-\hbar^2\left[\frac{1}{\sin\theta}\left\{\frac{\partial}{\partial\theta}\left(\sin\theta\frac{\partial}{\partial\theta}\right)+\frac{1}{\sin^2\theta}\frac{\partial^2}{\partial\phi^2}\right\}\right]Y_{lm}(\theta,\phi) = l(l+1)\hbar^2 Y_{lm}(\theta,\phi) \quad . \tag{2.4}$$

Inside the well, the radial equation becomes

$$\frac{d^2u}{dr^2} = \left[\frac{l(l+1)}{r^2} - k^2\right]u \quad , \tag{2.5}$$

where $u = rR_{nl}(r)$ and $k$ is $\sqrt{2mE}/\hbar$. The general solution to Eq. 2.5 is found as

$$u(r) = Arj_l(kr) + Brn_l(kr) \quad , \tag{2.6}$$

where $j_l$ is the spherical Bessel function of order $l$, and $n_l$ is the spherical Neumann function of order $l$, which are defined as follows:

$$j_l(x) \equiv (-x)^l\left(\frac{1}{x}\frac{d}{dx}\right)^l\frac{\sin x}{x}; \quad n_l(x) \equiv -(-x)^l\left(\frac{1}{x}\frac{d}{dx}\right)^l\frac{\cos x}{x} \quad . \tag{2.7}$$

Note that Neumann functions blow up at the origin. So the coefficient $B$ in Eq. 2.6 must be zero, and hence

$$R(r) = Aj_l(kr). \tag{2.8}$$

The boundary condition, $R(a) = 0$ requires that

$$k = \frac{1}{a}\beta_{nl} \quad , \tag{2.9}$$

where $\beta_{nl}$ is the $n$th zero of the $l$th spherical Bessel function. Finally, the wave functions are

$$\Psi_{n,l,m}(r,\theta,\phi) = A j_l(\beta_{nl} r/a) Y_{lm}(\theta,\phi) \ , \tag{2.10}$$

with constant $A$ to be determined by normalization. The allowed energies are given by

$$E_{nl} = \frac{\hbar^2}{2ma^2}\beta_{nl}^2 \ . \tag{2.11}$$

The eigenfunctions (Eq. 2.10) are atomic-like orbitals with quantum numbers, $n$, $l$, and $m$. The energies (Eq. 2.11) are proportional to $1/a^2$ and dependent on the size of the quantum dot. Therefore, the bandgap energy of a quantum dot can be tuned simply by changing the size of the quantum dots. For CdSe-based quantum dots, the bandgap energy can be tuned by more than 1 eV and cover the whole visible spectrum.

To consider more realistic band structures, the above model can be improved by the effective mass approximation which was proposed by Efros and Efros [**?** ], and Brus [**?** ]. In this approximation, the electronic wave functions in a bulk semiconductors can be expressed as

$$\Psi_{nk}(\vec{r}) = u_{nk}(\vec{r}) \ e^{i\vec{k}\cdot\vec{r}} \ , \tag{2.12}$$

where $u_{nk}$ is a function with the periodicity of the crystal lattice and the wave functions are labeled by the band index $n$ and wave vector $k$. Then, the band diagram in the effective mass approximation, is assumed to be a simple parabolic feature near the band-edge. So far, the Coulomb interaction between the electron and the hole has been ignored. However, the Coulomb interaction still exists in the quantum dots. In the strong confinement regime, according to Eq.2.11, the confinement

energy of each carrier scales as $1/a^2$, whereas the Coulomb interaction scales as $1/a$. In sufficiently small quantum dots, the quadratic confinement term dominates and the Coulomb interaction can be considered as perturbation. Thus, the electron and hole can be treated independently and each is described as a "particle-in-a-sphere". Using Eq. 2.10, the electron-hole pair (ehp) states in quantum dots are written as:

$$\Psi_{ehp}(\vec{r_e},\vec{r_h}) = \Psi_e(\vec{r_e})\Psi_h(\vec{r_h}) = A\Big[j_{l_e}(\beta_{n_e l_e} r_e/a)Y_{l_e m_e}\Big]\Big[j_{l_h}(\beta_{n_h l_h} r_h/a)Y_{l_h m_h}\Big] \ . \quad (2.13)$$

The Coulomb interaction can be expressed as:

$$\frac{1}{\mid \vec{r_e} - \vec{r_h} \mid} = \sum_{l=0}^{\infty}\Big(\frac{4\pi}{2l+1}\Big)\frac{r_<^l}{r_>^{l+1}}\sum_{m=-l}^{l} Y_{l_e m_e} Y_{l_h m_h} \ , \quad (2.14)$$

and calculated numerically to be - $1.78e^2/(\epsilon a)$ [**?** ]. Finally, the shift of the bandgap energy of the quantum dots in strong confinement regime can be given as:

$$\Delta E_g = \frac{\hbar^2\pi^2}{2a^2}\left(\frac{1}{m_e}+\frac{1}{m_h}\right) - 1.78\frac{e^2}{\epsilon a} - 0.248E_{Ry} \ . \quad (2.15)$$

The first term comes from the confinement energy due to the "particle-in-a-sphere" assumption. The second term represents the Coulomb interaction energy. The last term is the size independent exciton Rydberg energy which is usually negligible except for semiconductors with small dielectric constant [**?** ]. Therefore, comparing with this exciton Rydberg energy, $E_{Ry} = e^2/(2\epsilon a_x)$, the Coulomb interaction of quantum dots in the strong confinement regime ($a \ll a_x$), is significantly larger than that of a bulk material. The effect of exciton binding energy due to the Coulomb interaction in quantum dots can be seen in the size-dependent absorption spectrum in CdSe quantum dots (Fig. 2.1).

The real band structure of semiconductors, especially CdSe, is much more complicated. Although the conduction band fits well with the effective mass approximation, the valence band does not because of the six fold degeneracy at $k = 0$ which stems

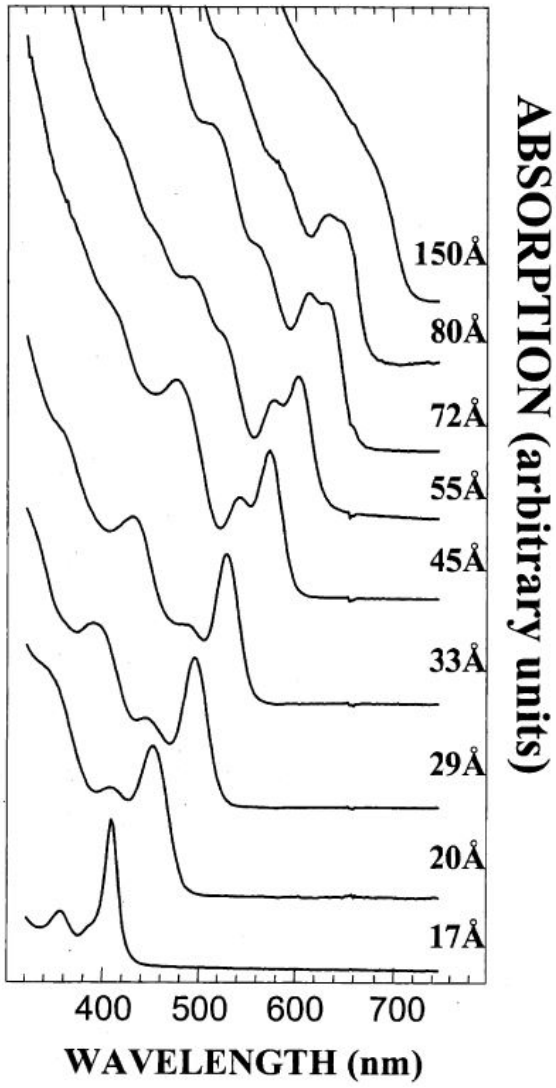


**Figure 2.1:** Size-dependent absorption spectrum from CdSe quantum dots. As the size of CdSe quantum dots decreases, the exciton peaks in the absorption spectrum get enhanced. (reprinted from [**?** ])

from Se $4p$ orbitals [**?** ]. Together with the spin-orbit coupling ($\Delta_{SO} = 42$ meV for CdSe [**?** ]), the valence band is split into $J = 3/2$ and $J = 1/2$ subbands at $k = 0$, where $J$ is the total angular momentum. In addition, the $J = 3/2$ subband is further split into heavy-hole and light-hole subbands away from $k = 0$. In wurtzite crystal structures, the hexagonal lattice induces a crystal field that breaks the degeneracy of the heavy-hole and light-hole subbands at $k = 0$. There also exist various complicated models with better realistic band structures such as "$k \cdot p$ method" [**?** ], "Luttinger Hamiltonian" [**?** ], "Kane model" [**?** ], and "linear combination of atomic orbital theory" (LCAO) [**?** ]. However, the detail explanations will not be discussed in this thesis.

In addition to the exciton transition due to the quantum confinement effect, the carrier-carrier interactions can affect strongly the dynamics of certain energy relaxation and recombination channels and make them more efficient [**?** ]. These effects are heavily related with the development of optical amplification mechanisms in semiconductor quantum dots. The detailed discussion on this topic will be followed in the next section.

## 2.2 Multiexciton Auger recombination process in semiconductor quantum dots

For zero dimensional semiconductor quantum dots, the intrinsic decay channel for a single exciton is the radiative recombination process which occurs within a time on the order of tens of nanoseconds. However, multi-exciton states are dominated by the fast Auger recombination process which is non-radiative [**?** **?** **?** ]. It is significantly enhanced for quantum dots in the strong confinement regime because the strong spatial confinement of electron and hole wave functions leads to the enhancement of the Coulomb interaction. Note that the Auger recombination which is a three-body

interaction is mediated by the Coulomb interaction. As a result of the Auger process, the recombination energy is not emitted as a photon, but instead is transferred to an electron or a hole which is further re-excited to a higher energy state [**?** **?** ]. Sometimes the absorption of the recombination energy by the third particle ionizes the quantum dots; this is known as Auger ionization and observed in CdSe quantum dots [**?** **?** ].

The Auger process however is not very efficient in bulk semiconductors since the momentum and energy of the charge carriers should be conserved, which results in a significant amount of thermal energy being needed to activate the process [**?** **?** ]. However, the Auger process gets greatly enhanced in quantum-confined systems, where the relaxation in momentum conservation removes the activation barrier [**?** **?** **?** ]. Also, unlike in bulk semiconductors, the Auger lifetime in quantum dots is quantized due to the quantization of the carrier populations. So, Auger recombination process occurs in a sequence of steps from $N$ to $N$-1, $N$-2, $\cdots$, 2, and 1 electron-hole pair state with each step characterized by a discrete exponential decay time constant, $\tau_N$ [4]. Also, the Auger lifetime in quantum dots shows a linear size dependence. This linear size dependence has been experimentally reported in quantum rods structures as well as zero-dimensional quantum dot systems [**?** **?** **?** ].

Although the time constants of the Auger decay process in quantum-confined systems depend on the exciton multiplicity and the size and shape of quantum dots, they are still shorter than radiative lifetimes, which means that Auger recombination is the dominant decay channel for multiexcitons. This is why many researchers try to suppress the Auger process by modifying the shape and chemical composition of the quantum dots, or obtain optical gain from single exciton states. Reduced overlap between the electron and hole wave functions is a well-known way to suppress the Auger decay process in CdSe/CdS core/shell quantum dots [**?** **?** **?** ]. This can also be applied to giant-quantum dots to suppress Auger rates. Suppression occurs

if electronic states extend over the entire structure while holes are tightly confined within the small core [8**?** **?** ]. Theoretical studies by Cragg and Efros [**?** ] and Climente *et al.* [**?** ] have predicted that the shape of the confinement potential can significantly affect the Auger decay rate. Especially, by smoothing the confinement potential, for example, from a sharp step-like potential to smooth parabolic profile, the Auger decay rate can be made less effective due to the reduced overlap between the initial and final states of the carrier excited during the Auger recombination [**?** ].

As was pointed out, the suppression of the Auger recombination process is very important for practical applications of the quantum dots. Specifically, the recombination of multi-excitons for lasers and charging effects for light-emitting-diodes, photovoltaic cells, and single-photon emitters are the consequences of the Auger process. However, the Auger process can be completely circumvented for single excitons as the nature of the multi-particle interaction. So, we will focus on how to avoid the Auger process with single exciton states as dominant source of optical gain from engineered core/shell structured CQDs in chapter three.

## 2.3 Optical gain mechanisms in colloidal quantum dots

### 2.3.1 Biexciton gain from two-level system

This section discusses the optical gain mechanism for a simplified quantum dot model. First, the lowest energy emitting transition in semiconductor quantum dots can be simplified into a two-level system [**?** ] which is illustrated in Fig. 2.2. The maximum occupancy for electrons is two because of the spin degeneracy. Therefore, an unexcited quantum dot has two electrons in the ground state (Fig. 2.2(a)). From

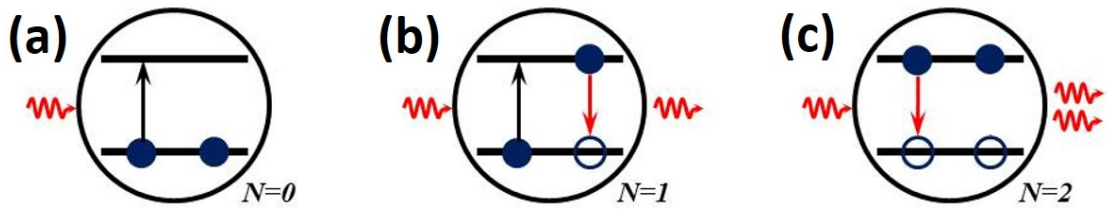


**Figure 2.2:** Two-level system representing a simplified view for semiconductor quantum dots. A quantum dot in the (a) ground state, (b) single exciton state, and (c) biexciton state.

the unexcited state, incoming photons with energy equal to the transition energy gap of the two-level system are absorbed, pushing the system into the excited state and leaving behind a hole in the ground state. Thus, there is no amplification of photons.

When a photon enters the system in the single-exciton state (Fig. 2.2 (b)), it is either absorbed by the electron in the ground state to create a biexciton state, or it stimulates the emission of an additional photon to bring the system back to the ground state. The probabilities of the two processes, absorption and stimulated emission are equal. Consequently, the net photon amplification is zero, satisfying the so-called transparency condition.

In order to achieve population inversion for optical gain, there should be at least two electrons in the excited state (Fig. 2.2 (c)), where the number of electron and hole pairs, $N$, is 2. In this case, stimulated emission is the only possible channel for a resonant incoming photon. This implies that the population inversion can happen when the average electron-hole pairs per quantum dots, $<N>$, is more than 1. Also, the lasing transition in semiconductor quantum dots is governed by biexciton-exciton transition. However, this evidently involves the non-radiative recombination channel, which is known as Auger process. The consequences of the Auger recombination process will be discussed in the following section.

### 2.3.2 Single exciton gain from type-II colloidal quantum dots

The biggest drawback of the biexciton gain mechanism in quantum dots is the dominant decaying channel of Auger process which is two orders of magnitude faster than the spontaneous emission lifetime (typically on the order of $\sim$ 10 ns for CdSe-based CQDs). This hinders the development of amplified spontaneous emission (ASE) and stimulated emission because it requires fast optical excitation sources (preferably in sub pico second time scale) and a large volume fraction of semiconductor quan-

tum dots [**?** ]. To circumvent the fast multi-excitonic Auger recombination process, Klimov and Bawendi proposed a model to achieve optical gain from the single exciton state in type-II colloidal quantum dots [**?** ], where charge carriers (electrons and holes) are confined in the core and shell separately unlike the type-I quantum dots. When the electrons and holes are segregated in the core and shell areas, there is an induced local electric field which is called the carrier-induced Stark effect [**?** **?** ]. The existence of the local electric field may modify the absorption energy of the electron in the ground state as seen in Fig. 2.3 (b), leading to the change of the condition for the optical gain.

In the presence of Coulomb exciton-exciton interactions which are significantly enhanced in the strong confinement regime, the absorption cross section, $\sigma^A$, of a quantum dot can be expressed as follows [**?** ]:

$$\sigma^A(\omega) = \frac{4\pi\omega}{n_r c} \sum_{i,j} \frac{|d_{ij}|^2 \Gamma_{ij}}{(\hbar\omega - \hbar\omega_{ij})^2 + \Gamma_{ij}^2} \ , \tag{2.16}$$

where $\omega_{ij}$ is the frequency of the interband transition, which couples the $i$-valence-band to the $j$-conduction-band quantized states, $\Gamma_{ij}$ and $d_{ij}$ are the linewidth and the dipole matrix element of this transition, $n_r$ is the refractive index, $\hbar$ is the reduced Planck's constant, and $c$ is the speed of light. However, the absorption cross section is a sum of individual partial absorption cross sections, $\sigma_{ij}^A(\omega)$, where

$$\sigma_{ij}^A(\omega) = \frac{4\pi\omega}{n_r c} \frac{|d_{ij}|^2 \Gamma_{ij}}{(\hbar\omega - \hbar\omega_{ij})^2 + \Gamma_{ij}^2} \ . \tag{2.17}$$

The stimulated emission cross section is the inverted $i$-$j$ transition, which can be expressed as follows:

$$\sigma_{ji}^{SE}(\omega) = -\sigma_{ij}^A(\omega) \ . \tag{2.18}$$

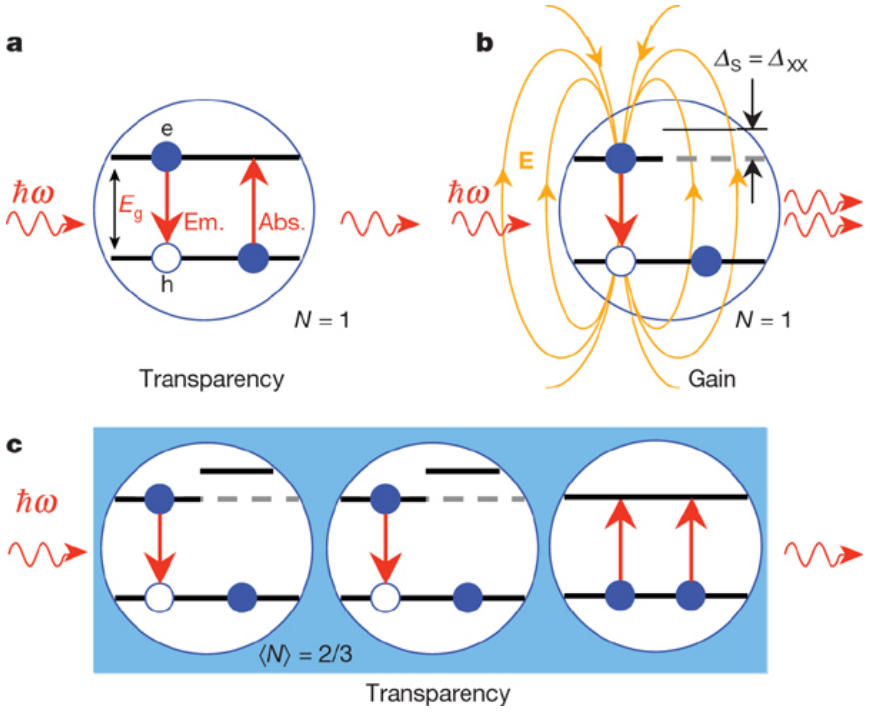


**Figure 2.3:** The concept of (a) biexciton gain in type-I CQDs and (b) single exciton gain in type-II CQDs. The optical transparency condition can be achieved when the average electron-hole pair concentration is more than 2/3. (reprinted from [**?** ])

If we assume a low excitation regime, so that the ensemble includes either quantum dots excited with a single exciton (fraction $n_x$) or unexcited quantum dots (fraction $n_o$ = 1 - $n_x$), then, the average exciton occupancy (concentration) per quantum dot, $<N> = n_x$. In a simplified two-level system for the type-II quantum dots, the absorption cross section for the quantum dots in the ground state where incoming photons can only be absorbed can be written as follows:

$$\sigma_{11}^{A0}(\omega) = \frac{4\pi\omega}{n_r c} \frac{|d_{11}|^2 \Gamma_{11}}{(\hbar\omega - \hbar\omega_{11})^2 + \Gamma_{11}^2} \ . \tag{2.19}$$

However, excited quantum dots can produce both absorption and stimulated emission. Under the presence of the Coulomb exciton-exciton (X-X) interaction (Fig. 2.3 (b)), the absorption maximum is blue-shifted with respect to the stimulated emission by the X-X interaction energy, $\Delta_{XX}$, since any subsequent absorption of a photon can only occur at higher energy. As a result, the absorption and stimulated emission cross sections for the excited quantum dots can be expressed as follows:

$$\sigma_{11}^{Ax}(\omega) = \frac{4\pi\omega}{2n_r c} \frac{|d_{11}|^2 \Gamma_{11}}{(\hbar\omega - \hbar\omega_{11} - \Delta_{XX})^2 + \Gamma_{11}^2} \ , \tag{2.20}$$

and

$$\sigma_{11}^{SEx}(\omega) = -\frac{4\pi\omega}{2n_r c} \frac{|d_{11}|^2 \Gamma_{11}}{(\hbar\omega - \hbar\omega_{11} - \Delta_{XX})^2 + \Gamma_{11}^2} \ . \tag{2.21}$$

The absorption coefficient of the ensemble of the excited quantum dots with concentration $n_{QD}$, considering the distribution of transition energies arising from different quantum dot sizes, is then

$$\alpha_{11}(\omega) = n_{QD} \int_0^\infty \Big[(1 - n_x)\sigma_{11}^{A0} + n_x(\sigma_{11}^{Ax} + \sigma_{11}^{SEx})\Big] g(\hbar\omega_{11}) d(\hbar\omega_{11}) \ . \tag{2.22}$$

The distribution function $g(\hbar\omega_{11})$ can be approximated by a Gaussian function

$$g(\hbar\omega_{11}) = \frac{1}{\sqrt{\pi}\Gamma} e^{\frac{-(\hbar\omega_{11}-\hbar\omega_0)^2}{\Gamma^2}} \ , \tag{2.23}$$

, where $\omega_0$ is the central frequency of the lowest-energy transition in the ensemble of quantum dots and $\Gamma$ is its inhomogeneous broadening. Finally, considering that the transition linewidths are dominated by inhomogeneous broadening, the absorption coefficient is expressed as follows

$$\alpha_{11}(\hbar\omega) = \frac{4\pi\omega}{2n_r c} \frac{\sqrt{\pi}|d_{11}|^2\Gamma_{11}}{2\Gamma} e^{\frac{-(\hbar\omega-\hbar\omega_0)^2}{\Gamma^2}} \left\{ 2 - 3n_x + n_x e^{-\frac{\Delta_{XX}^2}{\Gamma^2}} e^{\frac{2(\hbar\omega-\hbar\omega_0)\Delta_{XX}}{\Gamma^2}} \right\} . \tag{2.24}$$

A negative value of absorption coefficient means the optical gain. So, the gain threshold at $\omega = \omega_0$ can be calculated as

$$< N_{th} >= \frac{2}{3 - e^{-\frac{\Delta_{XX}^2}{\Gamma^2}}} \ . \tag{2.25}$$

If the coulomb X-X interaction energy is significantly greater than the transition linewidth, Eq. 2.25 reduces to $<N_{th}> = 2/3$, which is the transparency condition and less than 1 (Fig. 2.3) (c). This means that the optical gain can develop without the inhibition of the multi-excitonic Auger decay process only by single exciton states.

To summarize, the introduction of the local electric field which induces a giant transient Stark shift ($\sim$ 100 meV) in the absorption energy of the electron, makes it possible to break the balance between the absorption and stimulated emission. This reduces the required excitation for reaching population inversion even when $<N>$ = 2/3, which brings the quantum dots in the single exciton optical gain regime. Although the optical gain in the actual quantum dots is mediated by the multi-exciton states as well, the optical gain will be dominated by the single exciton state under the presence of the induced Stark effect and Coulomb exciton-exciton interaction. This

finally reduces the involvement of fast decaying non-radiative Auger recombination process which impedes the amplification of photons.

### 2.3.3 Single exciton gain from type-I colloidal quantum dots

Although it is possible to obtain optical gain condition from single exciton state in type-II quantum dots, the reduced overlap between the electron and hole wave functions due to the spatial separation further decreases the gain coefficient as well as the photoluminescence quantum yield. If we can reach the single exciton optical gain regime from type-I quantum dots, it would be possible to maximize the gain coefficient by the increased overlap between the electron and hole wave functions. Here, we propose another single exciton optical gain mechanism by introducing Stokes shift, which is the energy difference between the absorption and emission transitions, to effectively bypass the Auger process from type-II quantum dots.

If the magnitude of the Stokes shift is much bigger than the transition linewidth, then there would be an imbalance between the absorption and emission (Fig. 2.4). As a result, even for a quantum dot in the ground state, an incoming photon cannot be absorbed by electrons in the ground state. The transparency condition can be met only at $<N> = 0$. Having a single exciton in a quantum dot can stimulate emission of an incoming photon to amplify the light. Thus the optical gain threshold can be achieved at $<N> > 0$.

We have carried out ultrafast laser pump-probe experiments to dissect the optical gain properties on the core/shell engineered CQDs with optimized Stokes shift. The spectroscopic results proved that the CQD materials used in the study exhibited the presence of optical gain under low enough excitation regime where the average exciton occupation per CQD is less than 1 ($<N> \sim 0.5$). Also, we have observed that the optical gain lasted for 1 ns which is one order of magnitude longer than the typical Auger recombination lifetime. Therefore, while maintaining high photoluminescence

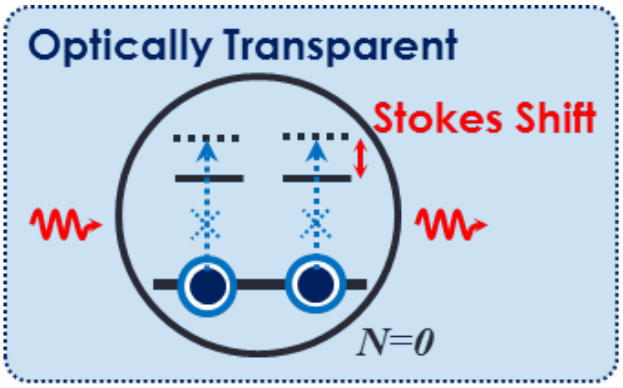


**Figure 2.4:** Single exciton optical gain mechanism in type-I quantum dots based on large magnitude of Stokes shift. The optical gain threshold can be reached at the average exciton population $<N> > 0$.

quantum yield of the close-packed CQD films at room temperature, the single exciton states were able to dominate the development of the optical gain from type-I CQDs. The details about the experimental setup and results will be followed in chapter three.

## 2.4 Rate equation and exciton dynamics for lasing in type-I CdSe/ZnCdS colloidal quantum dots

We proposed a new optical gain model relying on the single exciton state in type-I CQDs by introducing a large magnitude of Stokes shift. To verify the optical gain mechanism, pump-probe spectroscopic experiments were done on the closely packed CQD films at room temperature. In addition, amplified spontaneous emission was observed under various pump pulsed durations (from 100 fs to 10 ns) in the low excitation regime which corresponds to $<N> \sim 0.8$. Given the experimental results discusses in Chapter 3, exciton dynamics during the optical pumping process were analyzed and discussed by solving a series of rate equation under various optical pumping conditions.

The fraction of quantum dots that have $N$ excitons can be expressed as $n_N$(t). The excitation and decay processes for the multi- and single excitons occur via a sequence of quantized steps in quantum dots [**?** ]. Then, the rate equations for the $n$-exciton states can be built as follows:

$$\frac{dn_N(t)}{dt} = -n_N(t)\Big[R_N^{decay}(t)+R^{pump}(t)\Big]+n_{N+1}(t)R_{N+1}^{decay}(t)+n_{N-1}(t)R^{pump}(t) \quad (2.26)$$

,

$$\frac{dn_0(t)}{dt} = n_1(t)R_1^{decay}(t) - n_0(t)R^{pump}(t) \ . \quad (2.27)$$

where $R_N^{decay}(t)$ is the decay rate of $N$-exciton state, $R^{pump}(t)$ is the optical pumping(excitation) rate, $n_0(t)$ is the concentration of unexcited quantum dots, and $n_1(t)$ is the fraction of single exciton states in the quantum dots. Assuming the quantum dots are in the ground state before the pumping process, then the initial conditions are as follows:

$$n_{N+1}(0) = n_N(0) = 0 \text{ , and } n_0(0) = 1 \text{ .} \tag{2.28}$$

Here the decay rate is governed by the combination of the Auger recombination and spontaneous emission processes with time constants of $\tau_{Auger}$, and $\tau_{SP}$ respectively for $N$ is more than 2. For single exciton states, the decay rate is however only governed by the spontaneous emission process. Therefore these can be described as follows:

$$R_N^{decay} = \frac{1}{\tau_{Auger}} + \frac{1}{\tau_{SP}} \text{ for } N \geq 2, \text{ and } R_1^{decay} = \frac{1}{\tau_{SP}} \text{ .} \tag{2.29}$$

We used 120 ps and 15 ns for the Auger and spontaneous emission time constants, respectively which were acquired by our previous experiments. The pump rate, $R^{pump}(t)$, is the multiplication of the absorption and laser pulse as a function of time which is typically Gaussian. Then, the average number of excitons per quantum dots can be expressed as

$$< N(t) >= \sum_{i=0}^{N} i \cdot n_i(t) \text{ .} \tag{2.30}$$

With these rate equations and initial conditions, we have calculated the pulse energy density to bring the average exciton concentration per quantum dots to the

level of 0.8 which is the amplified spontaneous emission threshold level. Figure 2.5 represents the decay dynamics of the average exciton concentrations as a function of time. In order to reach $<N> = 0.8$, the pumping energy densities needed to be about 535 and 1910 $\mu$J/cm$^2$ for 100 ps and 10 ns pulsed excitation conditions, respectively. This implies that the longer pulsed excitation requires higher pumping energy as we expect. Even if the maximum value of the average exciton concentration is still below 1, there exist finite amounts of multi-excitons in quantum dots. Therefore, when the excitation source has longer pulse duration, it competes with the non-radiative Auger decay process which increases the required pumping energy density. In Fig. 2.5 (c), the fast decaying excitons can be observed at an early stage of decay process.

According to our previous ASE experiments [**?** ], the threshold pumping energy densities were 90, 720, and 1800 $\mu$J/cm$^2$ for 100 fs, 270 ps, and 10 ns pulsed excitation conditions, respectively. Based on our rate equations, the calculated pumping energy densities were 90, 650, and 1950 $\mu$J/cm$^2$, respectively which are very close to the experimental results. The slight difference between the calculated and experimental values may come from the fact that we have used different stripe geometry of the pumping laser beam by using different cylindrical lens, leading to different stripe widths in thickness. Also, in the rate equation, we have assumed that the multi-excitons decay with the same lifetime. However, the Auger rates are quantized in the strongly confined regime of quantum dots, so that the relaxation constants of the four-, three-, and two-exciton states are 33, 60, and 147 ps, respectively, in the case of CdSe quantum dots for example [4**?** ].

The dependence of the pumping pulse duration was investigated by the above rate equations. Figure 2.6 shows the required pumping energy density to reach $<N> = 0.8$ at various pumping pulse durations. When the pulse duration is shorter than 100 ps which is comparable to the Auger decay time constant (120 ps in our model),

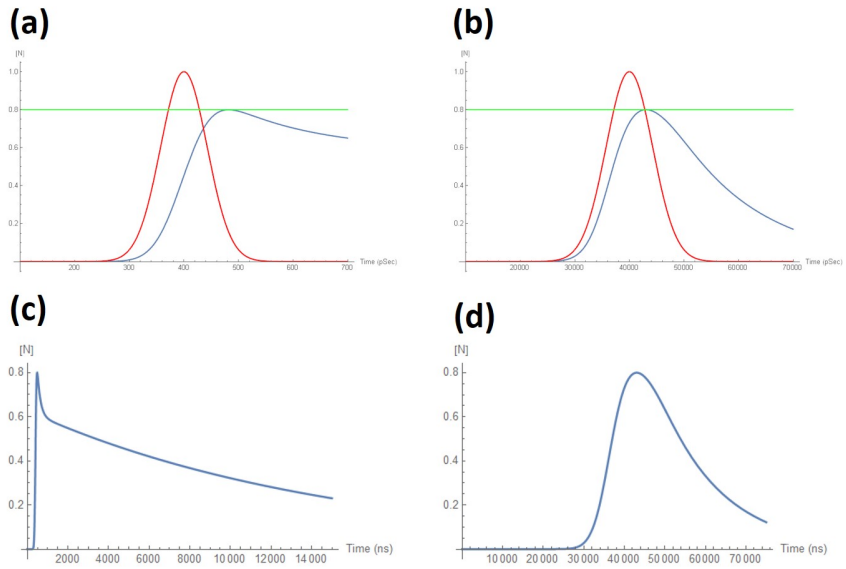


**Figure 2.5:** Decay dynamics of the average exciton occupation number per quantum dots as a function of time under (a) 100 ps and (b) 10 ns pulsed optical excitation conditions. The required pumping energy densities were 535 and 1910 $\mu$J/cm$^2$, respectively. (c) and (d) are plotted in the longer time scale for 100 ps and 10 ns pulsed excitation conditions, respectively.

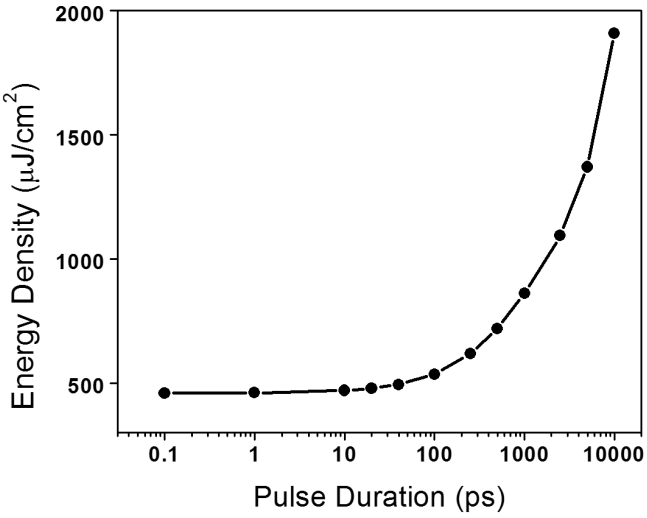


**Figure 2.6:** The pumping energy density required to reach the average exciton concentration of $<N> = 0.8$ has been plotted as a function of the pumping pulse duration.

the pumping energy densities were almost the same. This is because the decay term in the rate equation is dominated by the Auger decay term. Conversely, when the pulse duration becomes longer than the Auger time constant, the decay term in the rate equation is no longer dominated by the Auger term any more. Instead, both the Auger and pump terms contribute to the decay dynamics of the exciton states. Consequently, as the pulse duration gets longer, the energy density needs to be higher to compete with the Auger process.

Chapter three discusses the experimental results on spectroscopy of the optical gain dynamics for the closed-packed CQD films at room temperature via ultrafast laser pump-probe experiments. Our proposed optical gain model for type-I CQDs will be evaluated experimentally.

# Bibliography

[1] C.B. Murray, D.J. Norris, and M.G. Bawendi. Synthesis and characterization of nearly monodisperse CdE (e= sulfur, selenium, tellurium) semiconductor nanocrystallites. *Journal of the American Chemical Society*, 115(19):8706–8715, 1993.

[2] L. Qu and X. Peng. Control of photoluminescence properties of CdSe nanocrystals in growth. *Journal of the American Chemical Society*, 124(9):2049–2055, 2002.

[3] X. Peng, L. Manna, W. Yang, J. Wickham, E. Scher, A. Kadavanich, and A. P. Alivisatos. Shape control of CdSe nanocrystals. *Nature*, 404(6773):59–61, 2000.

[4] C. Dang, J. Lee, C. Breen, J.S. Steckel, S. Coe-Sullivan, and A.V. Nurmikko. Red, green and blue lasing enabled by single-exciton gain in colloidal quantum dot films. *Nature Nanotechnology*, 7(5):335–339, 2012.

[5] S. Ithurria, M.D. Tessier, B. Mahler, R.P.S.M. Lobo, B. Dubertret, and Al. L. Efros. Colloidal nanoplatelets with two-dimensional electronic structure. *Nature Materials*, 10(12):936–941, 2011.

[6] G. Beni and T_.M. Rice. Theory of electron-hole liquid in semiconductors. *Physical Review B*, 18(2):768, 1978.

[7] S. Shionoya, H. Saito, E. Hanamura, and O. Akimoto. Anisotropic excitonic molecules in CdS and CdSe. *Solid State Communications*, 12(3):223–226, 1973.

[8] L.E. Brus. Electron–electron and electron-hole interactions in small semiconductor crystallites: The size dependence of the lowest excited electronic state. *The Journal of chemical physics*, 80(9):4403–4409, 1984.

[9] K.I. Kang, A.D. Kepner, S.V. Gaponenko, S.W. Koch, Y.Z. Hu, and N. Peyghambarian. Confinement-enhanced biexciton binding energy in semiconductor quantum dots. *Physical Review B*, 48(20):15449, 1993.

[10] V.I. Klimov, S. Hunsche, and H. Kurz. Biexciton effects in femtosecond nonlinear transmission of semiconductor quantum dots. *Physical Review B*, 50(11):8110, 1994.

[11] M. Achermann, J.A. Hollingsworth, and V.I. Klimov. Multiexcitons confined within a subexcitonic volume: Spectroscopic and dynamical signatures of neutral and charged biexcitons in ultrasmall semiconductor nanocrystals. *Physical Review B*, 68(24):245302, 2003.

[12] Al. L. Efros and Al. L. Efros. Interband absorption of light in a semiconductor sphere. *Soviet Physics Semiconductors-Ussr*, 16(7):772–775, 1982.

[13] L.E. Brus. A simple model for the ionization potential, electron affinity, and aqueous redox potentials of small semiconductor crystallites. *The Journal of chemical physics*, 79(11):5566–5571, 1983.

[14] Y. Wang and N__. Herron. Nanometer-sized semiconductor clusters: materials synthesis, quantum size effects, and photophysical properties. *The Journal of Physical Chemistry*, 95(2):525–532, 1991.

[15] C.B. Murray, C.R. Kagan, and M.G. Bawendi. Synthesis and characterization of monodisperse nanocrystals and close-packed nanocrystal assemblies. *Annual Review of Materials Science*, 30(1):545–610, 2000.

[16] J.B. Xia. Electronic structures of zero-dimensional quantum wells. *Physical Review B*, 40(12):8500, 1989.

[17] K.H. Hellwege, A.M. Hellwege, H. Landolt, R. Börnstein, O. Madelung, and J.H. Callomon. *Landolt-Bornstein: Numerical Data and Functional Relationships in Science and Technology*, volume 15. Springer, 1987.

[18] C. Kittel. Quantum theory of solids, 1987.

[19] J.M. Luttinger. Quantum theory of cyclotron resonance in semiconductors: General theory. *Physical Review*, 102(4):1030, 1956.

[20] Evan O Kane. Band structure of indium antimonide. *Journal of Physics and Chemistry of Solids*, 1(4):249–261, 1957.

[21] E. Kucur, J. Riegler, G.A. Urban, and T. Nann. Determination of quantum confinement in CdSe nanocrystals by cyclic voltammetry. *Journal of Chemical Physics*, 119(4):2333–2337, 2003.

[22] V.I. Klimov. Mechanisms for photogeneration and recombination of multiexcitons in semiconductor nanocrystals: implications for lasing and solar energy conversion. *The Journal of Physical Chemistry B*, 110(34):16827–16845, 2006.

[23] R.D. Schaller, M.A. Petruska, and V.I. Klimov. Tunable near-infrared optical gain and amplified spontaneous emission using pbse nanocrystals. *The Journal of Physical Chemistry B*, 107(50):13765–13768, 2003.

[24] V.I. Klimov, A.A. Mikhailovsky, D.W. McBranch, C.A. Leatherdale, and M.G. Bawendi. Quantization of multiparticle auger rates in semiconductor quantum dots. *Science*, 287(5455):1011–1013, 2000.

[25] H. Htoon, J.A. Hollingsworth, A.V. Malko, R. Dickerson, and V.I. Klimov. Zero-to one-dimensional transition and auger recombination in semiconductor quantum rods. In *Quantum Electronics and Laser Science Conference*, page QTuA4. Optical Society of America, 2003.

[26] D. Chattarji. *The theory of Auger transitions*. Elsevier, 2012.

[27] P.T. Landsberg. *Recombination in semiconductors*. Cambridge University Press, 2003.

[28] D.I. Chepic, Al. L. Efros, A.I. Ekimov, M.G. Ivanov, V.A. Kharchenko, I.A. Kudriavtsev, and T.V. Yazeva. Auger ionization of semiconductor quantum drops in a glass matrix. *Journal of Luminescence*, 47(3):113–127, 1990.

[29] V.I. Klimov and D.W. McBranch. Auger-process-induced charge separation in semiconductor nanocrystals. *Physical Review B*, 55(19):13173, 1997.

[30] V.A. Kharchenko and M. Rosen. Auger relaxation processes in semiconductor nanocrystals and quantum wells. *Journal of Luminescence*, 70(1):158–169, 1996.

[31] J.M. Pietryga, K.K. Zhuravlev, M. Whitehead, V.I. Klimov, and R.D. Schaller. Evidence for barrierless auger recombination in pbse nanocrystals: A pressure-dependent study of transient optical absorption. *Physical Review Letters*, 101(21):217401, 2008.

[32] V.I. Klimov. Spectral and dynamical properties of multiexcitons in semiconductor nanocrystals. *Annu. Rev. Phys. Chem.*, 58:635–673, 2007.

[33] R.D. Schaller and V.I. Klimov. High efficiency carrier multiplication in pbse nanocrystals: implications for solar energy conversion. *Physical Review Letters*, 92(18):186601, 2004.

[34] V.I. Klimov, S.A. Ivanov, J. Nanda, M. Achermann, I. Bezel, J.A. McGuire, and A. Piryatinski. Single-exciton optical gain in semiconductor nanocrystals. *Nature*, 447(7143):441–446, 2007.

[35] D. Oron, M. Kazes, and U. Banin. Multiexcitons in type-ii colloidal semiconductor quantum dots. *Physical Review B*, 75(3):035330, 2007.

[36] M. Zavelani-Rossi, M.G. Lupo, F. Tassone, L. Manna, and G. Lanzani. Suppression of biexciton auger recombination in cdse/cds dot/rods: Role of the electronic structure in the carrier dynamics. *Nano Letters*, 10(8):3142–3150, 2010.

[37] Y.S. Park, A.V. Malko, J. Vela, Y. Chen, Y. Ghosh, F. Garcia-Santamaria, J.A. Hollingsworth, V.I. Klimov, and H. Htoon. Near-unity quantum yields of biexciton emission from CdSe/CdS nanocrystals measured using single-particle spectroscopy. *Physical Review Letters*, 106(18):187401, 2011.

[38] Y. Chen, J. Vela, H. Htoon, J.L. Casson, D.J. Werder, D.A. Bussian, V.I. Klimov, and J.A. Hollingsworth. giant multishell CdSe nanocrystal quantum dots with suppressed blinking. *Journal of the American Chemical Society*, 130(15):5026–5027, 2008.

[39] F. García-Santamaría, Y. Chen, J. Vela, R.D. Schaller, J.A. Hollingsworth, and V.I. Klimov. Suppressed auger recombination in giant nanocrystals boosts optical gain performance. *Nano Letters*, 9(10):3482–3488, 2009.

[40] G.E. Cragg and Al.L. Efros. Suppression of auger processes in confined structures. *Nano Letters*, 10(1):313–317, 2009.

[41] J.I. Climente, J.L. Movilla, and J. Planelles. Auger recombination suppression in nanocrystals with asymmetric electron–hole confinement. *Small*, 8(5):754–759, 2012.

[42] V.I. Klimov. Multicarrier interactions in semiconductor nanocrystals in relation to the phenomena of auger recombination and carrier multiplication. *Annu. Rev. Condens. Matter Phys.*, 5(1):285–316, 2014.

[43] V.I. Klimov, A.A. Mikhailovsky, S. Xu, A. Malko, J.A. Hollingsworth, C.A. Leatherdale, H.J. Eisler, and M.G. Bawendi. Optical gain and stimulated emission in nanocrystal quantum dots. *Science*, 290(5490):314–317, 2000.

[44] D.J. Norris, A. Sacra, C.B. Murray, and M.G. Bawendi. Measurement of the size dependent hole spectrum in CdSe quantum dots. *Physical Review Letters*, 72(16):2612, 1994.

[45] V.I. Klimov. Optical nonlinearities and ultrafast carrier dynamics in semiconductor nanocrystals. *The Journal of Physical Chemistry B*, 104(26):6112–6123, 2000.

[46] C. Dang, K. Roh, J. Lee, C. Breen, J.S. Steckel, S. Coe-Sullivan, and A. Nurmikko. Stimulated emission in red, green, and blue from colloidal quantum dot films by single exciton optical gain. In *IEEE Photonics Conference 2012*, 2012.

# Chapter 3

# Spectroscopy of Optical Gain in Colloidal Quantum Dots: Dominance of Single Exciton States

## 3.1 Introduction

Theoretical predictions that the electron-hole pair quantum confinement effect in quasi-zero dimensional semiconductor quantum dots [12**?** **?** , 13] provides intrinsically lower excitation thresholds compared to bulk crystals for lasers in low-loss media have become a technological reality. Epitaxially grown InGaAs quantum dot diode lasers have achieved ultralow current density ($J_{th} < 20$ A/cm$^2$) [**?** ]. Using very different methods of solution-based colloidal chemistry [**?** **?** **?** ], nanocrystals from the II-VI semiconductor family have recently emerged as important technologically viable candidates as visible fluorophores across the RGB with near-unity photoluminescence quantum yield, high color purity, monodisperse size distribution (<5%). In

addition to display applications, research demonstrations abound in applying CQDs as bio-labels [? ? ], in photovoltaics [? ? ], and in light-emitting diodes [? ? ? ? ]. In the laser work, there has been advances towards practical CQD lasers in such varying configurations as optically pumped VCSEL [4], DFB lasers across the RGB [? ? ], and photonic crystal coherent emitters [? ? ]. In addition, II-VI colloidal nanocrystalline platelet researches were recently published where ASE has been reported to onset at very low optical excitation levels [? ? ].

Given this relative maturation of CQD research and to assess prospects of functional laser devices emerging from contemporary work, it is important to investigate those electronic states which are recruited for population inversion as well as fundamental competing non-radiative mechanisms. What is beyond dispute is that due to the strong spatial quantum confinement, the inelastic three- and many-body Auger recombination processes ($\tau_{Auger} \sim$ few tens to few hundreds of pico-second) lead to profound depletion of any excitonic gain. Rather universally, the biexcitonic Auger process is about two orders of magnitude faster than spontaneous emission rates ($\sim$ 10 ns) for typical high quantum yield CdSe-based CQDs [24]. In one commonly accepted model, in order for a single ideal CQD, to reach population inversion, two electron-hole pairs (biexciton) must be first generated across the energy gap for light amplification. In the case of CQD ensembles, application of Poisson statistics such inversion constraint requires that <N> greater than 1, where <N> is the number of excitons per CQD on average and <N> = 1 correspond to the transparent state where absorption and stimulated emission rates are equal [24? ]. In such multiexcitonic cases, to avoid premature gain depletion by the Auger processes, majority of prior experiments have reported ASE under transient excitation in II-VI CQDs with ultrashort pulsed optical pumping (in femtosecond regime). Such extreme transient excitation conditions are of course impractical for compact low-cost RGB laser devices which the colloidal II-VI materials are candidates for competing

with other recently emerging solution-growth colloidal materials, most notably the organo-perovskites [? ? ].

One way to reduce the threshold for the population inversion has been proposed by using core-shell engineered type-II CQDs with Stark effect [34] whereby a sufficient positive biexciton binding energy is introduced by a local electric field to break the balance between the absorption and emission [34? ]. In this case, the optical transparency can be achieved at <N> on the order of 2/3. While thereby taking advantages from the single exciton gain regime, type-II CQDs have reduced spatial overlap between the electron and hole wave functions, leading to significant reduction of photoluminescence efficiency, and gain performance. Different from the CQD structure with three dimensional confinement, other nanocrystal structure such as colloidal quantum rods [? ] or colloidal nanoplatelets [? ? ], the latter has shown a milestone toward colloidally synthesized optical gain media with continuous wave operation. The strong oscillation strength combined with weak confinement (reduced Auger loss) in this two dimensional system demonstrated superior performance. But lack of strong confinement does not allow to control the emission spectrum in the broad range as CQD systems.

By contrast, we have focused on the engineering of type-I CdSe-based CQDs to access the single exciton regime of population inversion and optical gain by taking advantage of the finite Stokes shift between the absorption and emission resonances in the lowest exciton state, specifically in tailored nanocrystals which possess a narrow linewidth, and well-isolated 1S exciton resonance at room temperature. While varying Stokes shifts have been widely discussed and analyzed in II-VI CQDs in the past decade [? ? ? ? ], ranging from few meVs to hundreds of meVs, it can be suggested that there is an optimal range for a Stokes shift where single-exciton inversion can overcome self-absorption, yet possess sufficient oscillator strength for useful optical gain. In densely packed thin films of such high quantum yield media

where the 1S exciton state linewidth can approaches near homogeneously broadened limit due to high monodispersity, the fabrication of monolithically integrated optical cavity structures has been demonstrated as CQD VCSELs in the red and green operating at excitation levels which empirically point to a dominant role of single exciton gain given the low optical pumping thresholds [4]. For example, proof-of-concept surface-emitting CQD DFB lasers in RGB colors with high spatial coherence and good power conversion efficiency were recently demonstrated using a compact optical pumping source [**?** ].

We studied the optical gain near the 1S(e)-$1S_{2/3}$(h) exciton resonance via transient spectroscopic methods applied to two different type-I CQD core-shell nanocrystals, each of which however possessed the attributes listed above (including luminescence quantum yield in the red at room temperature in the range of $0.8 \sim 0.9$). We chose the structural details of the two core/shell structures to be distinctly different in order to test whether the single exciton gain hypothesis might be a general phenomenon.

## 3.2 Structural characteristics of CQDs

The CQDs were synthesized by well-established methods of organometallic synthesis [**?** ], under strictly controlled temperature and growth rate conditions. Figure 3.1(a) and (b) show the structural contrasts between the two classes of CQDs from their transmission electron microscope (TEM) images. Figure 3.1(a) shows "pyramidal" type-I CdSe/ZnCdS core/shell CQDs with average diameter of 5.2 nm. The shell thickness was approximately 1 nm ($\sim$ monolayer) and its Cd alloy composition was approximately 0.5 which was estimated by energy-dispersive X-ray spectroscopy (EDX) analysis as seen in Fig. 3.2(a). Amine-based monolayer organic ligands ensured the high luminescence quantum yield and helped in the subsequent

self-assembly of the solid films.

By contrast, Fig. 3.1(b) shows the TEM image of a CQD cluster of nearly spherical shape, composed of a CdSe/ZnS/$Zn_{0.65}Cd_{0.35}S$ core/shell/shell structure. Here the chemical compositions of the outermost shell were also estimated by the same technique in Fig. 3.2(b). Now a thicker ZnCdS outermost shell (∼2.7 nm) was grown on a thin ZnS intermediate layer (∼1.5 nm), resulting on an average nanocrystal diameter of 13.6 nm. Both classes of CQDs could be extracted into solution form at exceptionally high concentrations (∼150 mg/ml) without aggregation in a non-polar solvent (Toluene) and while maintaining high quantum yield, forming the starting materials for fabricating the thin film lasing media.

The films were made by spin-casting concentrated CQD solutions on quartz substrates at room temperature whereupon (at optimized spin speed) they had a propensity of forming self-assembled, closely packed solid thin films shown in Fig. 3.1(c). The best films were typically approximately 250 nm in thickness with an effective refractive index (measured by ellipsometry at 633 nm) 1.75 and 1.90 for pyramidal and spherical CQD cases, respectively. These values correspond with the packing density of the films about 50%, and 65% which are remarkably high (and exclude the finite thickness effects of the ligands), compared to the theoretical maximum case for identical hard spheres ( 74%). Such high packing fractions are the important factor for obtaining optical gain from these thin films which we utilized in optically pumped laser experiments [4**?** ]. Figure 3.1(d) and (e) are X-ray diffraction (XRD) patterns of CdSe/ZnCdS and CdSe/ZnS/ZnCdS CQDs respectively, verifying that although the geometrical shapes of the two classes of CQDs were quite different in symmetry, they possessed the same underlying wurtzite nanocrystal structure. The peaks in XRD patterns are resolved well enough for this conclusion, in spite of the small sizes of the individual CQDs for XRD experiments, which further indicates the good crystalline quality of the nanocrystal preparations.

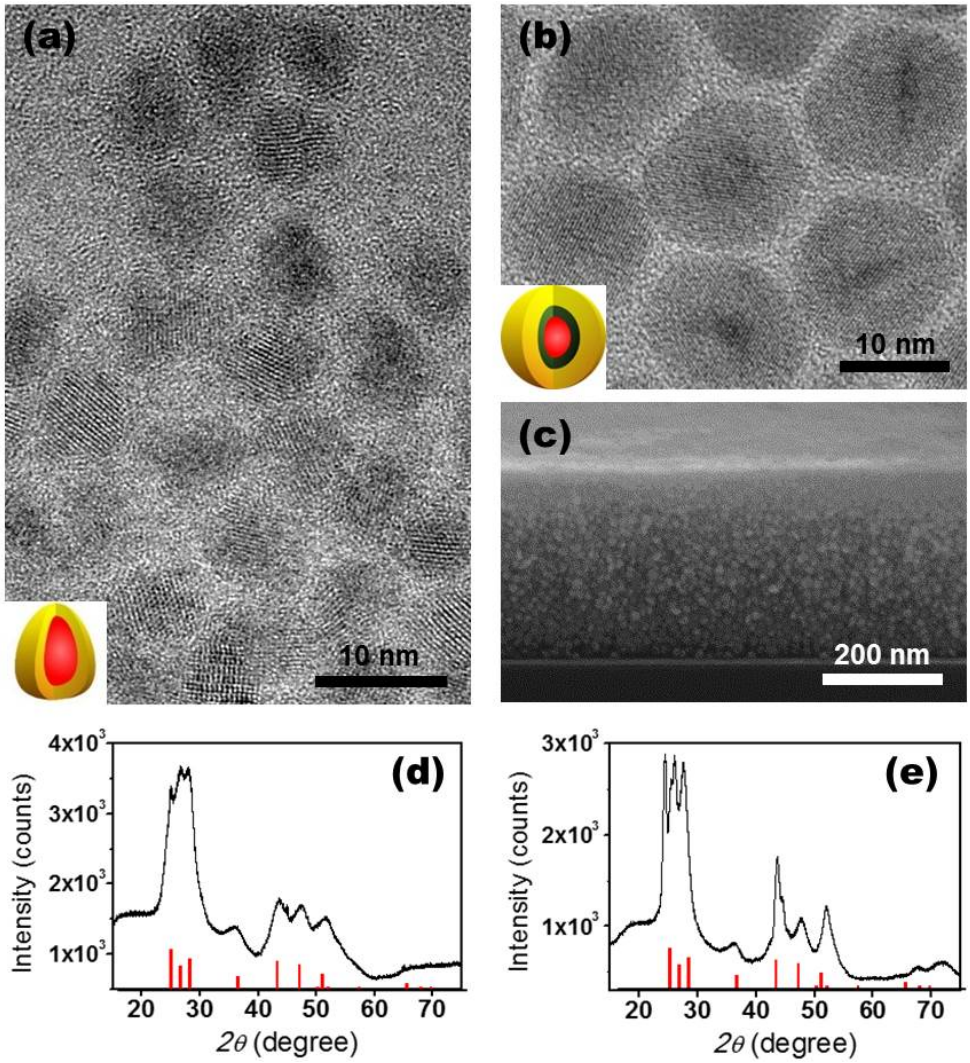


**Figure 3.1:** Structural characteristics of CQDs and their spin-cast closely packed films. TEM images of individual (a) CdSe/ZnCdS core/shell CQDs showing pyramidal shape anisotropy, and (b) spherical shaped CdSe/ZnS/ZnCdS CQDs. Insets are schematics of each CQD materials. (Red, green and yellow indicate CdSe, ZnS, and ZnCdS, respectively) (c) Scanning electron microscope (SEM) image of a closely packed CQD film on silicon substrate. Individual dots are self-assembled to form an optically smooth top surface. XRD patterns for (d) CdSe/ZnCdS and (e) CdSe/ZnS/ZnCdS CQDs, indicating wurtzite crystal structure for both CQDs. The red stick patterns on the bottom represent the standard peak positions for bulk wurtzite CdSe.

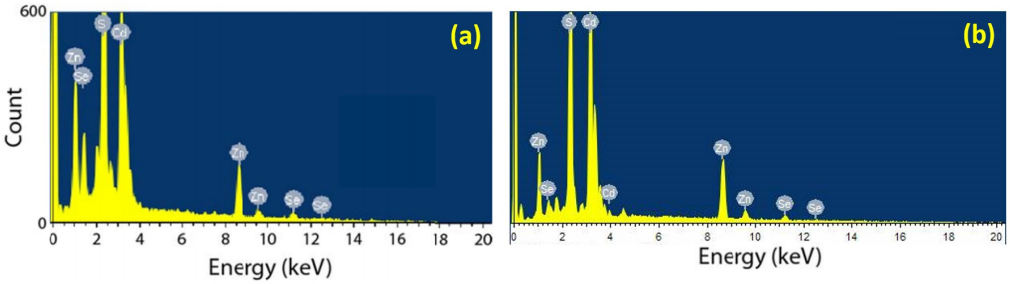


**Figure 3.2:** EDX analysis of the (a) CdSe/ZnCdS and (b) CdSe/ZnS/ZnCdS CQD films showing the chemical compositions in the core/shell structures. (reprinted from [4])

| **Element** | **CdSe/ZnCdS** | | **CdSe/ZnS/ZnCdS** | |
|---|---|---|---|---|
| | Weight (%) | Atomic (%) | Weight (%) | Atomic (%) |
| S | 22.40 | 44.91 | 25.41 | 49.93 |
| Zn | 20.26 | 19.92 | 16.90 | 19.36 |
| Se | 9.78 | 7.97 | 2.72 | 2.07 |
| Cd | 47.56 | 27.20 | 54.98 | 30.64 |
| Total | 100.00 | 100.00 | 100.00 | 100.00 |

**Table 3.1:** Weight and atomic percentages of individual elements in CdSe/$Zn_xCd_{1-x}S$ and CdSe/ZnS/$Zn_xCd_{1-x}S$ CQDs.

## 3.3 Optical characteristics of CQDs

### 3.3.1 Absorbance and photoluminescence

Before going into the detail gain dynamics of the CQDs, this section briefly describes the fundamental optical characteristics of the two contrasting CQD materials. Figure 3.3 shows the absorption and spontaneous emission spectra (PL under Xenon flash lamp filtered at 400 nm) from the two classes of dens solid CQD films at room temperature. Both 250 nm thick films display very well-defined and isolated lowest 1S(e)-$1S_{3/2}$(h) exciton absorption peak, as well as higher order resonances at least up to n = 3. The PL spectra are red-shifted with respect to their lowest absorption peaks by 52 and 17 meV for CdSe/ZnCdS (Pyramidal shape) and CdSe/ZnS/ZnCdS (Spherical shape) CQDs, respectively. The spectral linewidths and the Stokes shifts are seen to be somewhat different for the two preparations; While CdSe/ZnCdS CQDs have a large Stokes shift, CdSe/ZnS/ZnCdS CQDs show very narrow PL linewidth (27 meV of half-width at half-maximum (HWHM)). However, both CQDs maintain an approximate mutual relationship between these two critical parameters which are key for achieving single exciton driven optical gain without necessity of multiexcitonic processes. This is reflected in their low optical pumping lasing thresholds such as our previous red, green and blue (RGB) distributed feedback (DFB) laser performance with excellent spatial and temporal coherence [4**? ?** ].

### 3.3.2 Single-dot photoluminescence spectroscopy

In order to investigate the inhomogeneous broadening and monodispersity of the CQDs, PL spectra from individual CQDs were measured. Original CQDs with dense concentration ($\sim$ 150 mg/ml) were highly diluted with Toluene solvent and sonicated, so that the spacing between each CQD was far enough when they were spin-cast on a cover slip. The 365 nm line from a mercury lamp was used for the excitation

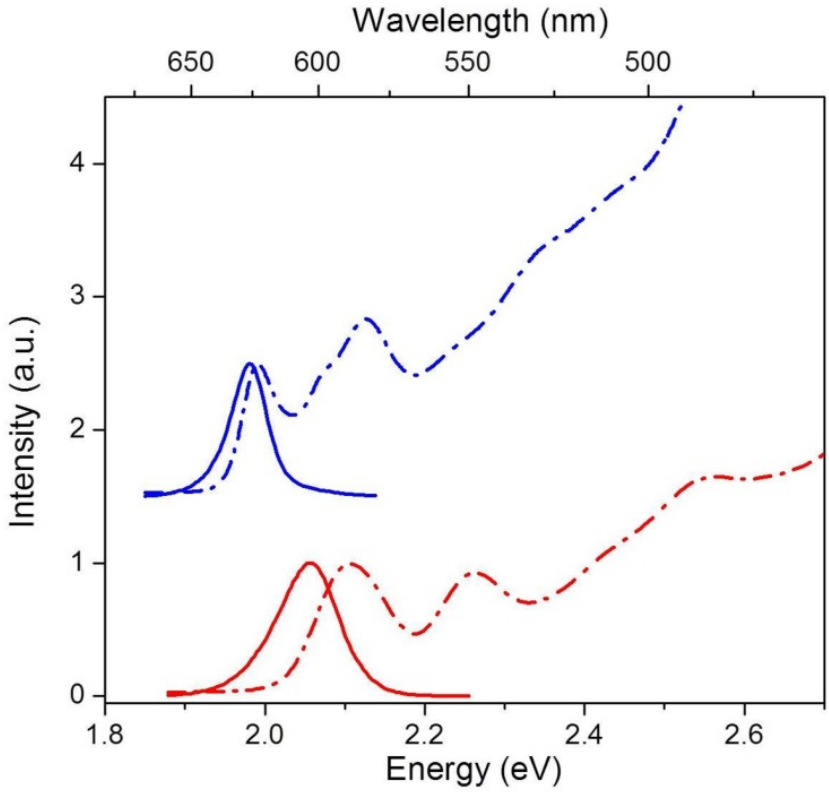


**Figure 3.3:** Absorption (dashed) and PL (solid) spectra from close-packed CQD (blue for CdSe/ZnS/ZnCdS and red for CdSe/ZnCdS) films at room temperature.

source for the CQDs in the fluorescence microscope system. Blinking phenomenon has been observed from the individual CQDs, which can be a direct evidence of a single level CQD. Figure 3.4 is a fluorescence microscope image of diluted individual CQDs on cover slip. The distance between the neighbor CQDs is far enough not to be re-absorbed by adjacent CQDs.

PL spectra from 10 single CQDs are plotted in Figure 3.5. Obviously, the PL peaks for the pyramidal shaped CQDs are more widely distributed than for the spherical shaped dual shell CQDs. The standard deviation values of peak PL positions when fitted with Gaussian curves are 17 and 4.1 meV for CdSe/ZnCdS and CdSe/ZnS/ZnCdS CQDs respectively. In addition, the HWHM values of PL show larger difference when compared between the single and ensemble CQD for pyramidal shaped CQDs. Note that the HWHM of PL for the ensemble of CdSe/ZnCdS CQD is 43 meV, while it is just 30 meV for the single CQD case. However, this difference for CdSe/ZnS/ZnCdS CQDs is just 3 meV (27 meV for the ensemble and 24 meV for the single CQDs). These results suggest that the spherical shaped dual shell CQDs are highly monodispersive to yield low inhomogeneous broadening.

## 3.4 Experimental apparatus: Ultrafast laser pump-probe technique

To study and characterize ultrafast electronic dynamics of materials such as semiconductors and photochemical molecules, pump-probe laser spectroscopy is a useful technique also known as time-resolved spectroscopy. Most relaxation processes occur in the time scale longer than 100 fs. Therefore, usually femto-second laser can be used to excite the samples instantly. In this technique, the pulses from the ultrafast pulsed laser are split into two beams. A stronger one is used as pump beam to populate the sample into an excited state. Then it relaxes down to a ground state

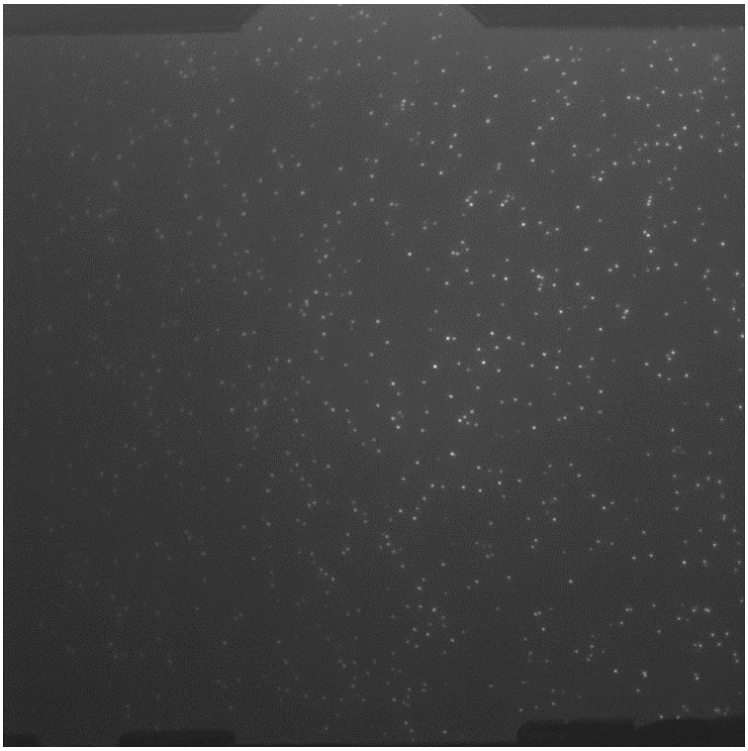

**Figure 3.4:** Fluorescence microscope image of diluted CQDs on cover slip using x 100 magnification objective lens.

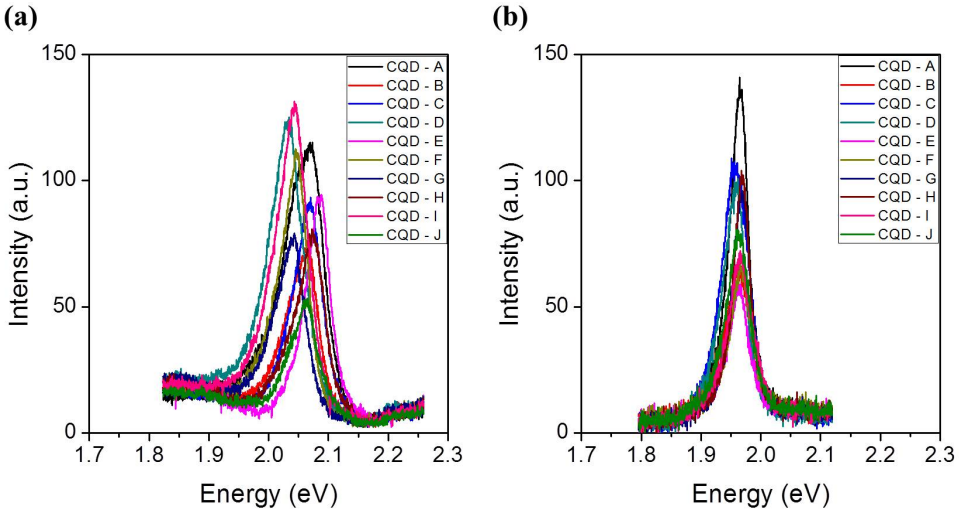


**Figure 3.5:** PL spectra from 10 single (a) CdSe/ZnCdS and (b) CdSe/ZnS/ZnCdS CQDs.

in picosecond time regime. Another beam (probe) which is delayed with respect to the pump beam probes the pump-induced changes of the sample by measuring the reflectance, transmittance, or absorbance as a function of time.

Figure 3.6 shows the experimental setup used in the study of the optical gain dynamics in the engineered core-shell structure CQDs. An continuous-wave solid-state laser at 532 nm pumps a passively mode-locked Ti:sapphire laser. Output beams from the amplified Ti:sapphire laser was frequency-doubled to be used for pump pulses whose wavelength, pulse duration and repetition rate are 400 nm, 100 fs, and 100 kHz respectively. These pulses were modulated by an optical chopper with phase-locked feedback loop for low frequency drift and jitter. The probe pulses were acquired by using fraction of the Ti:sapphire laser output for continuum white light generation, time-delayed by a linear stage with a retro-reflector, and spectrally narrowed after passing through a monochromator acting as a tunable filter. Then, the pump and probe pulses were focused to circular spots (75 and 30 $\mu$m in diameter, respectively) on the surface of the close-packed CQD thin films. The small spot size was used to avoid any confounding effects from ASE. Then transmitted and reflected probe beams at the CQD films were collected by a photodetector and analyzed by a lock-in amplifier, averaging over many pulses.

## 3.5 Experimental results

### 3.5.1 Transient absorption spectra

One view of key experimental results by gain spectroscopy is shown in Fig. 3.7 where the (non-linear) transient absorption spectrum of the probe is expressed as the sum of the low intensity linear absorption $\alpha(\omega)$ and the pump induced contribution $\Delta\alpha(\omega,t)$ for the two types of the solid densely packed CQD films. The spectral summaries of Fig. 3.7 are snapshots measured at 2 ps after the ultra-short pulsed excitation,

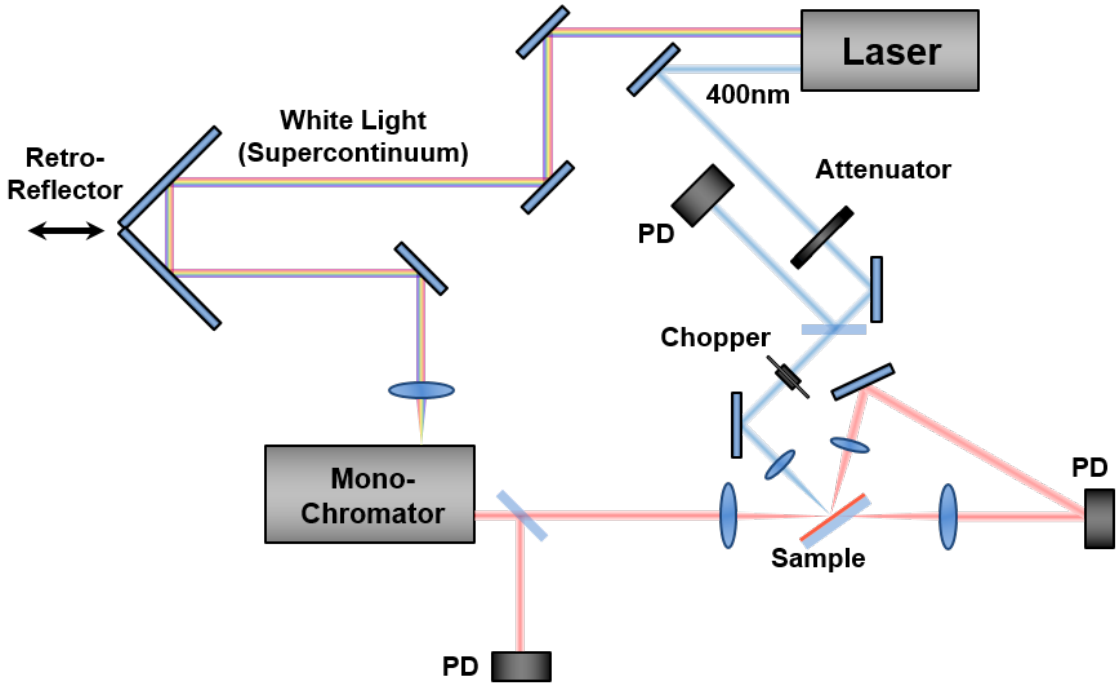


**Figure 3.6:** Schematic illustration of the ultrafast laser pump-probe experiment setup.

where the thermalization of the internal exciton bath has taken place, but prior to any population decay by exciton recombination, including any Auger processes. The negative values of $\alpha(\omega) + \Delta\alpha(\omega,t)$ provide a direct measure of the presence of optical gain. For the pyramidal CdSe/ZnCdS CQDs, the optical gain is seen to onset on the red-shifted flank of the PL spectrum when the pump fluence reaches the level corresponding to the average number of e-h pairs per CQD of $\langle N \rangle = 0.53 \pm 0.01$, that is at level of excitation which is well within the single exciton gain regime. We calculated values for $\langle N \rangle$ by precisely calibrating our instrumentation to measure the number of photons absorbed by the CQD film per pump pulse [4]. Similarly, for spherical dual-shell CdSe/ZnS/ZnCdS CQDs, the optical gain emerges at when $\langle N \rangle = 0.69 \pm 0.02$. Although this is slightly higher than those for CdSe/ZnCdS CQDs it is empirically evident that these CQD films also demonstrate ready access to optical gain in the single exciton regime.

### 3.5.2 Optical gain decay dynamics via time-resolved transient absorption spectroscopy

Figure 3.8 shows time-resolved transient absorption under various excitation levels at fixed wavelength. The probe pulses were tuned at 2.02 and 1.93 eV, where the optical gain first emerges for the CdSe/ZnCdS and CdSe/ZnS/ZnCdS CQDs, respectively (in Fig. 3.7). For ease of viewing, the vertical axis is inverted so that optical gain occurs when $-\Delta\alpha/\alpha > 1$ in these plots. For both types of CQD samples, the transient absorption curves show a single exponential decay rate at low excitation levels as would be expected for a single exciton recombination process (i.e. $\langle N \rangle = 0.45$ and 0.52 in Fig. 3.8(a) and (b), respectively). However, as the excitation levels increase, a faster decay rate emerges, which we assigned to the much studied multi-excitonic Auger process. The Auger rates from our experimental transient absorption data turned out to be 117 ± 1 ps (CdSe/ZnCdS CQDs) and 319 ± 9

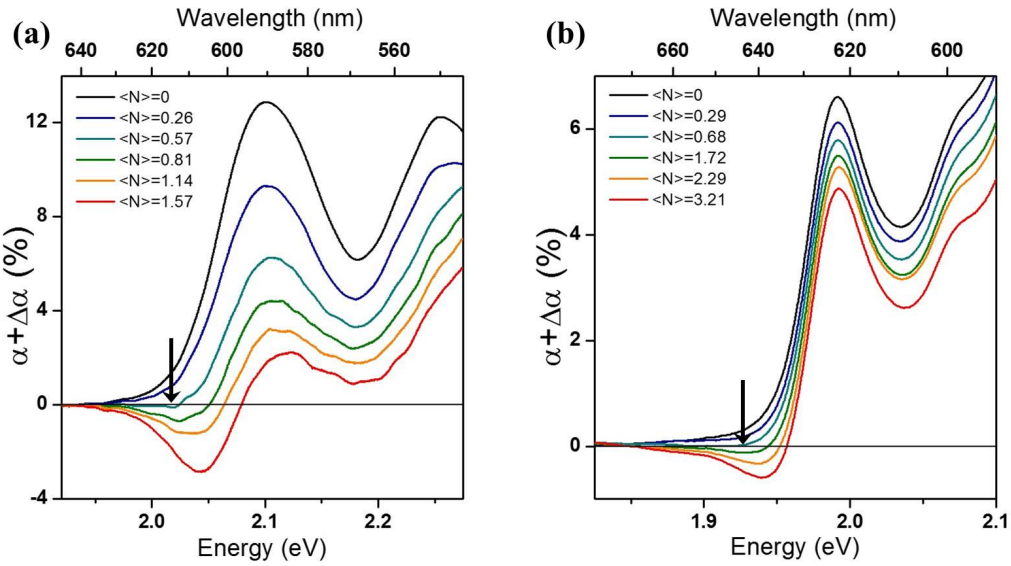


**Figure 3.7:** Transient absorption spectra of (a) CdSe/ZnCdS and (b) CdSe/ZnS/ZnCdS CQD films at various excitation levels. The optical gain occurs at $\alpha + \Delta\alpha < 0$. Threshold values for the optical gain are approximately <N> $\sim$ 0.5 and 0.7 for CdSe/ZnCdS and CdSe/ZnS/ZnCdS CQD films, respectively. Both CQD films' stimulated emissions are well within the single exciton gain regime. Arrows in the graphs indicate the location where the optical gain begins to emerge.

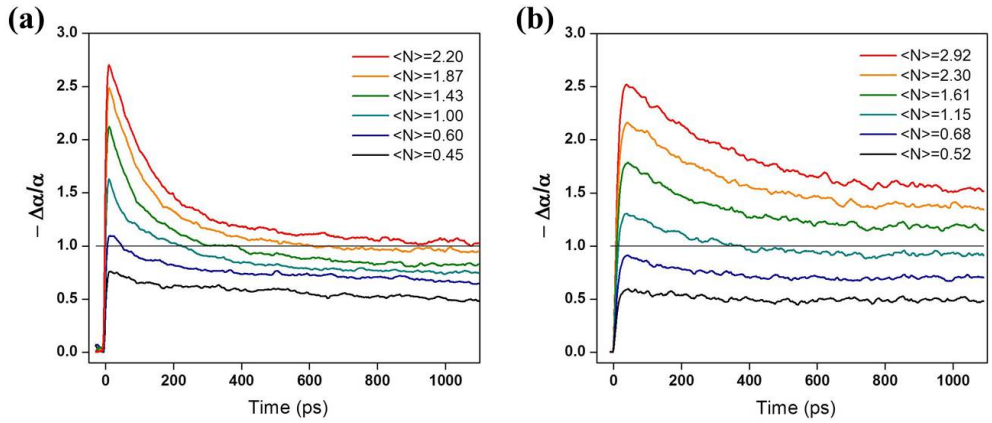


**Figure 3.8:** Time-resolved transient absorption measured at 2.02 and 1.93 eV where the optical gain arises for (a) CdSe/ZnCdS and (b) CdSe/ZnS/ZnCdS CQD films at various excitation levels. Under high optical excitation, the optical gain decay lasts more than 1 ns, two orders of magnitude longer than the Auger process. The estimated Auger rates are 117 and 319 ps for CdSe/ZnCdS and CdSe/ZnS/ZnCdS CQDs, respectively. At low optical excitation, the decay curves exhibit just slow exponential behavior ($\sim$ 10 ns).

ps (CdSe/ZnS/ZnCdS CQDs). Extensive theoretical and experimental studies have suggested that the Auger recombination process is largely dependent on the sharpness of the electronic confinement potential determined by the core/shell structure of CQDs [40**? ?** , 41]. Further, smoothing out the confinement potential can reduce the Auger recombination rate significantly in comparison to a confinement with an abrupt boundary [40].

These experimental results, coupled to the demonstrated low-threshold lasing in optical resonator structures of both types of CQDs, thus suggest empirically that the single exciton mechanism is not strictly dependent on a single sample effect, a point of relevance given the overall challenges in precisely controlling the reproducibility in the growth chemistry of colloidal nanocrystals. We suggest that single exciton optical gain mechanism can be a rather general, and perhaps dominant electronic source of gain in II-VI CQD lasers - if certain conditions are satisfied as discussed next.

### 3.5.3 Discussions

While we are not able to provide a detailed physical model related to specifics of the CQD structure, qualitative plausibility arguments can be made as follow. As going from bulk to low-dimensional semiconductors such as two-dimensional quantum wells (also quantum nanoplatelets, related to quasi-two dimensional structure) and quasi-zero dimensional quantum dots, the Coulomb interaction between the charge carriers gets significantly enhanced due to the quantum confinement effect. This, in turn results in the increase of the exciton binding energy. Focusing on the microscopics of the electron-hole interaction, the exchange portion of the indirect Coulomb interaction resulting in the energy difference between the spin-singlet and triplet exciton is also enhanced, providing one specific mechanism for the Stokes shift, apart from phonon and extrinsic effects [**?** ]. For CdSe-based quantum dots in strong

confinement regime, the Stokes shift can be introduced by the intrinsic asymmetry of the wurtzite structure and the spin-orbit coupling. Note that the CdSe/ZnCdS CQDs analyzed in this study exhibit strong shape anisotropy and wurtizte crystal structure as seen in Fig. 3.1(a) and (d), presenting a large magnitude of Stokes shift ($\sim$ 52 meV). The widely varying, preparation-dependent Stokes shifts have been extensively discussed and analyzed in II-VI CQDs in the past decade [40**?** , 41] ranging from few meV to hundreds of meV. Here, we believe that there is an optimal range for a Stokes shift where single-exciton inversion can overcome self-absorption, yet possess sufficient oscillator strength for useful optical gain.

Figure 3.9 shows the role of the Stokes shift in the single exciton gain for the CdSe/ZnCdS CQDs. By decreasing the temperatures, we were able to increase the Stokes shift, while reducing the linewidths of the optical transitions (PL and absorption) as shown in Fig. 3.9(e). This reduces the overlapping of emission and absorption spectra, which is beneficial for lowering the ASE thresholds. Figure 3.9(a-c) indicate that the ASE peaks emerge at different spectral location relative to the PL peak. At room temperature, the ASE peak is red-shifted from the PL peak (Fig. 3.9(a)). When T = 175 K, it is located at the center of the PL peak (Fig. 3.9(b)). Then, at T = 5 K, where the magnitude of the Stokes shift ($\sim$ 72 meV) is almost comparable to the PL linewidth ($\sim$ 74 meV), the ASE peak is on the blue side of the PL peak (Fig. 3.9(c)). At low temperatures, finite interaction among the close-packed CQD films red-shifts the PL peak, but does not affect the very fast ASE process (ASE lifetime $<$ 16 ps), which causes an effective ASE blue shift. With preferable conditions with the Stokes shift, the ASE thresholds decrease monotonically from 720 $\mu$J/cm$^2$ at room temperature to 280 $\mu$J/cm$^2$ at T = 5 K (Fig. 3.9(d)).

Recently quasi-two dimensional quantum nanoplatelets have realized ASE at very low optical excitation regime [**?** **?** ]. The quantum confinement occurs only for

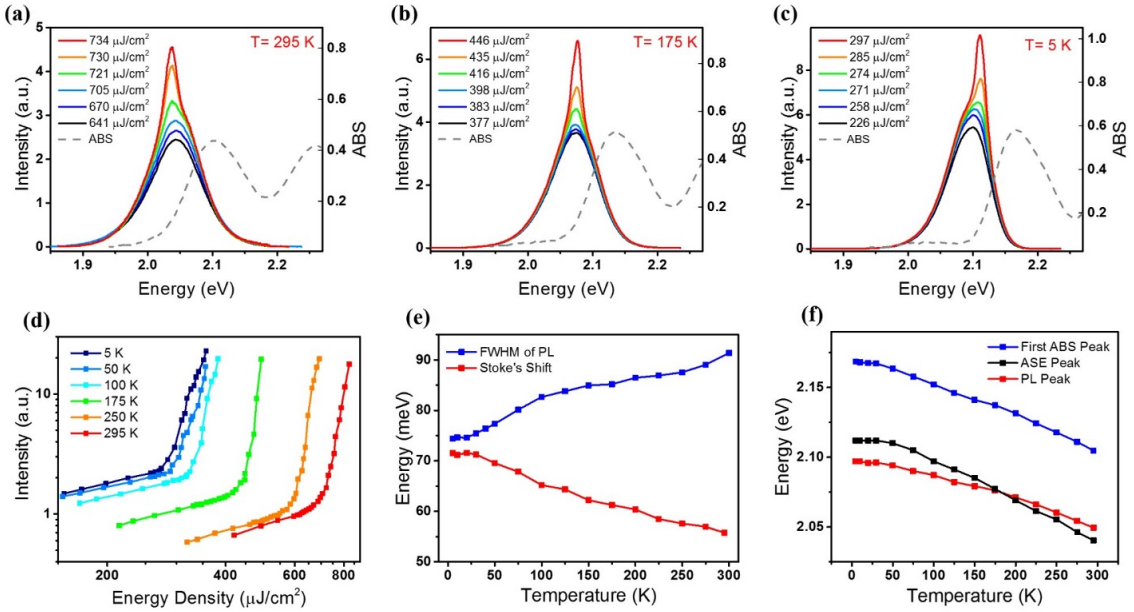


**Figure 3.9:** Tuning Stokes shift by temperature for adjusting positions of the ASE spectra with respect to the PL spectra. (a-c) PL, ASE and absorption spectra from CdSe/ZnCdS CQD film at different temperatures: 295 K, 175 K, and 5 K, respectively. (d) The emission intensity of edge emitted ASE signals in stripe excitation configuration as a function of pumping energy density at various temperatures. (e) The Stokes shift and the linewidth of the PL of the CQD film as a function of temperature. (f) The location of the peaks of the PL, ASE and the first absorption spectra of the CQD film.

the one dimension, enhancement of the Coulomb interaction and exciton binding energy is not as significant as for the three dimensional confinement regime. Yet, the strength of the exciton coupling with the emitted photons can be affected to shorten the radiative decay time and result in a giant oscillator strength transition [5]. Importantly, the precise control over the thickness of the quantum nanoplatelets can be achieved by colloidal-atomic layer deposition technique providing very narrow inhomogeneous broadening in their emission spectra (full width at half maximum (FWHM) $\sim$ 40 meV), which is a possible attribute for the low ASE threshold levels [**?** ]. Our spherical shaped CdSe/ZnS/ZnCdS CQDs also show very narrow PL linewidth due to high degree of monodispersity. According to the single CQD PL analysis, the average FWHM values of PL for the individual and ensemble CQDs only differ by 5 meV (49 and 54 meV). Thus, we attribute the emergence of single exciton optical gain to the narrow linewidth of the absorption and PL spectra, or the optical homogeneity despite the relatively small Stokes shift in the spherical shaped CQD films.

It has been reported that for close-packed CQD films, the PL quantum yield usually decreases due to direct dipole-dipole interaction among the nearest quantum dots [**?** **?** ]. However, note that according to our photocurrent measurements from the CQD films, there was no direct evidence of the interaction between the neighboring quantum dots. As a consequence, the PL quantum yield still reaches up to 90%. The other property of the single exciton gain mechanism that can be found from the time-resolved transient absorption data is the long gain decay characteristic which can last more than 1 ns at sufficient excitation levels. According to Fig. 3.7, the optical gain turns off after 220 and 380 ps at <N> = 1.00 and 1.15 of excitation for the CdSe/ZnCdS and CdSe/ZnS/ZnCdS CQDs, respectively. However, as the excitation increases further, the optical gain can last one order of magnitude longer than the Auger recombination rate for both CQDs. In fact, with ultrafast pumping pulses,

there exists finite amount of CQDs with multi-exciton states even at relatively low excitation levels. According to the Poisson distribution of excitons per CQD:

$$P(n) = \frac{< N >^n e^{-<N>}}{n!} , \tag{3.1}$$

where <N> is the average number of excitons per CQD and n is the number of excitons in a single CQD, the fractions of the multi-exciton states in CQDs, are 12% and 65% for the excitation levels of <N> = 0.6 and 2.2, respectively for example. The recombination process for the excitons in CQDs occurs as a sequence of quantized steps from multi-exciton to finally single-exciton state [24]. Thus, the optical gain finally shows two exponential decay rates which correspond to the single and multi-exciton recombination. For both CQDs, while there is an initial fast multiexcitonic decay process, CQDs still retain optical gain until the multi-exciton states becomes single excitons, leading to the characteristics of long-decaying optical gain.

## 3.6 Conclusions

Studies of ASE and lasing by optical pumping from multiple types of colloidal II-VI compound semiconductor nanocrystal preparations have been reported, ranging from solution to solid films and from quantum dots to recent discovery of nanocrystalline platelets. Several microscopic models have been proposed as sources of the underlying optical gain, usually involving combinations of quantum confined multiple excitonic states. Here we focus specifically on CdSe/CdZnS and CdSe/ZnS/ZnCdS CQD thin solid films and the discovery of single excitons as a prime, low-excitation source of optical gain (i.e. the excitation regime with single electron-hole pair occupancy per quantum dot). In the types of very densely packed CQD films, optical gain dominated by single exciton gain enable robust laser operation featuring well-defined spatially coherent beams e.g. from distributed Bragg feedback resonators across the

red, green, and blue.

Here we investigate the range of applicability of the single exciton gain properties by studying quantitatively two contrasting types of CQDs by performing direct gain spectroscopy. The CQDs differ in their nanocrystal core-shell composition and shape, with approximately pyramidal and spherical geometries, respectively. Transient spectroscopic techniques enable us to measure the onset of gain at optical pumping levels corresponding to ensemble-average exciton occupancy per CQD, $\langle N \rangle = 0.5$ and 0.7 for the two types of CQD thin films. Time-resolved measurements show how optical gain persists well into the spontaneous emission time regime (nanoseconds) providing direct evidence how the non-radiative Auger recombination process ($\sim$ 100 ps) can be thwarted. Auger processes frustrate optical gain in the higher excitation, multi-exciton regime in CdSe-based and related CQDs which most reports in earlier literature have focused on. Beyond deploying densely packed films of high luminescence efficiency (quantum yield $\sim$ 90%) and nanoparticle monodispersity, we propose that access to the single exciton gain regime requires a careful spectral balance between the lowest exciton absorption resonance and its corresponding spontaneous emission maximum (Stokes shift).

# Bibliography

[1] Y. Arakawa and H. Sakaki. Multidimensional quantum well laser and temperature dependence of its threshold current. *Applied Physics Letters*, 40(11):939–941, 1982.

[2] L.E. Brus. A simple model for the ionization potential, electron affinity, and aqueous redox potentials of small semiconductor crystallites. *The Journal of Chemical Physics*, 79(11):5566–5571, 1983.

[3] Al L. Efros and Al L. Efros. Interband absorption of light in a semiconductor sphere. *Soviet Physics Semiconductors-Ussr*, 16(7):772–775, 1982.

[4] A.I. Ekimov and A.A. Onushchenko. Size quantization of the electron energy spectrum in a microscopic semiconductor crystal. *Journal of Experimental and Theoretical Physics Letters*, 40(8):1136–1139, 1984.

[5] G.T. Liu, A. Stintz, H. Li, T.C. Newell, A.L. Gray, P.M. Varangis, K.J. Malloy, and L.F. Lester. The influence of quantum-well composition on the performance of quantum dot lasers using inas-ingaas dots-in-a-well (dwell) structures. *IEEE Journal of Quantum Electronics*, 36(11):1272–1279, 2000.

[6] M.A. Hines and P. Guyot-Sionnest. Synthesis and characterization of strongly luminescing ZnS-capped CdSe nanocrystals. *The Journal of Physical Chemistry*, 100(2):468–471, 1996.

[7] O. Chen, J. Zhao, V.P. Chauhan, J. Cui, C. Wong, D.K. Harris, H. Wei, H.S. Han, D. Fukumura, R.K. Jain, and M.G. Bawendi. Compact high-quality CdSe–CdS core–shell nanocrystals with narrow emission linewidths and suppressed blinking. *Nature Materials*, 12(5):445–451, 2013.

[8] P. Reiss, M. Protiere, and L. Li. Core/shell semiconductor nanocrystals. *Small*, 5(2):154–168, 2009.

[9] M. Dahan, S. Levi, C. Luccardini, P. Rostaing, B. Riveau, and A. Triller. Diffusion dynamics of glycine receptors revealed by single-quantum dot tracking. *Science*, 302(5644):442–445, 2003.

[10] M. Stroh, J.P. Zimmer, D. Duda, T. Levchenko, K. Cohen, E. Brown, D. Scadden, V.P. Torchilin, M.G. Bawendi, and D. Fukumura. Quantum dots provide customizable fluorescence for tumor pathophysiology and drug delivery studies. In *Abstract of Papers of the American Chemical Society*, volume 229, pages U232–U233. American Chemical Society, 1155 16th St., NW, Washington D.C. 20036 USA, 2005.

[11] K.S. Leschkies, R. Divakar, J. Basu, E. Enache-Pommer, Janice E. Boercker, C.B. Carter, U.R. Kortshagen, D.J. Norris, and E.S. Aydil. Photosensitization of zno nanowires with CdSe quantum dots for photovoltaic devices. *Nano Letters*, 7(6):1793–1798, 2007.

[12] A.J. Nozik, M.C. Beard, J.M. Luther, M. Law, R.J. Ellingson, and J.C. Johnson. Semiconductor quantum dots and quantum dot arrays and applications of multiple exciton generation to third-generation photovoltaic solar cells. *Chemical Reviews*, 110(11):6873–6890, 2010.

[13] K.S. Cho, E.K. Lee, W.J. Joo, E.J. Jang, T.H. Kim, S.J. Lee, S.J. Kwon, J.Y. Han, B.K. Kim, B.L. Choi, and J.M. Kim. High-performance crosslinked colloidal quantum-dot light-emitting diodes. *Nature Photonics*, 3(6):341–345, 2009.

[14] C. Dang, J. Lee, Y. Zhang, J. Han, C. Breen, J.S. Steckel, S. Coe-Sullivan, and A.V. Nurmikko. A wafer-level integrated white-light-emitting diode incorporating colloidal quantum dots as a nanocomposite luminescent material. *Advanced Materials*, 24(44):5915–5918, 2012.

[15] B.S. Mashford, M. Stevenson, Z. Popovic, C. Hamilton, Z. Zhou, C. Breen, J. Steckel, V. Bulovic, M. Bawendi, S. Coe-Sullivan, and P.T. Kazlas. High-efficiency quantum-dot light-emitting devices with enhanced charge injection. *Nature Photonics*, 7(5):407–412, 2013.

[16] X. Yang, E. Mutlugun, K. Gao Y. Dang, C. Dev, S. T. Tan, X. W. Sun, and H.V. Demir. Highly flexible, electrically driven, top-emitting, quantum dot light-emitting stickers. *ACS nano*, 8(8):8224–8231, 2014.

[17] C. Dang, J. Lee, C. Breen, J.S. Steckel, S. Coe-Sullivan, and A.V. Nurmikko. Red, green and blue lasing enabled by single-exciton gain in colloidal quantum dot films. *Nature Nanotechnology*, 7(5):335–339, 2012.

[18] C. Dang, J. Lee, K. Roh, H. Kim, S. Ahn, H. Jeon, C. Breen, J.S. Steckel, S. Coe-Sullivan, and A.V. Nurmikko. Highly efficient, spatially coherent distributed feedback lasers from dense colloidal quantum dot films. *Applied Physics Letters*, 103(17):171104, 2013.

[19] K. Roh, C. Dang, J. Lee, S. Chen, J.S. Steckel, S. Coe-Sullivan, and A.V. Nurmikko. Surface-emitting red, green, and blue colloidal quantum dot distributed feedback lasers. *Optics Express*, 22(15):18800–18806, 2014.

[20] B. Ellis, M.A. Mayer, G. Shambat, T. Sarmiento, J. Harris, E.E. Haller, and J. Vukovic. Ultralow-threshold electrically pumped quantum-dot photonic-crystal nanocavity laser. *Nature Photonics*, 5(5):297–300, 2011.

[21] M. Nomura, N. Kumagai, S. Iwamoto, Y. Ota, and Y. Arakawa. Photonic crystal nanocavity laser with a single quantum dot gain. *Optics Express*, 17(18):15975–15982, 2009.

[22] B. Guzelturk, Y. Kelestemur, M. Olutas, S. Delikanli, and H.V. Demir. Amplified spontaneous emission and lasing in colloidal nanoplatelets. *ACS Nano*, 8(7):6599–6605, 2014.

[23] C. She, I. Fedin, D.S. Dolzhnikov, A. Demortiere, R.D. Schaller, M. Pelton, and D.V. Talapin. Low-threshold stimulated emission using colloidal quantum wells. *Nano Letters*, 14(5):2772–2777, 2014.

[24] V.I. Klimov, A.A. Mikhailovsky, D.W. McBranch, C.A. Leatherdale, and M.G. Bawendi. Quantization of multiparticle auger rates in semiconductor quantum dots. *Science*, 287(5455):1011–1013, 2000.

[25] Y. Chan, J. Caruge, P.T. Snee, and M.G. Bawendi. Multiexcitonic two-state lasing in a CdSe nanocrystal laser. *Applied Physics Letters*, 85:2460, 2004.

[26] Q. Liao, K. Hu, H. Zhang, X. Wang, J. Yao, and H. Fu. Perovskite microdisk microlasers self-assembled from solution. *Advanced Materials*, 2015.

[27] V.I. Klimov, S.A. Ivanov, J. Nanda, M. Achermann, I. Bezel, J.A. McGuire, and A. Piryatinski. Single-exciton optical gain in semiconductor nanocrystals. *Nature*, 447(7143):441–446, 2007.

[28] S.A. Ivanov, J. Nanda, A. Piryatinski, M. Achermann, L.P. Balet, I.V. Bezel, P.O. Anikeeva, S. Tretiak, and V.I. Klimov. Light amplification using inverted core/shell nanocrystals: towards lasing in the single-exciton regime. *The Journal of Physical Chemistry B*, 108(30):10625–10630, 2004.

[29] M. Zavelani-Rossi, M.G. Lupo, R. Krahne, L. Manna, and G. Lanzani. Lasing in self-assembled microcavities of CdSe/CdS core/shell colloidal quantum rods. *Nanoscale*, 2(6):931–935, 2010.

[30] Al.L. Efros, M. Rosen, M. Kuno, M. Nirmal, D.J. Norris, and M. Bawendi. Band-edge exciton in quantum dots of semiconductors with a degenerate valence band: Dark and bright exciton states. *Physical Review B*, 54(7):4843, 1996.

[31] M. Kuno, J.K. Lee, B. Dabbousi, F.V. Mikulec, and M.G. Bawendi. The band edge luminescence of CdSe nanocrystallites. In *Abstract of Papers of the American Chemical Society*, volume 213, pages 457–PHYS. American Chemical Society, 1155 16th St., NW, Washington D.C. 20036 USA, 1997.

[32] M. Nirmal, D.J. Norris, M. Kuno, M.G. Bawendi, Al.L. Efros, and M. Rosen. Observation of the" dark exciton" in CdSe quantum dots. *Physical Review Letters*, 75(20):3728, 1995.

[33] D.J. Norris, Al.L. Efros, M. Rosen, and M.G. Bawendi. Size dependence of exciton fine structure in CdSe quantum dots. *Physical Review B*, 53(24):16347, 1996.

[34] J.I. Climente, J.L. Movilla, and J. Planelles. Auger recombination suppression in nanocrystals with asymmetric electron–hole confinement. *Small*, 8(5):754–759, 2012.

[35] G.E. Cragg and Al.L. Efros. Suppression of auger processes in confined structures. *Nano Letters*, 10(1):313–317, 2009.

[36] F. Garcia-Santamaria, S. Brovelli, R. Viswanatha, J.A. Hollingsworth, H. Htoon, S.A. Crooker, and V.I. Klimov. Breakdown of volume scaling in auger recombination in CdSe/CdS heteronanocrystals: the role of the core- shell interface. *Nano Letters*, 11(2):687–693, 2011.

[37] X. Wang, X. Ren, K. Kahen, M.A. Hahn, M. Rajeswaran, S. Maccagnano-Zacher, J. Silcox, G.E. Cragg, Al.L. Efros, and T.D. Krauss. Non-blinking semiconductor nanocrystals. *Nature*, 459(7247):686–689, 2009.

[38] T. Takagahara. Effects of dielectric confinement and electron-hole exchange interaction on excitonic states in semiconductor quantum dots. *Physical Review B*, 47(8):4569, 1993.

[39] S. Ithurria, M.D. Tessier, B. Mahler, R. Lobo, B. Dubertret, and Al.L. Efros. Colloidal nanoplatelets with two-dimensional electronic structure. *Nature Materials*, 10(12):936–941, 2011.

[40] S. Ithurria and D.V. Talapin. Colloidal atomic layer deposition (c-ald) using self-limiting reactions at nanocrystal surface coupled to phase transfer between polar and nonpolar media. *Journal of the American Chemical Society*, 134(45):18585–18590, 2012.

[41] C.A. Leatherdale, C.R. Kagan, N.Y. Morgan, S.A. Empedocles, M.A. Kastner, and M.G. Bawendi. Photoconductivity in CdSe quantum dot solids. *Physical Review B*, 62(4):2669, 2000.

[42] N.Y. Morgan, C.A. Leatherdale, M. Drndic, M.V. Jarosz, M.A. Kastner, and M. Bawendi. Electronic transport in films of colloidal CdSe nanocrystals. *Physical Review B*, 66(7):075339, 2002.

# Chapter 4

# Red, green, and blue colloidal quantum dot distributed feedback laser

## 4.1 Motivation and rationale

Following in the footsteps of fundamental studies of quantum confinement effect in low dimensional semiconductors [1**?** , 2], CQDs in the visible have become an appealing candidate for the next generation of luminescent materials for displays whether as advanced phosphors [**?** **?** ] or LEDs [13**?** **?** –15] and lasers [17**?** **?** , 18]. The chemically synthesized colloidal quantum dots are solution-processed semiconductor nanocrystal materials and their fabrication process into e.g. an RGB phosphor is fairly simple. State-of-the-art CQDs exhibit small size dispersion (less than 5%), high crystalline structure quality and effective surface passivation [**?** ] so that their photoluminescence quantum yield can reach almost up to unity with high color purity.

Given such assets of CQDs, research has also focused on the possibility of their

use as lasers. Two factors, one fundamental and the other practical have presented obstacles. On fundamental side, and despite their favorable light-emitting properties, CQDs suffer from non-radiative multiexcitonic Auger recombination process in achieving optical amplification or lasing. The efficiency of the Auger process is greatly enhanced in the quantum dots so that the inelastic electron-electron scattering can be much stronger than the electron-photon coupling [24]. Consequently, ultra-short pulsed (sub-pico-second) optical excitation sources have been employed to obtain optical amplification, circumventing the non-radiative decay channel [17, 27]. In order to suppress the Auger recombination, various types of quantum dot structures have been investigated including type II heterostructure core-shell CQDs [27] and quantum rods structures [29]. By first engineering specific type-I CQDs and then assembling them in very densely packed thin films, we have shown how access becomes possible to a single-exciton gain regime whereby both Auger effects and optical pumping thresholds for stimulated emissionare greatly reduced [17].

In this chapter, we focus on creating practical laser device structures in RGB colors without changing material composition by embedding the CQD optical gain media within DFB resonator structures. We demonstrate RGB surface-emitting second-order DFB lasers [18**? ? ? ?** ] which exhibit single cavity mode operation with well-defined spatially coherent output beams, and good efficiency. In the optical pumping experiments a compact solid-state laser was used as the excitation source, with pulse-widths exceeding the Auger decay time, and in contrast with much of the ultrashort pulse laser work in the literature.

## 4.2 Dense CQD film and optical characterization

The type I CdSe/$Zn_{0.5}Cd_{0.5}S$ core/shell CQDs used in this study were fabricated by high-temperature organometallic synthesis [6]. The diameters of CdSe core varied

between 2.5 $\sim$ 4.2 nm to tune the principal excitonic absorption and emission resonance wavelengths across the visible, from which gain and lasing was to be extracted. As part of the construct a 1 nm-thick ternary shell was grown to reduce strain and create a proper core/shell band gap difference for confinement of the electrons and holes. The cadmium composition in the ternary shell gives maximum alloy potential fluctuations, which may help in spatial localization of exciton wave function as shown in bulk single II-VI crystals [**?** ]. Finally, monolayer scale hydrophobic aromatic ligands were added for surface passivation. These engineered type-I CQDs were realized at extremely high concentrations ($\sim$ 150 mg/ml) in Toluene, without aggregation and were able to reach an approximately 80% photoluminescence-measured quantum yield. Such concentrated solutions were then spin-cast on quartz substrates to form self-assembled, densely packed solid thin films [17]. The films were 200 - 300 nm in thickness with an effective refractive index between n $\approx$ 1.65 - 1.8 across the RGB samples determined by ellisometry. Calculating from the refractive indices for the bulk materials, and without accounting for the organic ligand, we obtained for the packing density of the films about a value of $\sim$ 50% which is remarkably high when compared to the maximum case of identical hard spheres ($\sim$ 74%). Very important, the surface of the RGB films were optically smooth, indicating surface flatness of $\lambda/30$ and root-mean-square (RMS) surface roughness of 2 nm.

Figure 4.1 represents the absorption and emission spectra of the RGB CQD films, respectively, at room temperature. The red and green CQD films show very well-defined, spectrally isolated lowest exciton absorption peaks (up to $n = 3$ for red CQD), whereas these features are weak in the blue CQD films. In all cases, the emission peaks are red-shifted from their lowest exciton absorption peaks (Stokes shift). Importantly, the magnitude of the Stokes shifts in RGB CQD films are quite comparable to the half of the full-width-half-maximum (FWHM) of their spontaneous emission. We have found empirically that this approximate relationship is

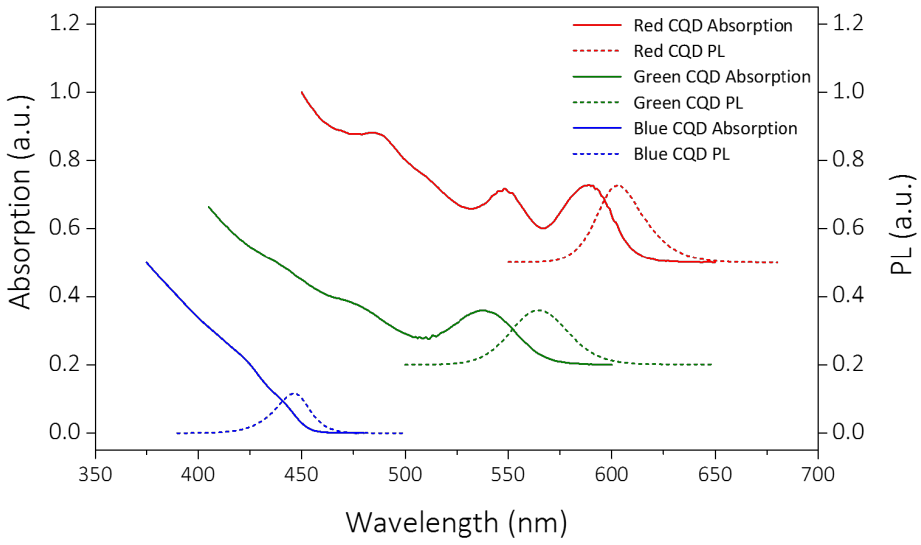


**Figure 4.1:** Absorption and photoluminescence spectra from densely packed solid red, green and blue CQD films at room temperature. (reprinted from [19])

optimal for achieving stimulated emission from the corresponding exciton resonance while reducing the self-absorption of emitted photons by the CQD films.

## 4.3 Design of grating structures and DFB laser microfabrication processes

### 4.3.1 Introduction to Bragg grating

To make laser devices from optical gain materials, suitable resonator structures should be involved. There exist various resonator structures such as Fabry-Perot, DFB, DBR, whispering-gallery mode, etc. Among the possible resonator structures, the DFB configuration can offer better mode controls in both longitudinal and transverse directions with relatively easy fabrication processes in the case of the solution-processed densely-packed CQD films.

In the DFB structure, selection of wavelength, a single mode of radiation can be achieved by distributed Bragg scattering. Under phase matching conditions, the emitted photons from the CQDs are coherently reflected from the periodic grating structure. The partially reflected waves from the corrugated structure give rise to constructive interference at a phase-matched wavelength, which is called Bragg wavelength. The Bragg wavelength is governed by the following equation:

$$\lambda_B = \frac{2\Lambda n_{eff}}{m} \ , \tag{4.1}$$

where $\lambda_B$ is the Bragg wavelength, $\Lambda$ is the pitch of the grating, $n_{eff}$is the refractive index of the grating layer, and $m = 1, 2, \cdots$ is the diffraction order. Thus, by controlling the pitch of the grating and the effective refractive index (varying the thickness of CQD films), narrow bandwidth and tunable emission of Bragg wavelength can be obtained.

| **Diffraction order** | **m = 0** | **m = 1** | **m = 2** |
|---|---|---|---|
| $1^{st}$-order grating | Feed-forward | Feedback | - |
| $2^{nd}$-order grating | Feed-forward | Radiation at $\theta_d \sim 0^\circ$ | Feedback |

**Table 4.1:** Summary of feedback and radiation loss from the DFB gratings. $\theta_d$ is a diffraction angle.[**?** ]

Here, the second-order grating, where $m = 2$, is of particular interest because the coupled light through the grating provides perpendicular lasing outputs from the surface of the grating. Thus, surface-emitting lasers can be achieved by using this second-order DFB grating. The relationship between the grating orders and diffraction orders is summarized in the table 4.1[**?** ]. For $1^{st}$-order gratings, the optical feedback is provided through the first diffraction order to form an edge-emitted laser. However, in $2^{nd}$-order gratings, the corrugated grating structure provides for in-plane distributed feedback and perpendicular output coupling from the grating plane via second- and first-order diffractions, respectively. According to equation 4.1, the pitch of the grating for $2^{nd}$-order DFB lasers can have larger dimensions compared to $1^{st}$-order ones, which leads to easier fabrication processes. In addition, vertically emitted photons are also easier to capture the lasing outputs than edge-emitted photons in the $1^{st}$-order DFBs. Thus, $2^{nd}$-order DFB configuration using quartz substrates as a grating structure has been chosen for these reasons to produce the surface-emitting RGB CQD lasers in this study. Considering the measured refractive indices and the wavelength at the ASE peaks of the RGB CQD films, the pitches of the gratings were expected to be 360 ± 10 nm (red), 330 ± 10 nm (green), and 260 ± 10 nm (blue) according to the Bragg relation. Detailed fabrication processes, experimental data and discussion will be followed in the next sections.

### 4.3.2 Holographic interference lithography for red DFB laser

Holographic interference lithography is a useful way to pattern periodic structures such as gratings. For red emitting CQD DFB lasers, considering the wavelength of the PL and the refractive index of the CQD films, the pitch of the grating needs to be around 350 nm. Therefore, A He-Cd laser emitting wavelength of 325 nm with long coherence length (∼30 cm) was used as an optical source for this lithography process as described in Fig. 4.2. The He-Cd laser beam was spatially filtered and

formed an incident plane wave. The mirror was mounted on a rotating stage for adjustment of the incident angle to vary the periodicity of the patterns.

A thin film (5 nm) of chromium, acting as a hard mask for the subsequent etching process, was deposited on the quartz substrate after development of the exposed photoresist layer [**?** **?** ]. Then, the grooves were formed by inductively-coupled-plasma reactive-ion-etching (ICP-RIE). The pressure inside of the chamber of the ICP-RIE equipment was kept at 2m Torr. Argon and octafluorocyclobutane ($C_4F_8$) gases were used with a flow rate of 15 sccm for both. The platen and coil powers were maintained at 400 and 150 W, respectively. These etching parameters yielded approximately 135 nm/min of etch rate. Finally, 75 nm-deep grooves were accomplished with 35 sec of etching process time. Figure 4.3 shows the SEM image of the final grating structure for the red CQD DFB devices.

### 4.3.3 Focused ion beam milling for green DFB laser

Focused ion beam (FIB) milling is another technique to pattern down to sub-micron scales. It usually uses a focused beam of gallium (Ga) ions to raster the surface of a sample similarly to the SEM which uses a beam of electrons. In the FIB systems, when the beam of Ga ions are focused to hit the sample, it leaves the surface of the sample with secondary electrons, ions, and sputtered atoms [**?** ]. At low operating beam currents, the secondary electrons can be collected for imaging purpose with 5 nm resolution which is limited by the sputtering and detector efficiency [**?** **?** ].

To fabricate CQD DFB lasers emitting in green color, the pitch of the grating needs to be around 330 nm, given the refractive index of the CQD films ($\sim 1.7$) and the ASE peak ($\sim$580 nm) for the green CQD materials. However, this criterion for the pitch of the grating limits the application of holographic interference lithography technique using a Hd-Cd laser. Therefore, FIB technique was used to pattern the grating structures for the green CQD DFB lasers in this study.

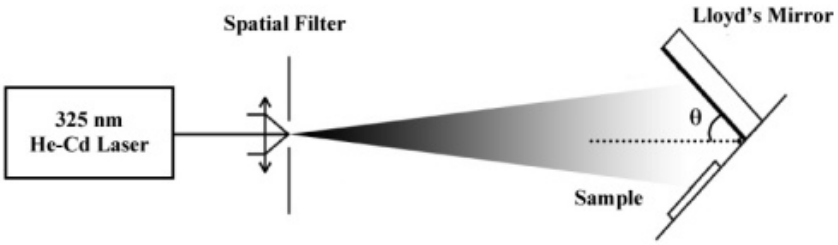


**Figure 4.2:** Schematic illustration of the optical setup for the interference lithography. (reprinted from [**?** ])

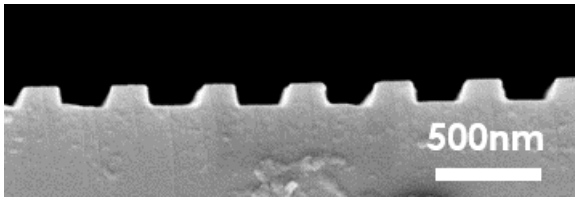


**Figure 4.3:** Cross-sectional SEM image of a quartz grating. (reprinted from [18])

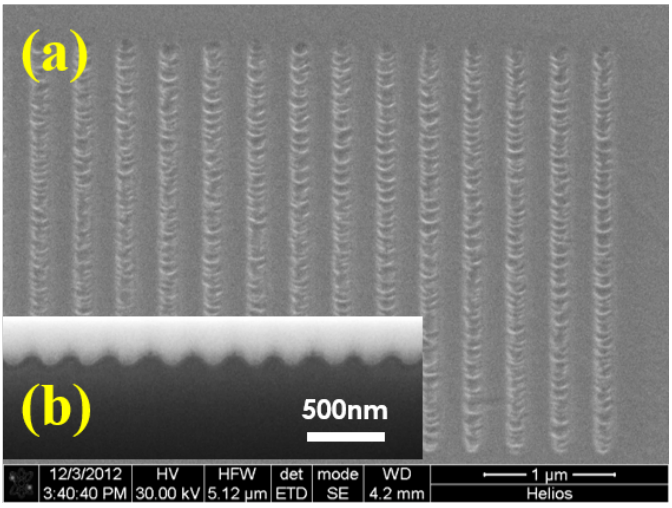


**Figure 4.4:** SEM image of the grating for the green DFB lasers. Top view (a) and cross-sectional view (b). (reprinted from [19])

10 nm-thick Cr layer was deposited by electron-beam evaporation on a quartz substrate. The ion beam current was maintained at 460 pA, and the dose amount on the Cr film was set to be 25 mC/cm$^2$. With these milling parameters, 900 periodic 100 $\mu$m-long lines were patterned as seen in Fig. 4.4. Note that this milling technique using focused Ga-ion beams directly etches away the quartz substrate, leading to no further ICP etching process.

### 4.3.4 Electron-beam lithography for blue DFB laser

Due to the practical limitation in resolution of the holographic interference lithography and milling time of the FIB system, electron-beam lithography technique was used to acquire smaller grating patterns for blue CQD DFB lasers which require approximately 250 nm-long periodicity.

The fabrication procedures are illustrated in Figs. 4.5 (a-e). 170 nm-thick layer of Poly(methyl methacrylate) (PMMA) was spin-coated on quartz, then soft-baked at 180 °C for 180 sec. Then, as a charge-dissipation layer for the electron beams, a thin Cr film (less than 10 nm) was evaporated above the PMMA layer. Under 30 kV of acceleration voltage, the electron beam current and dose amount were set to be 1.9 nA and 250 $\mu$C/cm$^2$. 1000 periodic 250 $\mu$m-long lines have been written on the PMMA while varying the pitches of the grating from 230 to 280 nm. The PMMA resist was developed after removing the Cr film by wet etching process. A 30 nm-thick Cr layer was deposited on the patterned PMMA. Lift-off process of the PMMA in acetone resulted in a periodic Cr hard-mask pattern. Finally, a grating pattern with groove depth of 75 nm was formed by ICP-RIE process using the same etching conditions for the red DFB gratings. Figures 4.5 (h) is the cross-sectional view of SEM image for the bare grating. Then blue CQD films were spin-coated on top of this grating structure with optically smooth surface filling the entire grooves as seen in Fig. 4.5 (i).

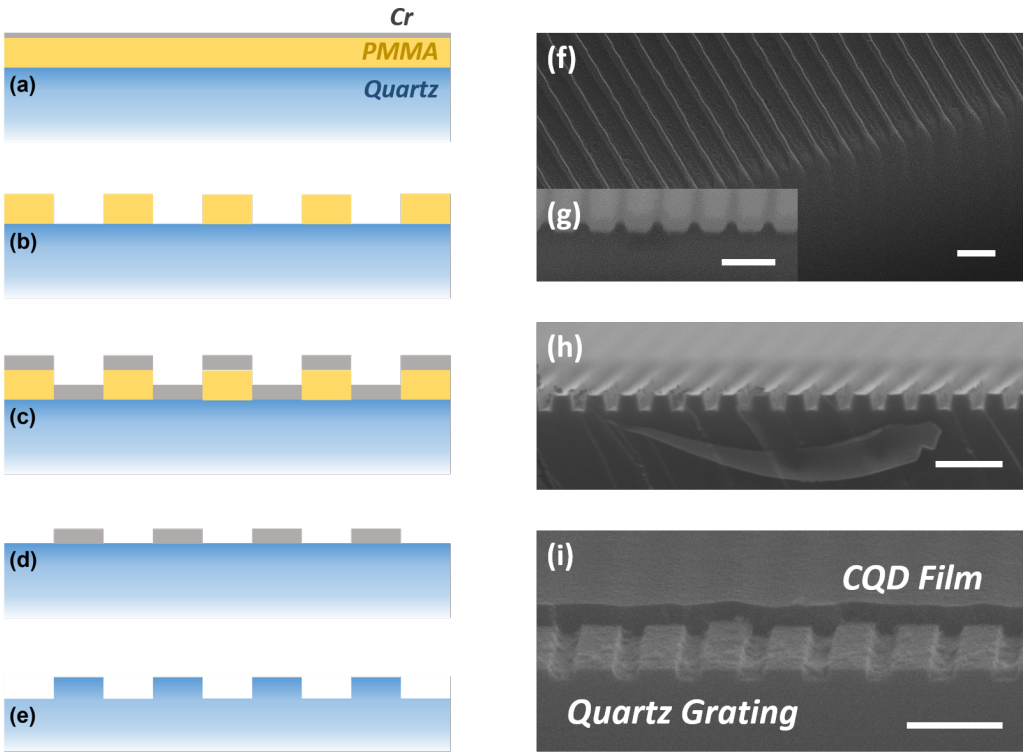


**Figure 4.5:** Fabrication procedure for the blue CQD DFB lasers (a)-(e). Gray, yellow, and light-blue colors represent Cr, PMMA, and Quartz, respectively. Reference SEM image of the cross-sectional view of the red DFB gratings fabricated by holographic lithography (f)-(g). SEM images of the bare blue DFB grating by electron-beam lithography (h) and with densely-packed CQD films (i). Scale bars are 500 nm. (reprinted from [19])

## 4.4 Lasing action under sub-nanosecond-pulsed optical pumping

### 4.4.1 Experimental setup

A compact solid state laser (pulse duration of 400 ps; repetition rate of 1 kHz) at 532 nm (for red) and 355 nm (for green and blue) of second- and third-harmonics from a Nd:Yag source was used to optically pump the CQD DFB lasers. Figure 4.6 and table 4.2 are the photographic image and the specifications of the pumping laser. We underscore that the pump pulses were thus longer than the typical non-radiative Auger decay time constants of $\sim$ 100 ps for biexciton and multiexciton processes which have dominated the literature on optical gain experiments in II-VI CQDs that use ultrashort pulsed excitation [24, 27].

The experimental setup for the RGB CQD DFB lasers is illustrated in Fig. 4.7. The fundamental output wavelength from the pumping laser was frequency-doubled and -tripled to generate second- and third-harmonics (532 and 355 nm) by using a non-linear lithium triborate (LBO) crystal. The excitation intensities were varied by a compensated reflective neutral density filter. The pumping beam was focused by a cylindrical lens to form an approximately 20 $\mu$m-wide stripe excitation onto the CQD films. The emitted signals from the CQD DFB devices were collected by an objective lens and analyzed by a spectrometer (Model:INS-300-122B, Acton Research Corporation). The electronic shutter was installed and synchronized with the spectrometer to minimize the exposure time by the excitation beam. We varied the pitch of the gratings to tune the output emission wavelength of the CQD DFB lasers with a fixed groove depth of 75 nm. These parameters were chosen for being close to optimizing a low lasing threshold as indicated in our previous results with red CQDs [18].

**Figure 4.6:** Photograph image of the laser - Model: PNP-M0810, Vendor: teem photonics ™

| **Pumping Laser** | **PNP-M0810** |
|---|---|
| Peak Power (kW) | 220 |
| Average Power (mW) | 90 |
| Repetition Rate (kHz) | 1 |
| Pulse Width (ps) | 400 |
| Energy/Pulse (µJ) | 90 |

**Table 4.2:** Specification of the optical parameters for the pumping laser used in the RGB DFB laser demonstration.

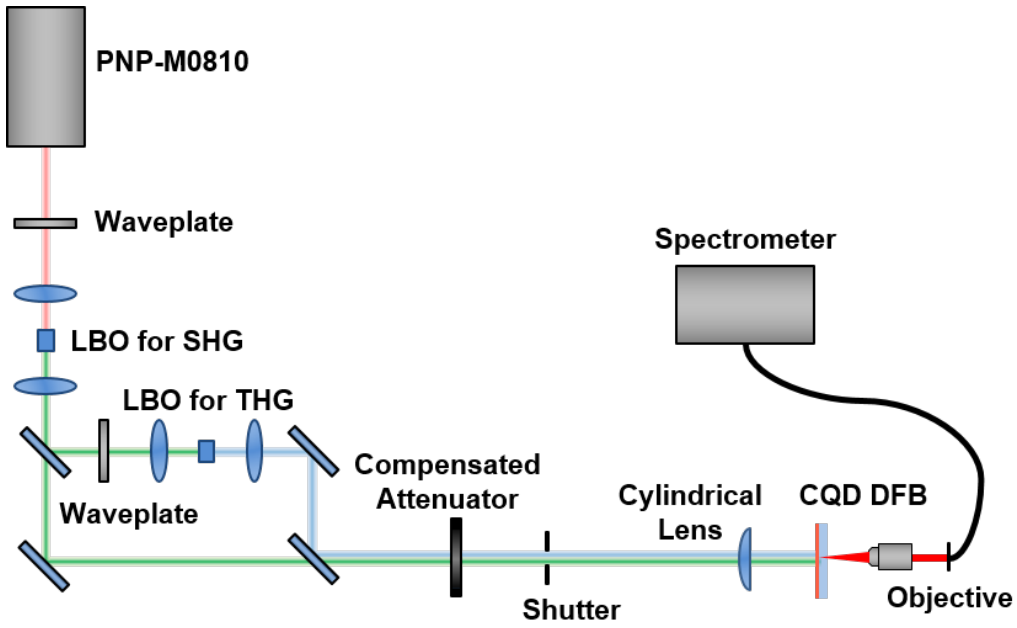


**Figure 4.7:** Schematic diagram of the experimental setup for RGB CQD DFB lasers. The second harmonic generation (SHG) setup has been used to excite the red DFB lasers, and the third harmonic generation (THG) setup has been used for the green and blue DFB lasers.

### 4.4.2 Results

A summary of the RGB emission in terms of spectral characteristics is shown in Fig. 4.9 (a). At low pumping level, the devices emitted typical Gaussian-shaped photoluminescence signals. At a well-defined threshold for each color, the onset of stimulated emission was unambiguous from the linewidth narrowing. Figure 4.9 (a) also includes the edge emitted ASE spectra from corresponding planar films which we used to optimize the DFB laser operation by tuning the dominant grating mode into spectral coincidence from varying the effective index of refraction of the CQD films. Specifically, to match the DFB lasing with the ASE emission, we prepared a series of samples where the thickness of the CQD films ranged between 150 nm and 300 nm to fine-tune the effective refractive indices of the CQD films on the corrugated grating structures. Figure 4.8 shows the effect of varying the thickness of the CQD films. By varying the thickness of CQD films, we were able to observe spectral shifts of the lasing peaks, further verifying the dominance of DFB-induced optical feedback through the CQD gain media.

The lasing outputs exhibited a very narrow linewidth (FWHM $<$ 1 nm, below the limit of our spectrometer resolution), indicating an evident single-mode operation. Figures 4.9 (b-d) shows the output intensities from the RGB CQD DFB lasers as a function of input energy density per pump pulse, showing evident threshold behaviors. The micrographs in the insets visually show a significant increase in the output intensity of the stripe when the pumping level is above the threshold for all three colors. The threshold pumping energy densities were measured as 120, 280, and 330 $\mu$J/cm$^2$ for the red, green, and blue CQD DFB lasers, respectively.

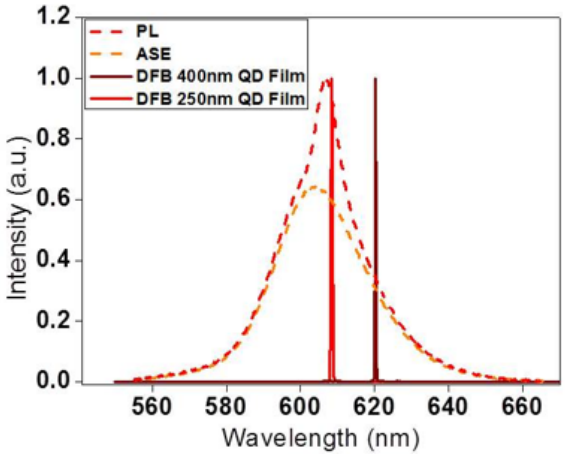


**Figure 4.8:** Spectral analysis of the PL and ASE from a CQD film on quartz substrate and single mode red CQD DFB lasers in which a single quartz grating was spin-coated with two different CQD film thicknesses. (reprinted from [18])

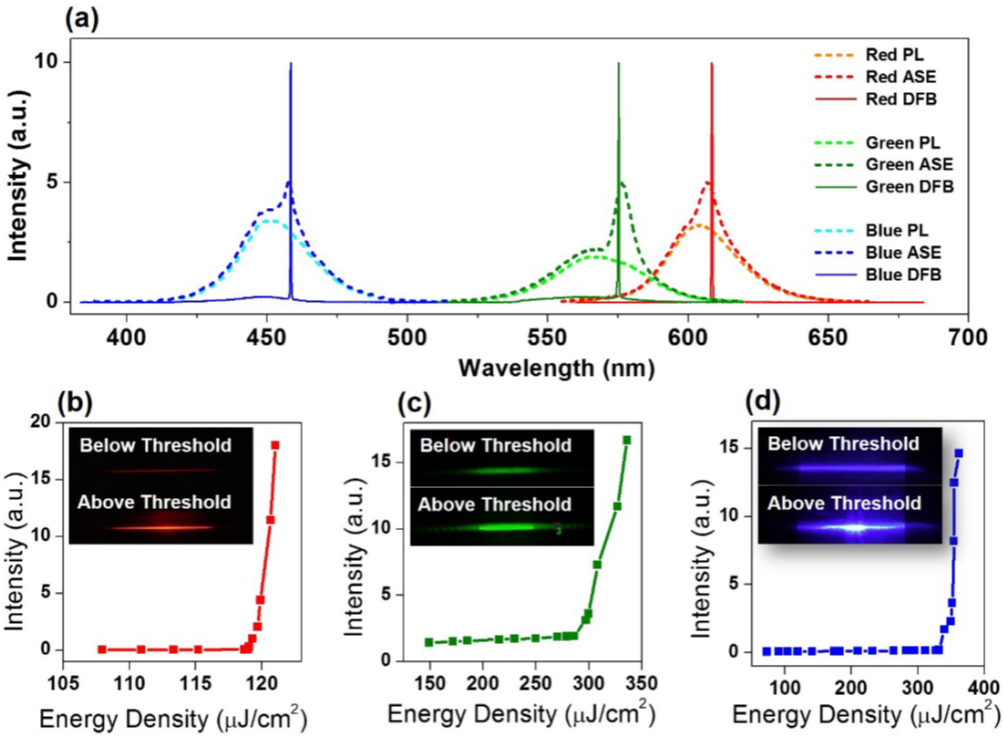


**Figure 4.9:** (a) Spectral characteristics of the RGB CQD DFB lasers. Solid lines represent the single mode output laser beams perpendicular to the device surface just above the lasing threshold. (b-d) Input-Output characteristics of the three lasers highlighting the threshold regime. Insets show the near-field patterns, underscoring the spatial coherence in the laser emission. (reprinted from [19])

## 4.5 Far-field emission and spatially coherent lasing outputs

It is very important to validate the DFB laser operation by also measuring the spatial coherence of the emitted radiation as well-defined output beams. Far-field patterns from our devices are seen in Fig. 4.10. The patterns were vertically elongated due to the stripe geometry (200 $\mu$m-length and 20 $\mu$m-width) by the focusing cylindrical lens. They exhibited two closely spaced beams, instead of single beam. This well-known phenomenon occurs due to the interference between coherent left-and right-traveling waves in any finite length optical waveguide [**?** ], i.e. here along the gain guided excitation stripe in the CQD films. As a result, there was always a zero intensity at the center of the stripe in the near-field which, in turn, Fourier-transforms in the far-field to a double-lobed pattern. In DFB applications requiring Gaussian fundamental transverse modes, a symmetric mode operation with single lobe can be obtained by introducing half-wave phase shift in grating structure [**?** ] or incorporating a photonic crystal structure. Note that the angular divergence in the horizontal direction is less than 2°, which is consistent with high degree of spatial coherence.

The measured average output powers of the RGB lasers are listed in Table 4.3. The maximum output power from the red DFB laser was about 400 $\mu$W. We note that the device emitted perpendicular output beams emerging from the surface in both opposite directions. Therefore the conversion efficiency (output power vs. absorbed power) was about 28% when considering that only 25% of the incident light was absorbed by the CQD film. Similarly, the maximum measured output power for the green and blue DFB were 40 and 5 $\mu$W, respectively. Since the pumping power of our third-harmonic source (355 nm) only reached 0.9 mW, the absolute output power values of the green and blue DFB lasers were not as high as that of the red

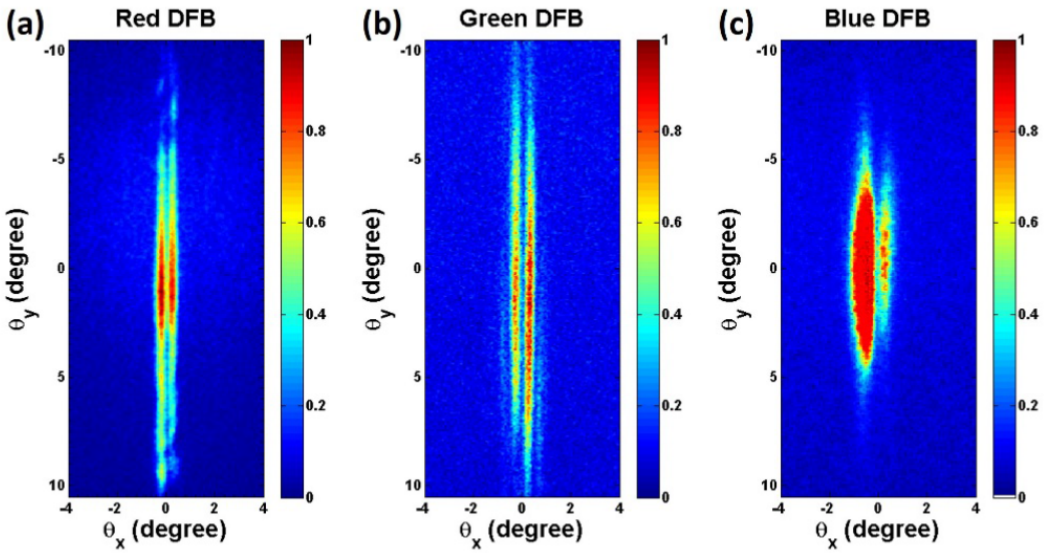


**Figure 4.10:** Far-field patterns of the output beams for red (a), green (b), and blue (c) CQD DFB devices. (reprinted from [19])

| **DFB lasers** | **Excitation wavelength** [nm] | **Absorbance** | **Pumping power** [mW] | **Output power** [µW] | **Efficiency** [%] |
|---|---|---|---|---|---|
| Red | 532 | 0.13 | 6 | 400 | 28 |
| Green | 355 | 0.5 | 0.9 | 40 | 6 |
| Blue | 355 | 0.05 | 0.9 | 5 | 7 |

**Table 4.3:** Output characteristics of the RGB CQD DFB lasers (reprinted from [19]).

DFB laser. Their conversion efficiencies, however were nonetheless at a satisfactory high level.

## 4.6 Conclusions

We have developed surface-emitting colloidal QD DFB optically pumped lasers which operate across the red, green and blue colors based on a single material system. The device structures employed closely-packed QD films deposited on grating structures which were optimized to yield maximum performance. Highly monochromatic lasing for all three colors was achieved at low excitation thresholds and measured far-field profiles demonstrated high degree of spatial coherence in the output beams of our DFB lasers. By taking advantage of single-exciton optical gain from our engineered type-I CdSe/ZnCdS core/shell thin films, the RGB DFB lasers were optically pumped beyond the normal Auger regime into quasi-steady state operation with high conversion efficiency. To reach continuous wave operation will require strategies for heat management which were not applied here.

# Bibliography

[1] Y. Arakawa and H. Sakaki. Multidimensional quantum well laser and temperature dependence of its threshold current. *Applied Physics Letters*, 40(11):939–941, 1982.

[2] L.E. Brus. A simple model for the ionization potential, electron affinity, and aqueous redox potentials of small semiconductor crystallites. *The Journal of Chemical Physics*, 79(11):5566–5571, 1983.

[3] A.I. Ekimov and A.A. Onushchenko. Quantum size effect in three-dimensional microscopic semiconductor crystals. *ZhETF Pisma Redaktsiiu*, 34:363, 1981.

[4] J.S. Steckel, J. Ho, C. Hamilton, C. Breen, W. Liu, P. Allen, J. Xi, and S. Coe-Sullivan. Quantum dots: the ultimate down-conversion material for lcd displays. In *SID Symp. Dig. Tech. Pap.(submitted)*, 2014.

[5] Jonathan S Steckel and Seth Coe-Sullivan. Quantum dots for display backlighting. In *Abstracts of Papers of the American Chemical Society*, volume 246. American Chemical Society.

[6] K.S. Cho, E.K. Lee, W.J. Joo, E.J. Jang, T.H. Kim, S.J. Lee, S.J. Kwon, J.Y. Han, B.K. Kim, B.L. Choi, and J.M. Kim. High-performance crosslinked colloidal quantum-dot light-emitting diodes. *Nature Photonics*, 3(6):341–345, 2009.

[7] C. Dang, J. Lee, Y. Zhang, J. Han, C. Breen, J.S. Steckel, S. Coe-Sullivan, and A.V. Nurmikko. A wafer-level integrated white-light-emitting diode incorporating colloidal quantum dots as a nanocomposite luminescent material. *Advanced Materials*, 24(44):5915–5918, 2012.

[8] B.S. Mashford, M. Stevenson, Z. Popovic, C. Hamilton, Z. Zhou, C. Breen, J. Steckel, V. Bulovic, M. Bawendi, S. Coe-Sullivan, and P.T. Kazlas. High-efficiency quantum-dot light-emitting devices with enhanced charge injection. *Nature Photonics*, 7(5):407–412, 2013.

[9] J. Kwak, W.K. Bae, D. Lee, I. Park, J. Lim, M. Park, H. Cho, H. Woo, D.Y. Yoon, and K. Char. Bright and efficient full-color colloidal quantum dot light-emitting diodes using an inverted device structure. *Nano Letters*, 12(5):2362–2366, 2012.

[10] J.M. Caruge, J.E. Halpert, V. Wood, V. Bulović, and M.G. Bawendi. Colloidal quantum-dot light-emitting diodes with metal-oxide charge transport layers. *Nature Photonics*, 2(4):247–250, 2008.

[11] C. Dang, J. Lee, C. Breen, J.S. Steckel, S. Coe-Sullivan, and A.V. Nurmikko. Red, green and blue lasing enabled by single-exciton gain in colloidal quantum dot films. *Nature Nanotechnology*, 7(5):335–339, 2012.

[12] C. Dang, J. Lee, K. Roh, H. Kim, S. Ahn, H. Jeon, C. Breen, J.S. Steckel, S. Coe-Sullivan, and A.V. Nurmikko. Highly efficient, spatially coherent distributed feedback lasers from dense colloidal quantum dot films. *Applied Physics Letters*, 103(17):171104, 2013.

[13] F. Todescato, I. Fortunati, S. Gardin, E. Garbin, E. Collini, R. Bozio, J.J. Jasieniak, G. Della Giustina, G. Brusatin, S. Toffanin, and R. Signorini. Soft-lithographed up-converted distributed feedback visible lasers based on CdSe–CdZnS–ZnS quantum dots. *Advanced Functional Materials*, 22(2):337–344, 2012.

[14] V.C. Sundar, H.J. Eisler, T. Deng, Y. Chan, E.L. Thomas, and M.G. Bawendi. Soft-lithographically embossed, multilayered distributed-feedback nanocrystal lasers. *Advanced Materials*, 16(23-24):2137–2141, 2004.

[15] C.B. Murray, D.J. Norris, and M.G. Bawendi. Synthesis and characterization of nearly monodisperse cde (e= sulfur, selenium, tellurium) semiconductor nanocrystallites. *Journal of the American Chemical Society*, 115(19):8706–8715, 1993.

[16] V.I. Klimov, A.A. Mikhailovsky, D.W. McBranch, C.A. Leatherdale, and M.G. Bawendi. Quantization of multiparticle auger rates in semiconductor quantum dots. *Science*, 287(5455):1011–1013, 2000.

[17] V.I. Klimov, S.A. Ivanov, J. Nanda, M. Achermann, I. Bezel, J.A. McGuire, and A. Piryatinski. Single-exciton optical gain in semiconductor nanocrystals. *Nature*, 447(7143):441–446, 2007.

[18] M. Zavelani-Rossi, M.G. Lupo, R. Krahne, L. Manna, and G. Lanzani. Lasing in self-assembled microcavities of CdSe/CdS core/shell colloidal quantum rods. *Nanoscale*, 2(6):931–935, 2010.

[19] Y. Chen, B. Guilhabert, J. Herrnsdorf, Y. Zhang, A.R. Mackintosh, R.A. Pethrick, E. Gu, N. Laurand, and M.D. Dawson. Flexible distributed-feedback colloidal quantum dot laser. *Applied Physics Letters*, 99(24):241103, 2011.

[20] S. Gao, C. Zhang, Y. Liu, H. Su, L. Wei, T. Huang, N. Dellas, S. Shang, S.E. Mohney, and J. Wang. Lasing from colloidal inp/zns quantum dots. *Optics Express*, 19(6):5528–5535, 2011.

[21] M.A. Hines and P. Guyot-Sionnest. Synthesis and characterization of strongly luminescing ZnS-capped CdSe nanocrystals. *The Journal of Physical Chemistry*, 100(2):468–471, 1996.

[22] O. Goede, L. John, and D. Hennig. Compositional disorder-induced broadening for free excitons in ii-vi semiconducting mixed crystals. *Physica Status Solidi (b)*, 89(2):K183–K186, 1978.

[23] K. Roh, C. Dang, J. Lee, S. Chen, J.S. Steckel, S. Coe-Sullivan, and A.V. Nurmikko. Surface-emitting red, green, and blue colloidal quantum dot distributed feedback lasers. *Optics Express*, 22(15):18800–18806, 2014.

[24] J.E. Carroll, J. Whiteaway, and D. Plumb. *Distributed feedback semiconductor lasers*, volume 10. IET, 1998.

[25] C.H. Liu, M.H. Hong, H.W. Cheung, F. Zhang, Z.Q. Huang, L.S. Tan, and T.S.A. Hor. Bimetallic structure fabricated by laser interference lithography for tuning surface plasmon resonance. *Optics Express*, 16(14):10701–10709, 2008.

[26] J. Lee, S. Ahn, S. Kim, D. Kim, H. Jeon, S. Lee, and J. Baek. Gan light-emitting diode with monolithically integrated photonic crystals and angled sidewall deflectors for efficient surface emission. *Applied Physics Letters*, 94(10):101105, 2009.

[27] J. Lee, S. Ahn, H. Chang, J. Kim, Y. Park, and H. Jeon. Polarization-dependent gan surface grating reflector for short wavelength applications. *Optics Express*, 17(25):22535–22542, 2009.

[28] A. Latif, W.E. Booij, J.H. Durrell, and M.G. Blamire. Real time resistometric depth monitoring in the focused ion beam. *Journal of Vacuum Science & Technology B*, 18(2):761–764, 2000.

[29] J. Orloff, L.W. Swanson, and M. Utlaut. Fundamental limits to imaging resolution for focused ion beams. *Journal of Vacuum Science & Technology B*, 14(6):3759–3763, 1996.

[30] V. Castaldo, C.W. Hagen, B. Rieger, and P. Kruit. Sputtering limits versus signal-to-noise limits in the observation of sn balls in a ga+ microscope. *Journal of Vacuum Science & Technology B*, 26(6):2107–2115, 2008.

[31] H. Kogelnik and C.V. Shank. Coupled-wave theory of distributed feedback lasers. *Journal of Applied Physics*, 43(5):2327–2335, 1972.

[32] G. Witjaksono, S. Li, J.J. Lee, D. Botez, and W.K. Chan. Single-lobe, surface-normal beam surface emission from second-order distributed feedback lasers with half-wave grating phase shift. *Applied Physics Letters*, 83(26):5365–5367, 2003.

# Chapter 5

# Colloidal Quantum Dot Vertical-cavity Surface-emitting Laser

## 5.1 Motivation and Rationale

After nanocrystal quantum dots were predicted theoretically as efficient fluorescent materials, their optical gain properties have been reported by many researchers [**?** **?** **?** **?** ]. However, having optical gains does not always guarantee the stimulated emission in quantum dots. The stimulated emission can only be achieved when the buildup time of the population inversion is faster than the time of their relaxation to the ground state. Here, the buildup time for the stimulated emission $\tau_s$, can be expressed in terms of a gain cross section, $\sigma_g$ and the volume fraction of semiconductor material in the sample, $\xi$ as follows [**?** ]:

$$\tau_s = \frac{n_r}{Gc} = \frac{4\pi R^3}{3}\frac{n_r}{\xi\sigma_g c} \ , \tag{5.1}$$

where $c$ is the velocity of light, $n_r$ is the sample refractive index, and $R$ is a radius of quantum dots. Assuming that the gain decay process is dominated by the Auger recombination ($\tau_{Auger}$), stimulated emission can be observed if $\tau_s$ is less than $\tau_{Auger}$. Eqaution 5.1 shows that the volume fraction of the quantum dots should be high enough. In earlier chapter, we have shown that our CQD solutions can meet the condition by spin-coating the CQDs of ultrahigh concentration ($\sim$ 100 mg/ml), which produces close-packed dense solid films as in Fig. 3.1(c). Also, for the light amplification, the excitation source needs to be short enough (sub-picosecond) to bypass the fast-decaying Auger process.

However, we have already shown that the precisely optimized Stokes shift and narrow inhomogeneous broadening of the photoluminescence can bring the CQDs in the single exciton gain regime to effectively circumvent the fatal Auger process. As a result, a sub-nanosecond pulsed optical excitation generated highly efficient and spatially coherent surface-emitting DFB lasers in the visible spectrum [12, 23]. Note that this result is in contrast with other reports such as whispering gallery mode lasing or random lasing mode in literature, where both have focused only on the monochromaticity, not on the spatial coherence nor the extraction of the lasing outputs.

VCSELs are another efficient laser structures extensively used in the display related applications, although they are one of the most challenging types of laser devices to be fabricated (high Q, low loss, and short optical path). Recently, a method of porosifying GaN by electro-chemical etching has been developed by Jung Han at Yale University [**?** **?** ]. Refractive index of NP-GaN layers can be easily tuned by this method. Alternating 10 pairs of NP-GaN and GaN layers, very high reflective (more than 99.5%) DBRs can be fabricated, which is suitable to be a basis of the VCSEL configuration [**?** ]. In the previous chapters, we have shown that the exciton decay mechanism is governed not by the multiexcitonic Auger process

but by the single exciton state, and demonstrated proof-of-concept CQD DFB lasers with high performance. Considering all the parameters to obtain lasing phenomenon by overcoming various obstacles as described above, the CQD VCSEL devices using NP-GaN/GaN DBRs with ultra-low lasing threshold can take a role as one of the efficient laser devices.

In this chapter, the fabrication process for the electro-chemical formation of NP GaN is briefly introduced. Then, optical characterization of the NPGaN/GaN DBRs is analyzed. The performance of the lasing output device in terms of longer pulsed optical excitation, thresholds and the lifetime are discussed in detail. Finally, pixelated two-dimensional arrays of CQD VCSEL are demonstrated via laser scanning micro-mirror system.

## 5.2 Chracterization of nano-porous GaN distributed Bragg reflector

The details of the electro-chemical etching processes for porosifying heavily doped n-type GaN ($n > 1 \times 10^{18}$ $cm^3$) are described in the other literature [**?** **?** **?** ]. During this procedure, oxalic acid was used as an electrolyte at room temperature. To have electrical contacts for voltage application, a GaN sample with an indium contact was connected to a platinum wire. Then, the bias voltage was applied to the GaN sample. The degree of etching can be tuned by simply changing the bias voltage (1 - 10 V) and the doping concentration of the n-type GaN materials as illustrated in Fig. 5.1 (a). According to this phase diagram of the electrochemical etching, the bias voltage and doping concentration can control not only the dimension of the pores (from mesoporous to macroporous), but also the level of etching (from no etching to electro-polishing) Hence, in order to have a proper level of porosified GaN media, the applied bias voltage and doping concentration need to be optimized as shown in

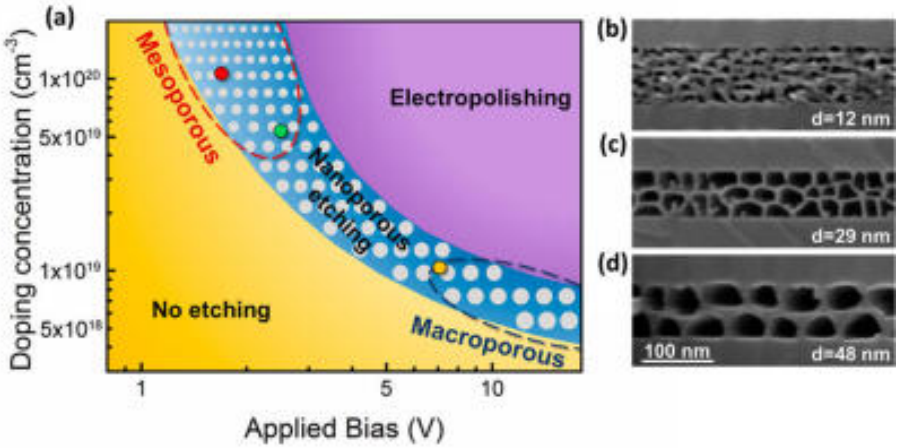


**Figure 5.1:** (a) Phase diagram for the electrochemical etching. The red and blue dashed lines represent the mesoporous and macroporous regions, respectively. SEM images of the etched NP-GaN according to the (b) red, (c) green, and (d) yellow conditions in (a). (reprinted from [**?** ])

Fig. 5.1 (b-d).

The NP-GaN/GaN DBRs used in this study are described in Fig. 5.2. A 1 $\mu$m-thick unintentionally doped (UID) GaN layer was grown on the top of the sapphire substrate. This process is required to ensure the recovery of good crystal quality from the very first stage of GaN nucleation layer growth on sapphire. Then, 0.5 $\mu$m-thick heavily doped n-type GaN ($5 \times 10^{18}$ cm$^{-3}$) layer was grown on the UID-GaN, acts as a current spreading layer making the electrical current spread uniformly across the whole sample during the electro-chemical etching process. On the top of this layer, another UID-GaN layer (0.5 $\mu$m) was located, directly beneath the DBR structure. This additional layer acts as an etch-stop layer to prevent the etching down to the sapphire substrate.

10 pairs of n$^+$GaN/GaN layers (1.63 $\mu$m) were grown epitaxially on the sapphire/UID-GaN/n-type GaN/UID-GaN structure. Trenches for opening windows were patterned on top of the DBR structure by photolithography and ICP RIE processes. Then, the electro-chemical etching was conducted in the lateral direction to lead porosification of n$^+$GaN layers selectively from the exposed sidewalls in the direction, perpendicular to the side wall to form the parallel nanopores [**?** ]. Figure 5.2 (b) is the normarski microscope image of the top surface of the fabricated NP-GaN/GaN DBR. Cross-sectional SEM images of the porosified NP-GaN/GaN DBRs can be seen in Fig. 5.2 (c) and (d), showing $\sim$ 70% of porosity and an average pore size of 30 nm.

The reflectance spectrum of the NP-GaN/GaN DBRs was measured by the experimental setup, which is shown in Fig. 5.3. The white laser output was created from a non-linear sapphire crystal via supercontinuum generation, and scanned by a monochromator from 500 to 720 nm. A beam splitter was used to split the laser beam into two parts. One of them was used for the calibration of the intensity over the scanned wavelength range, and the other was focused by a lens to form 50 $\mu$m

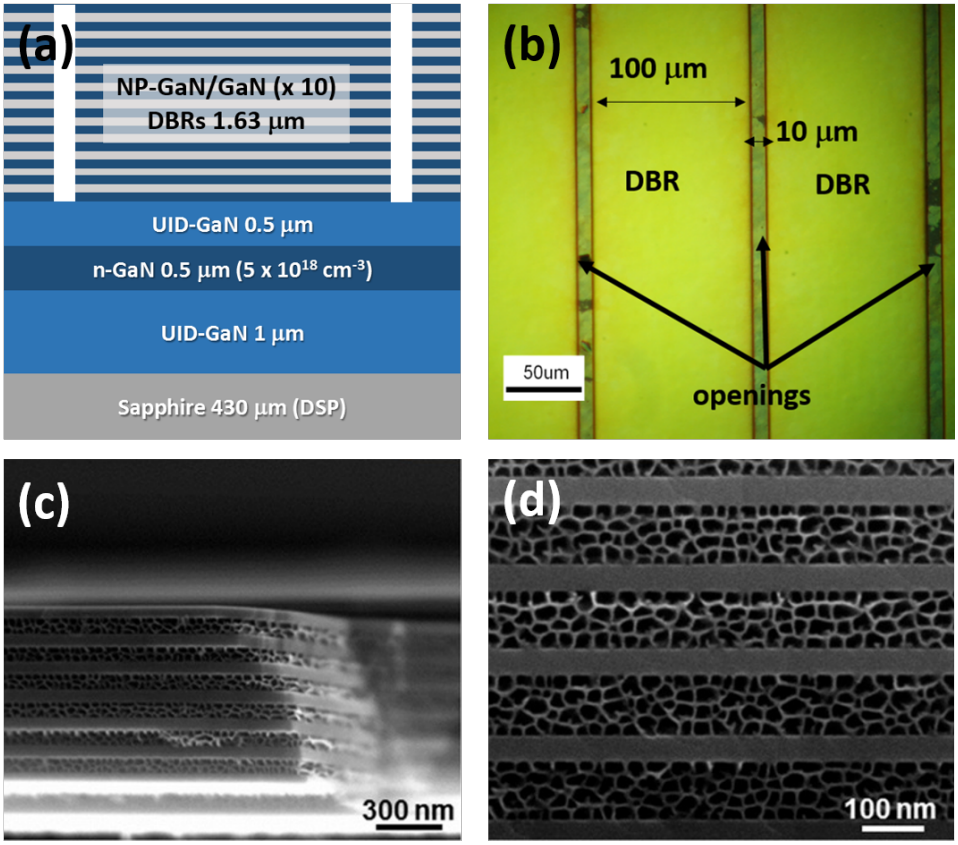


**Figure 5.2:** (a) Schematic diagram of NP-GaN/GaN DBR mirror. UID-GaN (1 $\mu$m)/n-type GaN (0.5 $\mu$m)/ UID-GaN (0.5 $\mu$m) layers were grown on the sapphire substrate. Epitaxial growth for the 10 pairs of $n^+$-GaN/GaN layers were followed. (b) Normarski microscope image showing 10 $\mu$m of opening windows and the highly reflective 100 $\mu$m-wide NP-GaN/GaN DBR region. (c) Cross-sectional SEM image of a NP-GaN/GaN DBR structure. (d) Zoom-in SEM image of the same structure. (reprinted from [**?** ])

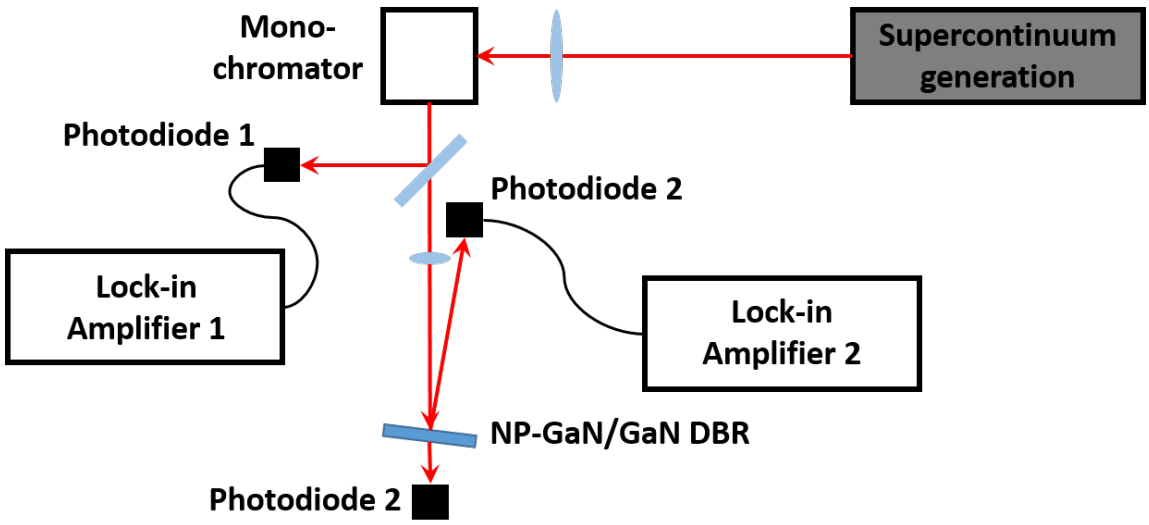


**Figure 5.3:** Experimental setup for the reflectance measurement. White laser outputs from the supercontinuum generation were scanned by a monochomator and focused into 50 $\mu$m circular spot on the DBR surface by a lens.

circular spot on the DBR surface. Two lock-in amplifiers were used to analyze the reflected signals from the surface of the DBRs. The reference signals were measured without the DBR sample. Then, the DBR sample was inserted into the setup with an incident angle of 7°. The reflected laser beam was collected by a photodetector (PDA100A, *Thorlabs, Inc.*).

The results of the reflectance measurement are plotted in Fig. 5.4. The reference intensity was measured without the NP-GaN/GaN DBR sample (black curve in Fig. 5.4 (a)). The measured reflectance spectrum is displayed in Fig. 5.4 (b) in red color, showing the 100 nm-wide stop band centered at $\sim$ 620 nm. A peak reflectance was turned out to be more than 99.5% at 610 nm from the inset of Fig. 5.4 (b). The estimated refractive index of the NP-GaN layer was calculated by the volume average theory, where effective refractive index $n_{eff}$ can be expressed as $[(1 - \psi){n_{GaN}}^2 + \psi{n_{air}}^2]^{1/2}$ [**?** ]. Based on this refractive index of the porosified layers, simulated results on the reflectance spectrum can be found from Fig. 5.4 (c) showing the similarity to the reflectance measured from experiments. The discrepancy between the simulated and measured results may come from the non-uniform refractive indices of each NP-GaN layers in the DBR structures.

## 5.3 Low threshold lasing performance from CQD-VCSEL devices

### 5.3.1 CQD-VCSEL design

The optically pumped CQD-based VCSEL devices already have been demonstrated under femto-second pulsed excitation regime, by our group in 2012 [11]. However, the DBR structures ($SiO_2/TiO_2$) used in the previous experiment had the relatively low reflectivity ($\sim$ 95%) compared to the one developed by our collaborators, Jung

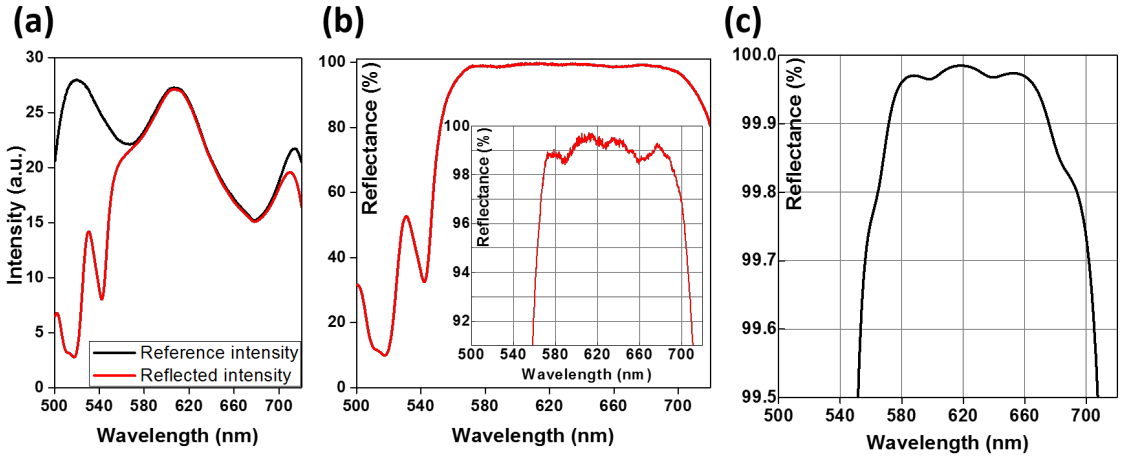


**Figure 5.4:** Results of the reflectance spectra from the NP-GaN/GaN DBRs. (a) Black and red curves represent reference and reflected intensities, respectively. (b) Calculated reflectance spectrum. Inset is the zoomed-in view of the spectrum. (c) (COMSOL-) Simulated reflectance spectrum assuming the refractive indices of 1.53 and 2.39 for the NP-GaN and GaN layers, respectively.

Han *et. al.*, of which the reflectivity was 99.5% at maximum. Also, since the highly concentrated CQD solutions ($\sim$ 100 mg/ml) have been inserted between the two $SiO_2/TiO_2$ DBRs to form a wedge structure with a 30 $\mu$m separation, it was inevitable to have multiple lasing peaks in the output spectra due to the long cavity length.

However, the electro-chemically porosified NP-GaN layers can provide tunable refractive index covering wide ranges (range from 560 to 650 nm). The precise control of the tunable refractive index enables highly reflective NP-GaN/GaN DBRs. It should be noted that the NP-GaN layers still preserve the electrical conductivity of their native GaN form. Thus, NP-GaN/GaN DBR is a possible candidate for the next generation of electrical injection types of optoelectronic devices, such as lasers. In this study, we built optically pumped CQD lasers using the NP-GaN/GaN DBRs as highly reflective cavity mirrors.

To fabricate CQD-based VCSELs, the solution of CQDs (in ultrahigh concentration, $\sim$ 150 mg/ml) was spin-coated on the NP-GaN/GaN DBR. However, due to the porous nature of NP-GaN layers, spin-coating liquid solutions such as CQD solutions, photoresist, or Poly Methyl-Methacrylate (PMMA) on the NP-GaN layer can change the reflectance spectrum of the DBR; the liquid can be absorbed into the patterned trenches on the surface by the capillary force (see Fig. 5.2). For example, the viscous photoresist solution fills the nanopores to change the effective refractive index of the NP-GaN layers to shift the optimized reflectance spectrum and reduce the maximum reflectivity. In the case of the CQD solutions, nanocrystals can stick onto the porous walls, making them hard to be removed. Therefore, a blocking layer between the CQD film and the NP-GaN layer was required to prevent the CQDs from flowing into the trenches during the spin-coating process. We chose PMMA as the blocking layer which is transparent and easily removable by acetone.

Since introducing a thin layer of PMMA ($\sim$ 200 nm) may affect the reflectance

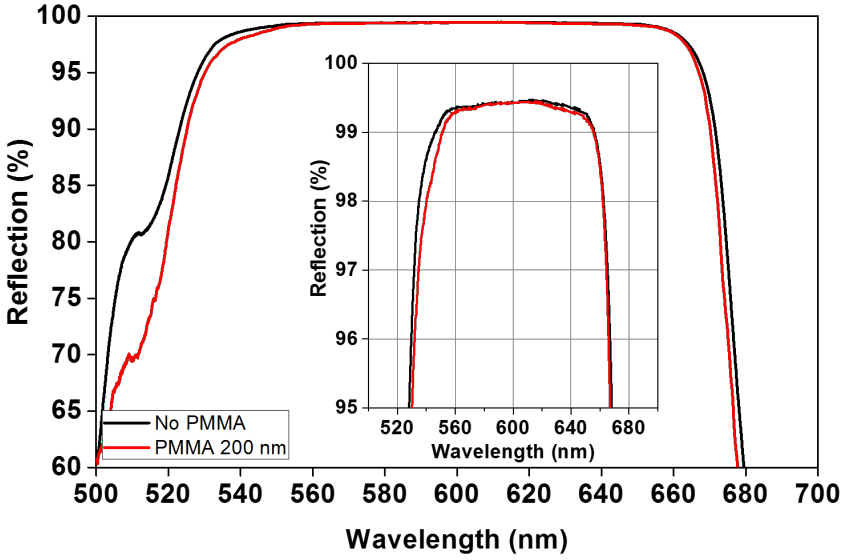


**Figure 5.5:** Reflection spectra for the NP-GaN/GaN DBR without(black) and with (red) the 200 nm-thick PMMA layer. The inset is the close-up plot.

spectrum of the DBR, we measured the reflectance spectrum of the DBR with an additional PMMA (950PMMA-A4, *MicroChem Corp.*) layer of 200 nm thickness (spin-coated at 4000 rpm and cured at 180°C for 90 seconds). Figure 5.5 shows the two reflection spectra of NP-GaN/GaN DBR with and without the PMMA layer. Although the drop in the reflectance in 500 - 560 nm and the narrowing of the stop band were observed, the overall reflectance of the DBR with the additional PMMA layer mostly remained the one without the PMMA layer, making it suitable for the optically pumped CQD-VCSEL application.

The CQD film was deposited by the same spin-coating process at 1000 $\sim$ 2000 rpm, resulting in 200 to 300 nm-thick CQD solid film. The other NP-GaN/GaN DBR was overlaid on top of the CQD-coated DBR sample. Figure 5.6 illustrates the CQD-VCSEL design configuration seen from the side and top, respectively. As the top view in Fig. 5.6 suggests, overlaying the two DBRs in perpendicular direction produces square-lattice arrays (100 $\times$ 100 $\mu$m size for each pixels), due to the geometry of the vertical opening trenches on each layer.

### 5.3.2 Results

The optical excitation source for the CQD-VCSELs was the laser described in Chapter 4 (PNP-M0810, *teem photonics*; wavelength of 1064 nm, pulse duration of 400 ps, and repetition rate of 1 kHz). Since the CQD-VCSEL was designed to emit red color, the output (532 nm) from the second harmonic generation setup (see Fig. 4.7) was used as an excitation wavelength. Instead of a cylindrical lens, a spherical lens was used to create a circular spot on the CQD-VCSEL with less than 100 $\mu$m in diameter. A notch filter was placed behind the CQD-VCSEL to block the pumping laser. Emitted photons from the CQD-VCSEL were collected by a lens and sent to a spectrometer.

Figure 5.7 represents the emission characteristics from the CQD-VCSEL. Fig-

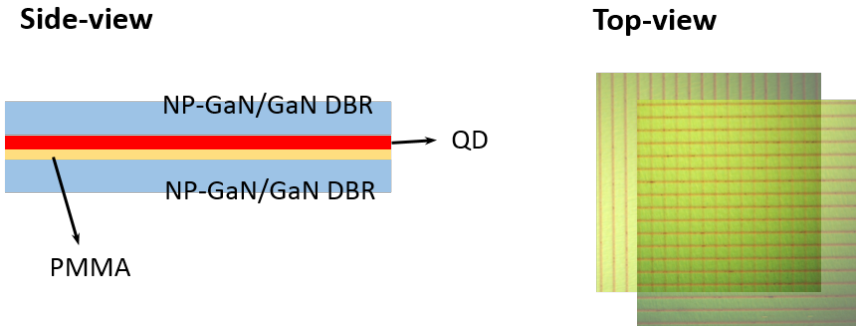


**Figure 5.6:** Schematic illustration of the CQD-VCSEL device configuration for side-view and top-view. The PMMA layer and the CQD films were spin-coated on the NP-GaN/GaN DBR, then another DBR was overlaid vertically to form natural square-lattice arrays of pixelated CQD-VCSEL.

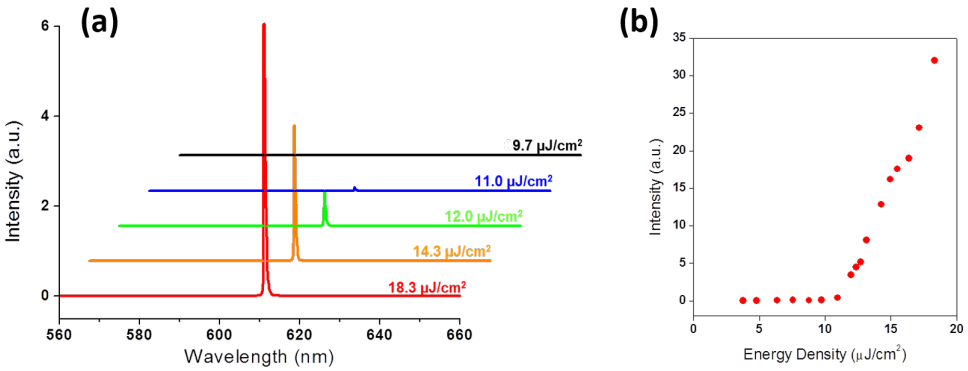


**Figure 5.7:** (a) Emission spectra at various pumping energy densities. Single-mode monochromatic lasing peak at 611 nm emerged when the pumping energy density was more than 11.0 $\mu$J/cm$^2$. (b) Integrated intensities were plotted as a function of pumping energy density, showing a clear threshold behavior.

ure 5.7 (a) shows the emission spectra along the different pumping energy densities. Spectral line-narrowing and threshold behavior were observed from the results. Below the threshold (9.7 $\mu$J/cm$^2$), no lasing signal or spontaneous emission was detected due to the highly reflective NP-GaN/GaN DBRs which blocked the photoluminescence from the CQD film. However, as the excitation intensity increased, a monochromatic (FWHM $<$ 1 nm) single-mode lasing outputs at 611 nm emerged. Figure 5.7 (b) shows a clear evidence of the threshold behavior. From Figure 5.7 (b), the lasing threshold was approximately 11.0 $\mu$J/cm$^2$. Note that this is almost one order of magnitude lower than the threshold of the red CQD DFB laser (120 $\mu$J/cm$^2$), considering the same CQD materials as the gain media were used. We also measured the output power of the lasing ouput beam from the CQD-VCSEL. The output was 1.5 $\mu$W when the input power was about 40 $\mu$W. Considering the absorption by the CQD film and two sides of lasing outputs from the CQD-VCSEL device, the conversion efficiency was about 11.4%. This was the first time showing the ultra-low lasing threshold and high conversion efficiency for operating CQD-VCSELs with the high-Q and low-loss cavity from the NP-GaN/GaN DBR structure.

Not only the temporal coherence, the spatial coherence of the lasing output from the CQD-VCSEL was validated by taking images of the surface of the CQD-VCSEL device as seen in Fig. 5.8. When the pumping energy density was lower than the lasing threshold, the photons were only emitted by the spontaneous emission which was filtered (blocked) by the DBR. Thus almost nothing can be seen from the microphotograph (leftmost one in Fig. 5.8 (a)). As increasing the pumping energy density further to exceed the lasing threshold, the photons were emitted via stimulation emission process from the CQD film forming an intense bright lasing beam. Figure 5.8 (b) shows the far-field pattern of the CQD-VCSEL device with spatially well-defined lasing output beam.

As the lasing threshold for the CQD-VCSEL turned out to be very low compared

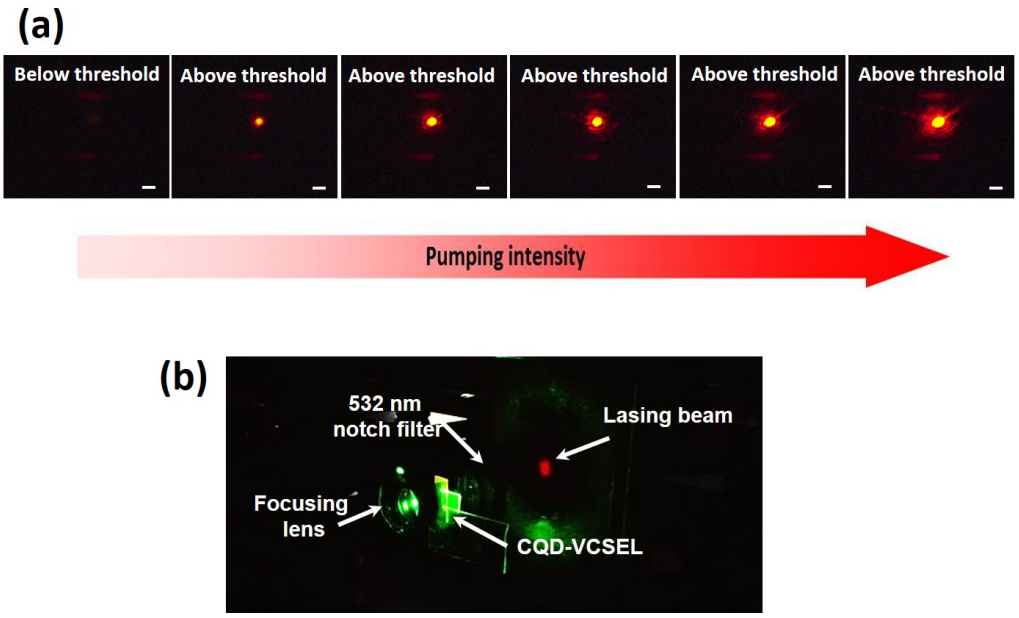


**Figure 5.8:** (a) Microphotographs of the surface of the CQD-VCSEL device. Below the threshold, no lasing signals were detected. However, above the lasing threshold, intense lasing outputs from the device can be seen and the intensities increases as the pumping energy density increases. Scale bars are 30 $\mu$m. (b) Far-field pattern from the CQD-VCSEL device. A 532 nm-notch filter was used to block the pumping laser beam. Well-defined spatially coherent red lasing beam were observed on a white screen.

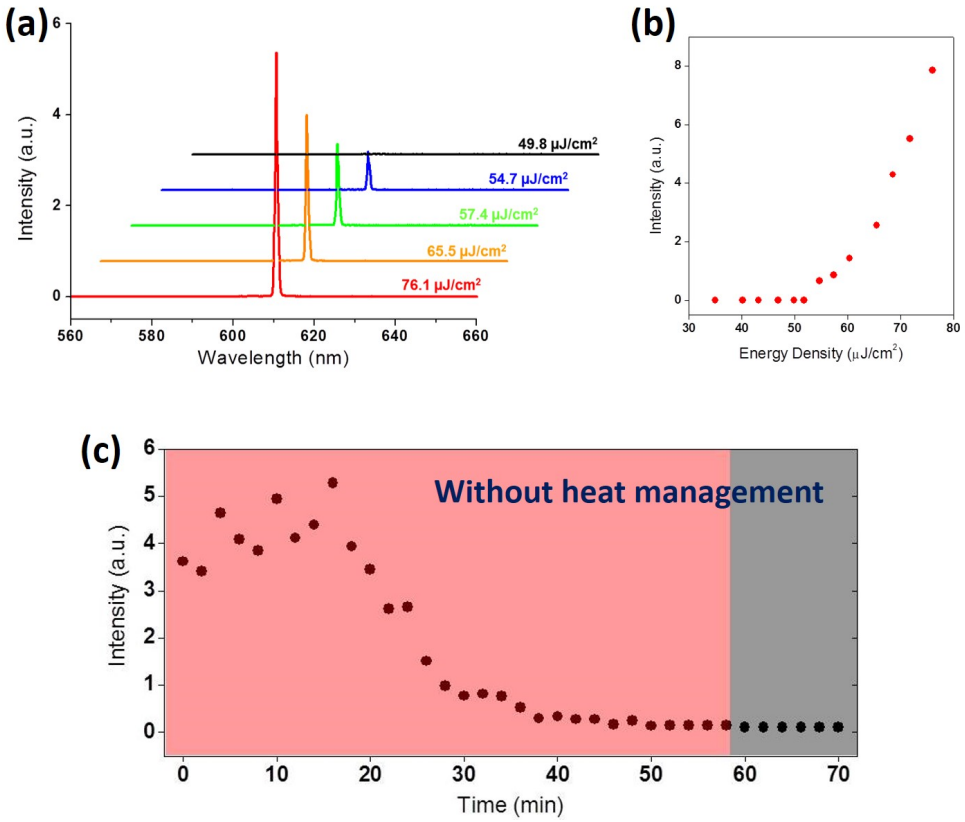


**Figure 5.9:** (a) Emission spectra at various pumping energy densities. Single-mode monochromatic lasing peak at 611 nm emerges when the pumping energy density is more than 54 $\mu$J/cm$^2$. (b) Integrated intensities have been plotted as a function of pumping energy density, showing a clear threshold behavior. (c) CQD-VCSEL device lifetime without heat management. The device lasts for about 58 minutes under continuous excitation at 20 Hz of repetition rate and 5 times of the lasing threshold pumping intensity conditions. After 58 minutes of optical excitation, the CQD-VCSEL device stopped producing lasing outputs.

to that of the CQD DFB lasers, we decided to use a longer pulsed laser (NY60B-20, *Continuum*) for pumping the CQD-VCSELs; wavelength of 532 nm, pulse duration of 10 ns and repetition rate of 20 Hz. The spectral characteristics are plotted in Fig. 5.9, which are very similar to the result of the 270 ps-pulsed laser excitation (*cf.* Fig. 5.7) but with a different lasing threshold. In this longer pulsed excitation experiment, the lasing threshold was about 54 $\mu$J/cm$^2$ which was about 5 times higher than that of 270 ps-pulsed laser excitation case. However, this was still lower than the lasing threshold using DFB laser (120 $\mu$J/cm$^2$).

We also measured the lifetime of a CQD-VCSEL device using the same laser excitation method without any heat management. While maintaining the input pumping energy density at 5 times higher ($\sim$ 250 $\mu$J/cm$^2$) than the lasing threshold, we measured the output spectrum from the CQD-VCSEL with a spectrometer every two minutes. The peak of the output signals as a function of time was plotted in Fig. 5.9 (c). The lasing outputs from the CQD-VCSEL device were detected for about an hour, until no lasing was observed. The continuous optical excitation into the CQD-VCSEL device induced accumulation of heat which did not dissipate to the substrate fast enough due to the low thermal conductivity of the close-packed CQD film. The thermal conductivity of the CQD film has not been measured, but considering the CQD films closely packed nanocrystal structure, we can estimate it to be significantly lower than that of a bulk CdSe semiconductor which is around 9 W/m·K [**?** ]. The increased local temperature of the CQD film by the intense optical excitation results in peeling-off of the surface organic ligands. This may induce significant amount of surface trap states that can trap the hot excitons and quench the emission process. Also, quantum dot charging process induced by the laser beam can also lead to the non-radiative Auger process, consequently quench the emission process.

## 5.4 Pixelated CQD-VCSEL arrays

### 5.4.1 Results

We developed the ultra-low lasing threshold CQD-VCSEL device with high degree of spatial coherence. Also, the square-lattice pattern of the device was formed by overlaying two NP-GaN/GaN DBRs. We used this configuration to build the CQD-VCSEL pixelated arrays as a proof-of-concept for the two dimensional scanning display application. As already described, a single NP-GaN/GaN DBR has a pattern of vertical lines as opening windows for electro-chemical etching (100 $\mu$m of periodicity and 10 $\mu$m of width). Overlaying two DBRs in vertical direction naturally formed a number of individual pixels of CQD-VCSELs in square-lattice arrays. Figure 5.10 (a) shows the microphotograph image of the pixelated arrays of CQD-VCSEL devices under white light illumination. Dark regions in Fig. 5.10 (a) (100 $\mu$m $\times$ 100 $\mu$m for an individual pixel) represent the pure DBR areas.

We measured the lasing spectra and the thresholds of the 10 by 10 pixelated CQD-VCSEL arrays. Figure 5.10 (b) is a graphical map representing the lasing thresholds from 100 pixelated CQD-VCSELs in different colors. Pixels with colors close to red have high thresholds (from 24.4 to 30.6 $\mu$J/cm$^2$). The average threshold of overall pixels was 26.2 $\pm$ 1.0 $\mu$J/cm$^2$. The histogram of the lasing peaks was plotted in Fig. 5.10 (c). The most frequent peaks appeared near 615 nm, the wavelength we aimed to get the maximum gain coefficient from the red CQDs by optimizing the thicknesses of the PMMA and CQD layers including air gaps between the two NP-GaN/GaN DBRs. Distribution of the peak lasing wavelengths may come from the non-uniformity of the PMMA and CQD films, or difference of the local reflectivity at certain spots on the NP-GaN/GaN DBRs. Nevertheless, the distribution of the lasing thresholds were close enough meaning that it was able to produce uniform lasing output beams from individual pixels of CQD-VCSELs except some pixels

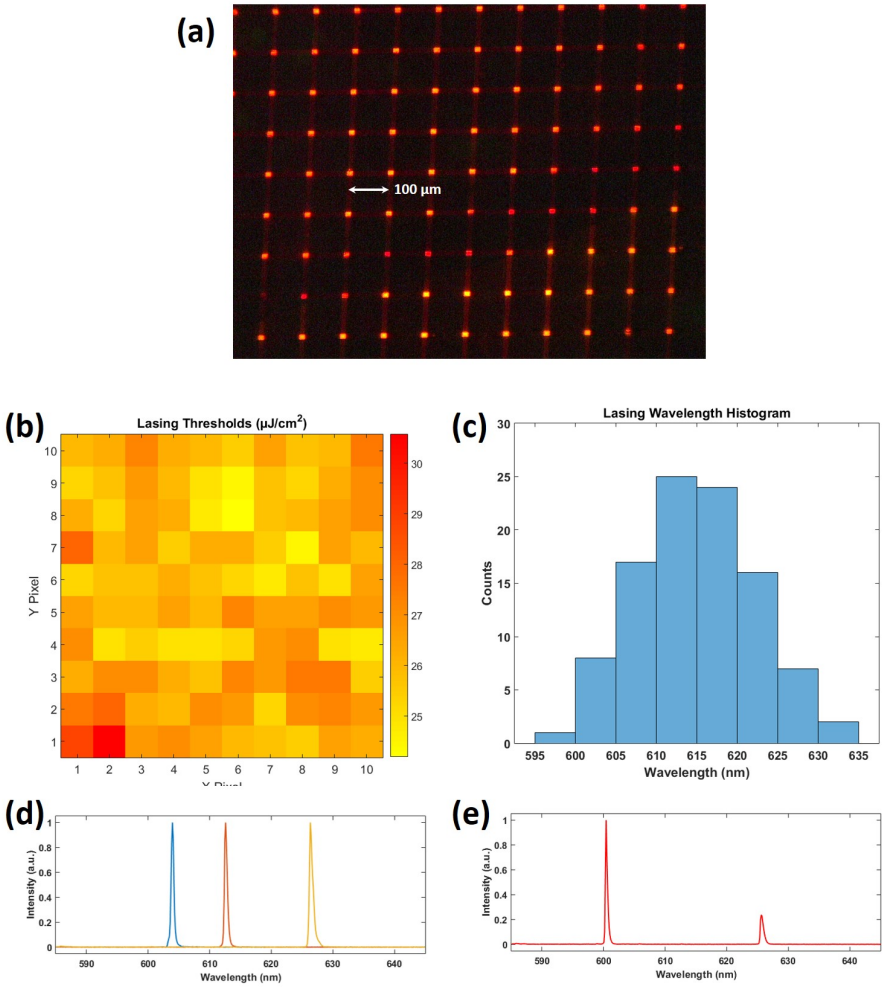


**Figure 5.10:** (a) Microphotograph image of pixelated arrays of CQD-VCSEL devices under white light illumination formed by sandwiching two NP-GaN/GaN DBRs in vertical direction. (b) Map of lasing thresholds for the 10 × 10 arrays of pixelated CQD-VCSELs. (c) Histogram of the lasing peaks. (d) Three examples of lasing spectra from the individual CQD-VCSELs showing very narrow (monochromatic) lasing peaks. (e) Some CQD-VCSELs exhibited two lasing peaks from a single individual pixel.

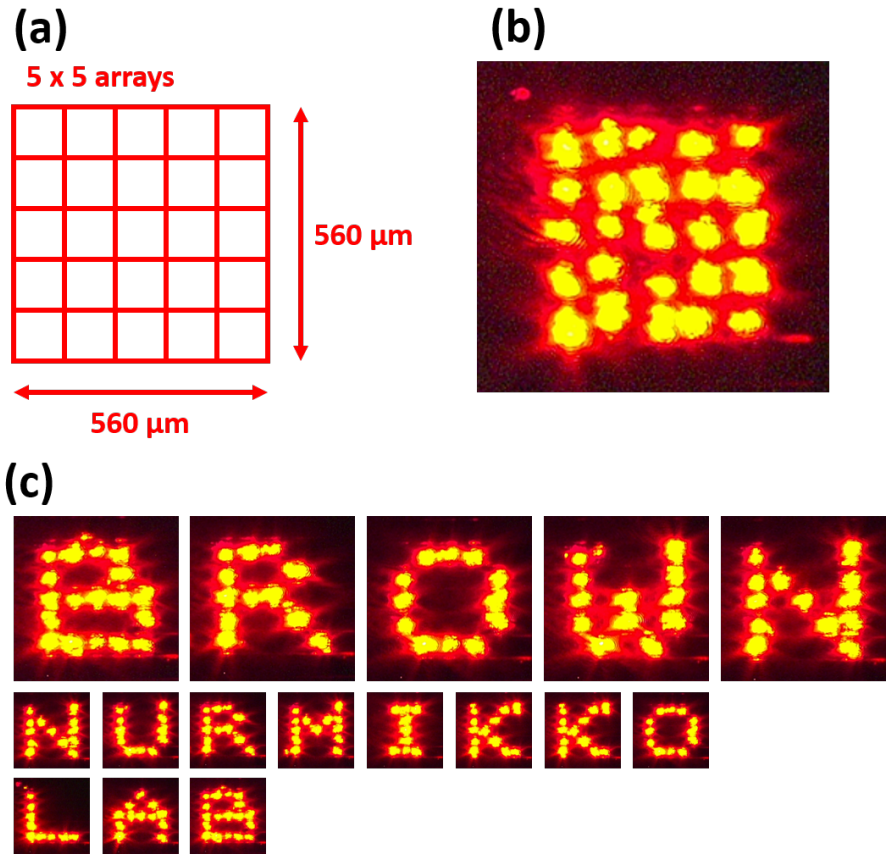


**Figure 5.11:** (a) Schematic description for 25 pixels of CQD-VCSEL laser arrays. (b) Lasing outputs from individual CQD-VCSEL pixels. (c) Example alphabetic characters formed by 5 × 5 pixelated CQD-VCSEL arrays. Scanned images were taken under 500 ms of integration time.

exhibiting two lasing peaks (Fig. 5.10 (e)). However, most of the CQD-VCSEL pixels (more than 90%) showed a single lasing peak as seen in Fig. 5.10 (d).

Finally, we built 25 (5 × 5) pixels of CQD-VCSEL for a proof-of-concept two - dimensional laser arrays. The dimensions of each pixels were 100 $\mu$m × 100 $\mu$m, and pixels were separated by $\mu$m. The total size was 560 $\mu$m × 560 $\mu$m as seen in Fig. 5.11 (a). A scanning micro-mirror was used to scan the laser excitation beam (second harmonic generation from PNP-M0810, *teem photonics*; 532 nm-wavelength, 270 ps-pulse duration, 1000 Hz-repetition rate) to the pixelated CQD-VCSEL arrays. Then the reflected pumping laser beam from the micro-mirror was focused by a telecentric objective lens and a spherical lens on to the surface of the CQD-VCSEL. The size of the focused pumping laser beam was about 90 $\mu$m in diameter so that it can fit in a single CQD-VCSEL pixel. The micro-scanning mirror was controlled by a commercial software (LabView, *National Instruments*) with fast and precise angle controls. In this demonstration, dwelling time for each CQD-VCSEL pixels was set to 4 ms. In turn, the time required to scan the whole CQD-VCSEL arrays was about 100 ms in principle. However, in order to capture the lasing output beams from all pixelated CQD-VCSELs, the integration time for taking an image must be longer than 500 ms at least due to the delay caused by the communication between the software and the micro-mirror system. Figure 5.11 (b) shows the lasing output from 25 pixels of CQD-VCSELs. Based on the array, we demonstrated alphabetic characters as examples in Fig. 5.11 (c).

### 5.4.2 Limitations

Although we successfully demonstrated two dimensional 25 pixelated CQD-VCSEL arrays by a scanning mirror system in the previous section, some limitation still exists in the current setup. First, the laser beams from each CQD-VCSEL pixels were not uniform in their sizes and intensities. In Fig. 5.11 (b), some lasing spots

were small compared to others and dislocated from the original pixel positions. This issue mainly comes from the non-uniform optical characteristics of the NP-GaN/GaN or the CQD film. In this study, we relied on the "DBR overlay" method to crated the configuration. However, placing a DBR on top of another DBR must involve non-controllable air gap. Consequently, it is almost impossible to control the peak lasing wavelength of the CQD-VCSEL devices. In order to avoid this problem, introducing a micro-meter scale spacer between the two DBR can be a possible solution, such as periodic platinum pillars ($\sim$ 3 $\mu$m) by focused-ion beam deposition and pressured overlaying of DBRs.

The pumping laser used in this study also limits the application of CQD-VCSEL as a practical display device. To deliver higher resolution display, the number of CQD-VCSEL pixels should be increased. However, this requires the pumping laser to have a higher repetition rate as well. In our current setup, the repetition rate of the pumping laser was only 1 kHz, which will take more than 1 second if it scans the whole 1000 CQD-VCSEL pixels. Since the repetition rate of the pumping laser sets the frame rate to be significantly slow for larger size arrays, it needs to be high enough for practical application. In addition, the scanning speed of the micro-mirror system needs to be faster to scan wide areas of the pixelated CQD-VCSEL arrays. This issue can be simply solved by replacing the current scanning mirror system to such as a fast resonant micro-mirror or acousto-optic deflector systems which provides much faster scanning speed. A digital micro-mirror device (DMD) system can be another candidate for illuminating the pumping laser beam into the pixelated CQD-VCSEL arrays.

## 5.5 Conclusions

In this chapter, we showed the fabrication process of GaN-based DBRs. By using the electro-chemical etching, oxalic acid electrolyte selectively porosified the heavily doped n-type GaN layers. 10 pairs of alternating NP-GaN and GaN layers have been fabricated on sapphire substrate with very high reflectivity (more than 99.5% at 610 nm) and wide stop band (100 nm). These DBRs were incorporated with the CQD gain media to develop optically pumped CQD-VCSEL devices. A 200 nm-thick PMMA layer was spin-coated on top of the NP-GaN/GaN DBR, and 200 nm-thick CQD film was deposited via spin-coating as well. Then, another NP-GaN/GaN DBR was overlaid to create CQD-VCSEL devices.

Second harmonic generations (532nm) from two Nd:Yag lasers (270 ps and 10 ns of pulse duration) were chosen as the optical excitation sources. Under 270 ps-pulsed laser excitation, the CQD-VCSEL exhibited very well-defined red lasing output beams with the threshold of 11.0 $\mu$J/cm$^2$. For 10 ns-pulsed laser excitation, the lasing threshold was about 54.7 $\mu$J/cm$^2$ which is still lower than that of the DFB lasers under 270 ps-pulsed excitation. The ultra-low lasing threshold and high degree of spatial coherence from the CQD-VCSEL devices can be attributed to the high quality of the NP-GaN/GaN DBRs (high-Q and low-loss). Importantly, the fact that the electro-chemically etched NP-GaN still preserves the electrical conductivity opens the possibility to realize the fabrication of electrically-driven laser devices, or monolithic design of all nitride-based laser devices.

The square-lattice patterns were formed in the CQD-VCSEL by overlaying the two NP-GaN/GaN DBRs. Based on this, we built the scanning micro-mirror system to create the 25 pixelated CQD-VCSEL arrays as a demonstration. Although the current scanning micro-mirror system and the repetition rate of the pumping laser are limiting factors on delivering commercial level of display products, advances in subsequent technologies including faster scanning systems (e.g. acousto-optic

deflectors) and proper heat managements on the CQD films may enable the CQD-VCSEL to play an important role as a future display device.

# Bibliography

[1] V.S. Dneprovskii, V.I. Klimov, D.K. Okorokov, and Y.V. Vandyshev. Strong optical nonlinearities and laser emission of semiconductor microcrystals. *Solid State Communications*, 81(3):227–230, 1992.

[2] J. Butty, Y.Z. Hu, N. Peyghambarian, Y.H. Kao, and J.D. Mackenzie. Quasicontinuous gain in sol-gel derived CdS quantum dots. *Applied Physics Letters*, 67(18):2672–2674, 1995.

[3] Y.Z. Hu, H. Gie, N. Peyghambarian, and S.W. Koch. Microscopic theory of optical gain in small semiconductor quantum dots. *Physical Review B*, 53(8):4814, 1996.

[4] H. Giessen, J. Butty, U. Woggon, B. Fluegel, G. Mohs, Y.Z. Hu, S.W. Koch, and N. Peyghambarian. Ultrafast nonlinear gain dynamics in semiconductor nanocrystals. *Phase Transitions*, 68(1):59–94, 1999.

[5] V.I. Klimov, A.A. Mikhailovsky, S. Xu, A. Malko, J.A. Hollingsworth, C.A. Leatherdale, H.J. Eisler, and M.G. Bawendi. Optical gain and stimulated emission in nanocrystal quantum dots. *Science*, 290(5490):314–317, 2000.

[6] C. Dang, J. Lee, K. Roh, H. Kim, S. Ahn, H. Jeon, C. Breen, J.S. Steckel, S. Coe-Sullivan, and A.V. Nurmikko. Highly efficient, spatially coherent distributed feedback lasers from dense colloidal quantum dot films. *Applied Physics Letters*, 103(17):171104, 2013.

[7] K. Roh, C. Dang, J. Lee, S. Chen, J.S. Steckel, S. Coe-Sullivan, and A.V. Nurmikko. Surface-emitting red, green, and blue colloidal quantum dot distributed feedback lasers. *Optics Express*, 22(15):18800–18806, 2014.

[8] Y. Zhang, S.W. Ryu, C. Yerino, B. Leung, Q. Sun, Q. Song, H. Cao, and J. Han. A conductivity-based selective etching for next generation gan devices. *Physica Status Solidi (b)*, 247(7):1713–1716, 2010.

[9] D. Chen, H. Xiao, and J. Han. Nanopores in gan by electrochemical anodization in hydrofluoric acid: Formation and mechanism. *Journal of Applied Physics*, 112(6):064303, 2012.

[10] C. Zhang, S.H. Park, D. Chen, D.W. Lin, W. Xiong, H.C. Kuo, C.F. Lin, H. Cao, and J. Han. Mesoporous gan for photonic engineering highly reflective gan mirrors as an example. *ACS Photonics*, 2(7):980–986, 2015.

[11] M.M. Braun and L. Pilon. Effective optical properties of non-absorbing nanoporous thin films. *Thin Solid Films*, 496(2):505–514, 2006.

[12] C. Dang, J. Lee, C. Breen, J.S. Steckel, S. Coe-Sullivan, and A.V. Nurmikko. Red, green and blue lasing enabled by single-exciton gain in colloidal quantum dot films. *Nature Nanotechnology*, 7(5):335–339, 2012.

[13] O. Madelung. *Semiconductors: data handbook*. Springer Science & Business Media, 2012.

# Chapter 6

# Conclusions and Outlook

In the preceding chapters we presented both theoretical predictions on the quantum confinement effect in semiconductor nanocrystal quantum dots and a number of techniques for fabricating CQD-based lasers. Most notably, we show that CQDs are size-tunable solution-processed semiconductor nanocrystals with low size distribution and high crystalline structures. As a result, CQDs can exhibit bright, pure, and tunable output emission colors which correspond to high quantum yield, narrow inhomogeneous broadening, and quantum size effect respectively. It makes CQDs a competitive material for solid-state lighting and full-color display applications. In this thesis, the light amplification properties and optically pumped laser applications of CQDs have been presented in the physics and engineering points of view.

To achieve stimulated emission from dense CQD films at room temperature, ultrafast (sub-picosecond time scale) optical excitation sources should be equipped to compete with the fast non-radiative multiexcitonic Auger recombination process. This has delayed the practical realization of CQD-based laser devices. Thus, reaching optical gain from single exciton state becomes a crucial requirement. Our collaborator, *QD Vision, Inc.* has fabricated engineered type-I core/shell CQDs with high quality of crystalline structures in ultrahigh concentration, which were verified by

TEM and XRD measurements. High concentration of CQD solution enabled densely packed expitaxial-like solid films by the simple spin-coating method. The CQD films was able to show robust excitonic absorption peaks and high photoluminescence quantum yield at room temperature.

With these high quality of CQD materials, we investigated optical gain properties by performing ultrafast laser pump-probe spectroscopy. Two contrasting types of CQDs were studied in these experiments: pyramidal-shaped CdSe/ZnCdS CQD with large magnitude of Stokes shift and spherical-shaped CdSe/ZnS/ZnCdS CQD with narrow inhomogeneous broadening (low monodispersity). Optical gain was observed for both CQDs at $<N> = 0.5$ and 0.7, respectively. Therefore, it demonstrated the dominance of single exciton states for development of optical gain. Also, the optical gain persisted for more than 1 ns which is two orders of magnitude longer than the Auger recombination process. We believe that a careful spectral balance between the lowest exciton absorption resonance and its corresponding spontaneous emission peak (precisely optimized Stokes shift) plays a key role for the access to the single exciton optical gain regime together with ability to load ultrahigh volume fraction (densely packed film form) and low nanoparticle monodispersity.

Having the advantage of the single exciton optical gain property, we fabricated red, green and blue colors of CQD lasers at room temperature. Nano-grating structures were incorporated with dense CQD films to create $2^{nd}$-order surface-emitting DFB laser devices. Various techniques were used to fabricate the nano-grating structures such as holographic interference patterning, focused-ion beam milling process, and electron-beam lithography. A compact solid-state laser with 270 ps of pulse duration was used to generate lasing output beams from the surface of the CQD DFB devices with the lasing threshold levels from 120 to 330 $\mu J/cm^2$. Measured far-field patterns were good evidences for the high degree of spatial coherence. Also, we were able to achieve fairly high conversion efficiency (up to 10%) for the lasing output

beams.

Another type of resonator structure for stimulated emission was employed to our CQD material: VCSEL. Our collaborator, Prof. Jung Han group at Yale University has developed a novel technique that can selectively porosify and etch heavily doped n-type GaN layers to give NP-GaN with wide tuning range of refractive index while still maintaining electric conductivity. This enabled the fabrication of GaN-based DBRs consisting 10 alternating pairs of NP-GaN/GaN layers. They showed very wide stop band and high reflectivity (more than 99.5%) at around 610 nm.

By sandwiching PMMA and CQD films with optimized thicknesses between the two NP-GaN/GaN DBRs, pixelated CQD-VCSEL arrays were fabricated. Using the same optical excitation source, robust lasing outputs were measured at ultralow threshold level, 11 $\mu J/cm^2$ with high temporal and spatial coherence as well, attributed by the high Q and low loss of the DBR resonator structure. Adopting a scanning micro mirror system, we built proof-of-concept 25 (5 by 5) pixelated arrays of CQD-VCSEL.

Heat management is a crucial point for semiconductor laser devices. Unfortunately, our CQD-based DFB lasers and VCSELs did not involve any thermal treatment. Although the building blocks (for example, CdSe, ZnS, etc.) for the CQD nanocrystals themselves are thermally good conductive, the thermal conductivity of close-packed CQD films might be fairly low. Therefore, an efficient way for dissipating heat created inside of CQD films due to high excitation condition should be involved. Mixing CQDs with high thermal conductive materials such as graphene or carbon nanotubes can be a possible option. Proper heat management and protection from ambient air condition which is directly related to robustness of devices may make the CQDs more efficient materials for solid-state lighting, light-emitting diode, and laser display industry.